

Water at α -Alumina Surfaces: Energetics, Dynamics and Kinetics

Dissertation zur Erlangung des akademischen Grades
›doctor rerum naturalium‹ (Dr. rer. nat.)
in der Wissenschaftsdisziplin Theoretische Chemie

vorgelegt von

Sophia L. Heiden

an der

Mathematisch-Naturwissenschaftlichen Fakultät
der Universität Potsdam



Potsdam, 2018

This work has been done between January 2015 and December 2018 in the group of Prof. Dr. Peter Saalfrank at the Institute of Chemistry at the University of Potsdam.

Potsdam, December 2018

Erstgutachter: Prof. Dr. Peter Saalfrank (Uni Potsdam)

Zweitgutachter: Prof. Dr. Beate Paulus (FU Berlin)

Drittgutachter: PD Dr. Ralf Tonner (Uni Marburg)

Published online at the

Institutional Repository of the University of Potsdam:

<https://doi.org/10.25932/publishup-42636>

<https://nbn-resolving.org/urn:nbn:de:kobv:517-opus4-426366>

Contents

Preamble	5
1 Methodology	9
1.1 The Electronic Schrödinger Equation	9
1.2 Wave Function Theory	10
1.2.1 Hartree-Fock Theory	10
1.2.2 Møller Plesset Perturbation Theory	12
1.3 Density Functional Theory	14
1.3.1 Basics	14
1.3.2 Kohn-Sham Equations and Choice of Exchange-Correlation Functionals	15
1.3.3 Hybrid Functionals	17
1.3.4 Dispersion Corrections	17
1.4 Periodic Boundary Conditions	18
1.5 Plane Wave Bases, Atom Centered Bases and Peculiarities	21
1.6 <i>Ab Initio</i> Molecular Dynamics	22
1.7 Vibrational Spectroscopy: Frequencies and Intensities	24
1.8 Transition States and Kinetics	27
1.9 Software and Computational Details	29
2 Water on α-Al₂O₃(0001)	31
2.1 Supercell Model for the Adsorption of Water	32
2.2 Adsorption Energies, Vibrations and Reactions of Water on α -Al ₂ O ₃ (0001) . .	35
2.2.1 Adsorption Energies	35
2.2.2 Frequency Analysis: Normal Modes and Beyond	40
2.2.3 Activation Energies and Reaction Rates	42
2.3 AIMD Simulation of Molecular Beam Scattering Experiments	43
2.3.1 Beam Model	43
2.3.2 Example Trajectories	47
2.3.3 Microcanonical AIMD at a Clean Surface at $T = 0$	47

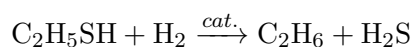
Contents

2.3.4	Thermalized Surface	52
2.3.5	Refined Surface Model	53
2.3.6	Refined Beam Model	57
3	Water on α-Al₂O₃(11$\bar{2}$0)	61
3.1	Surface Models	61
3.2	Water Adsorption: Adsorption Energies and Geometries	65
3.2.1	Low Coverage	65
3.2.2	Higher Coverages	69
3.2.3	Other Surface Terminations	71
3.3	Dissociation and Diffusion Reactions of Water Species	71
3.4	Interpretation of Vibrational Spectra	77
3.4.1	Vibrational Analysis Based on Normal Modes	78
3.4.2	Harmonic Vibrational Spectra from Born Effective Charges	87
3.4.3	Vibrational Analysis Based on Vibrational Density of States Curves . .	89
	Summary	93
	Appendix	97
A	Special Basis Sets for AO Calculations with CRYSTAL	97
B	Basis Set Superposition Error: Adsorption of H ₂ O at α -Al ₂ O ₃ (0001)	102
C	Reaction Probabilities for AIMD MBS Simulations of H ₂ O at α -Al ₂ O ₃ (0001) .	104
C.1	Microcanonical AIMD at a Clean Surface at $T = 0$	104
C.2	Refined Surface Models: Effects of Precoverage	105
C.3	Refined Beam Models: Clustering and Preexcitation	106
D	Test of a Symmetric Slab: Normal Modes of H ₂ O at α -Al ₂ O ₃ (11 $\bar{2}$ 0)	108
E	Harmonic Vibrational Spectra for Higher Coverages and the O-II Terminated α -Al ₂ O ₃ (11 $\bar{2}$ 0) Surface	109
	References	117

Preamble

The importance of surface science in our industrialized world is overwhelming. Most processes in chemical industry are carried out with the help of (heterogeneous) catalysts [1–3] which speed up reactions by lowering the reaction barrier. The advantage of heterogeneous over homogeneous catalysts is that these do not need to be separated from the reactants and the product after the process, which is often a costly step in the production of chemicals. It is therefore desirable to understand heterogeneous catalytic processes by learning more about the microscopic phenomena, which take place on the surface of materials especially by computational methods because they can deliver basic understanding on the atomic level. Metal oxide materials are commonly used as catalysts as well as catalyst support materials. Hence, understanding their properties in contact with chemicals is crucial. In this work, we consider water, which can act as a reactant, solvent or also impurity in aforementioned processes due to its ubiquity.

In technical applications alumina (Al_2O_3) is commonly used as an abrasive due to its hardness, as a whitening pigment and also ceramics are widely applied because of the insulating properties. Alumina is also applied as a catalyst (for example in the Claus process [4]) and more often as a co-catalyst, for example in the ethylene epoxidation [5] or in the hydrodesulfurization [6] where it acts as a support material for the active cobalt and molybdenum catalyst in a sulfur removing process:



Furthermore, in geochemical sciences Al_2O_3 is a subject of a variety of studies since aluminum is the most abundant metal in the crust of the earth with 8.1% and the third most abundant element therein [7, 8]. Alumina can additionally be seen as a model system for more complex aluminosilicates. Mineral oxides are omnipresent in the crust of the earth and henceforth are present in most geochemical processes. Since the times the earth's atmosphere was oxidizing in the early stages of the planetary evolution [9], which became even more extensive with the rise of photosynthetic life forms [10–12] around 2.2 billion years ago [13], oxidic rocks became more common.

Preamble

In all technically and environmentally relevant applications the Al_2O_3 system contains at least small amounts of water. Hence a quantitative understanding of the alumina water interaction on the microscopic scale is crucial. In the environment, alumina appears as rocks, *e.g.* corundum, or gems like ruby. Aluminum is also contained in some rocket fuels as a reduction agent, so as a result alumina particles are ejected into the atmosphere during the launch of a spacecraft [14]. The start of one space shuttle can produce around 276000 kg of alumina particles [15]. Measurements show that approximately one third of these particles can be deposited in the stratosphere [16] (in an altitude between 15 and 50 km above the surface of the earth). These particles are accumulated there and can react with water and other molecules [17, 18] and impact the ozone layer.

Different modifications of alumina exist, α , β and γ - Al_2O_3 , which are built slightly different and show distinct properties. This work focuses only on α -alumina. The structure of α -alumina has been well known for decades and was studied extensively (*e.g.* [19, 20]). It crystallizes in the hexagonal cell with $|a| = |b| \neq |c|$, with an angle of 60° between the cell vectors \underline{a} and \underline{b} . Also for this modification, different surface cuts can be observed. The most stable ones according to Kurita [21] are (0001), $(1\bar{1}02)$ and $(11\bar{2}0)$. In this work, the (0001) and the $(11\bar{2}0)$ surface cuts are subject of interest. Also for each surface cut, there exist several possible terminations, leading to different surface atom layers, with a specific stability. In case of the (0001) only the most stable Al-I terminated surface is investigated (nomenclature from Kurita *et al.* [21]). For the $(11\bar{2}0)$ surface the most stable O-I termination will be considered, but also the less stable O-II termination is of interest, the latter concerning a defect side.

This work divides into three different topics on those two different α -alumina surface cuts:

(i) Nowadays, a typical standard method to treat periodic surface systems is density functional theory (DFT) with the generalized gradient approximation (GGA). GGA functionals however are known to underestimate reaction barriers and hence overestimate reaction rate constants. Improving this issue is a great step towards the understanding of surface reactions like dissociation and diffusion. We want to achieve this by employing a hybrid functional as well as a wave function-based method (local Møller Plesset perturbation theory of second order, LMP2) for an exemplary hydrogen diffusion reaction, in this case at the (0001) surface. Furthermore we want to compare adsorption energies and vibrational frequencies obtained with a hybrid functional, and in the case of adsorption energies also LMP2, to calculations with GGA.

(ii) Molecular beam experiments have recently shown that water is able to adsorb both molecularly and dissociatively on an α - Al_2O_3 (0001) surface [22]. The results show an enhanced dissociation probability compared to “pinhole dosing”, which may be referred to adsorption

under thermal equilibrium conditions. However, precise mechanisms of the ongoing reactions and their relative probabilities are not known. In this work *ab initio* molecular dynamics calculations were conducted to unravel this process.

(iii) The $(11\bar{2}0)$ surface has not been studied to a great extent so far. Hence we first are interested in the structure of the clean surface, the adsorption of water in the low-coverage limit and also with higher coverages, calculated by DFT with a GGA functional. We search for stable molecular and dissociative minima and the reactions connecting these minima: dissociation and diffusion reactions to study the mobility and reactivity of adsorbed groups. In addition to that we want to calculate vibrational frequencies to compare with experimental research and help to understand and interpret their findings.

For this we first want to introduce the methodology that the calculations are based on, then proceed with the three subprojects just outlined and at the end give a summary.

Preamble

1 Methodology

In this chapter the basics of the theoretical methods applied in this work shall be explained. It starts from the ideas of wave function based theory, namely Hartree-Fock and Møller Plesset perturbation theory, and density functional theory, going over periodic boundary conditions, to the advantages and disadvantages when dealing with plane waves and atom centered bases, and continues with *ab initio* molecular dynamics. Then we will proceed with frequency calculations and intensities needed for the interpretation of vibrational spectra, then to transition state theory to compute reaction rates, and finally computational details of the applied software. Most basic theory parts of this chapter are based on References [23], [24] and [25].

1.1 The Electronic Schrödinger Equation

The theoretical description of chemical systems is often based on the calculation of their electronic structure. For this, the first step is to separate electronic and nuclear degrees of freedom as introduced by the Born-Oppenheimer approximation [26], which is appropriate due to the largely different masses of electrons and nuclei. Within this approximation, an electronic Schrödinger equation is solved separately from a nuclear Schrödinger equation (or its classical counterpart). The electronic Schrödinger equation for the time independent case with the electronic Hamiltonian \hat{H}_e , the electronic wave function $\Psi_e(\{\underline{r}_i\})$ and electronic energy E_e is (we neglect spin for the moment)

$$\hat{H}_e \Psi_e(\{\underline{r}_i\}) = E_e \Psi_e(\{\underline{r}_i\}). \quad (1.1)$$

The wave function $\Psi_e(\{\underline{r}_i\})$ is a function of the coordinate vectors \underline{r}_i ($i = 1, \dots, N_e$), with the number of electrons N_e . Ψ_e depends also parametrically on the nuclear coordinates, $\{\underline{R}_A\}$, which is not explicitly indicated here. The Hamiltonian in atomic units contains the kinetic energy of the electrons, and two Coulomb terms:

$$\hat{H}_e = -\frac{1}{2} \sum_i^{N_e} \nabla_i^2 - \sum_A^{N_A} \sum_i^{N_e} \frac{Z_A}{r_{iA}} + \sum_{i < j}^{N_e} \frac{1}{r_{ij}}. \quad (1.2)$$

1 Methodology

The first term is the kinetic energy operator of the electrons, the second describes the Coulomb interaction between electrons and nuclei (there are N_A nuclei), and the third term gives the Coulomb repulsion between electrons. r_{ij} is the distance between electrons i and j , and r_{iA} denotes the distance between electron i and nucleus A . This equation is written in atomic units for sake of simplicity. In atomic units we have $a_0 = m_e = e = \hbar = 4\pi\epsilon_0 = 1$; a_0 is the Bohr radius, m_e the electron mass, $\hbar = h/(2\pi)$ is the reduced Planck's constant and ϵ_0 is the dielectric constant (of vacuum).

For large systems, the solution of Equation (1.1) gets computationally demanding, which is why further approximations are needed. The approximations used here are based either on wave function theory (WFT) or density functional theory (DFT).

1.2 Wave Function Theory

1.2.1 Hartree-Fock Theory

Hartree-Fock theory (HF) is the simplest WFT to solve the electronic Schrödinger equation. It is based on the approximation of independent particles. The motion of one electron is considered to be only influenced by an averaged field by all other electrons.

The electrons are described by one electron wave functions, the (spatial) orbitals $\psi_i(\underline{r})$. A spatial orbital ψ_i describes the spatial distribution of the electron, such that the probability of finding the electron in the volume element $d\underline{r}$ is given by $|\psi_i(\underline{r})|^2 d\underline{r}$. We assume the spatial orbitals to be orthonormalized:

$$\int \psi_i^*(\underline{r})\psi_j(\underline{r})d\underline{r} = \langle\psi_i|\psi_j\rangle = \delta_{ij}. \quad (1.3)$$

δ_{ij} is the Kronecker delta which is 1 for $i = j$ and 0 else.

To describe an electron completely one has to consider the spin (“up” and “down”), with the spin functions $\alpha(\omega)$, $\beta(\omega)$ with the spin variable ω . For the spin functions we have

$$\int \alpha^*(\omega)\alpha(\omega)d\omega = \langle\alpha|\alpha\rangle = \langle\beta|\beta\rangle = 1 \quad (1.4)$$

and $\langle\alpha|\beta\rangle = \langle\beta|\alpha\rangle = 0$ in the bra-ket notation. Spin orbitals, *e.g.* $\chi(\underline{x}) = \psi(\underline{r})\gamma(\omega)$ with $\gamma = \alpha, \beta$ and $\underline{x} = (\underline{r}, \omega)$ contain information about the position and the spin of the electron.

The simplest ansatz for the total, N_e -electron wave function would be a product of spin orbitals. Since electrons are indistinguishable and fermions with a spin of $1/2$, the wave function must change its sign when interchanging any two electrons (antisymmetry principle):

$$\Psi(\underline{x}_1, \dots, \underline{x}_i, \underline{x}_j, \dots, \underline{x}_{N_e}) = -\Psi(\underline{x}_1, \dots, \underline{x}_j, \underline{x}_i, \dots, \underline{x}_{N_e}). \quad (1.5)$$

This condition is fulfilled in Hartree-Fock theory by using a single Slater determinant, *i.e.* an antisymmetrized product of spin orbitals, as an ansatz for the ground state (“0”), N_e -electron wave function:

$$\Psi_0^{HF}(\underline{x}_1, \dots, \underline{x}_N) = \frac{1}{\sqrt{N_e!}} \begin{vmatrix} \chi_1(\underline{x}_1) & \chi_2(\underline{x}_1) & \dots & \chi_N(\underline{x}_1) \\ \chi_1(\underline{x}_2) & \chi_2(\underline{x}_2) & \dots & \chi_N(\underline{x}_2) \\ \vdots & \vdots & \ddots & \vdots \\ \chi_1(\underline{x}_N) & \chi_2(\underline{x}_N) & \dots & \chi_N(\underline{x}_N) \end{vmatrix}. \quad (1.6)$$

With the variational principle the energy of the system can be minimized:

$$E_{HF} = \langle \Psi_0^{HF} | \hat{H}_e | \Psi_0^{HF} \rangle. \quad (1.7)$$

The best wave function approximated by a single Slater determinant gives the lowest energy. Minimizing the energy with respect to the choice of the spin orbitals results in the Hartree-Fock equations. These are one-electron, non-linear Schrödinger equations for a single electron, called here electron 1 (with spatial coordinate \underline{r}_1). For a closed shell system, after spin has been integrated out, these read:

$$\hat{f}(\underline{r}_1)\psi_i(\underline{r}_1) = \varepsilon_i\psi_i(\underline{r}_1) \quad (1.8)$$

with the orbital energy ε_i and the Fock operator $\hat{f}(\underline{r}_1)$ that is an effective one-electron operator, given in this case as

$$\hat{f}(\underline{r}_1) = \hat{h}(\underline{r}_1) + \sum_{j=1}^{N_e/2} [2\hat{J}_j(\underline{r}_1) - \hat{K}_j(\underline{r}_1)] \quad (1.9)$$

where $\hat{h}(\underline{r}_1) = -\frac{1}{2}\nabla_1^2 - \sum_{A=1}^{N_A} \frac{Z_A}{r_{1A}}$ is the one-electron Hamiltonian, $\hat{J}(\underline{r}_1)$ is the Coulomb operator and $\hat{K}(\underline{r}_1)$ is the exchange operator. \hat{J} refers to the “classical” Coulomb interaction and \hat{K} represents exchange due to the antisymmetry of the wave function. The sum is only to $N_e/2$ because all spatial orbitals are doubly occupied in closed shell systems as considered here.

1 Methodology

The solution of the Hartree-Fock equations gives a set of orthonormal HF orbitals with orbital energies ε_i . The orbitals are occupied according to the aufbau principle (the lowest $N_e/2$ orbitals), further orbitals are unoccupied, also referred to as virtual.

In principle, Equation (1.8) gives an infinite number of solutions. In practice, however, a finite set of K spatial basis functions is introduced, giving K spatial molecular orbitals (or $2K$ spin orbitals). The larger the basis, the lower the expectation value for the energy can be according to the variational principle.

Specifically if we introduce a basis $\{\phi_\mu\}$, *e.g.*, of atomic orbital like functions, the molecular orbitals can be expanded as a sum:

$$\psi_i = \sum_{\mu}^K C_{\mu i} \phi_{\mu} \quad (1.10)$$

The $C_{\mu i}$ are coefficients.

With this we can write the Hartree-Fock equations (1.8) as:

$$\hat{f}(r_1) \sum_{\mu}^K C_{\mu i} \phi_{\mu} = \varepsilon_i \sum_{\mu}^K C_{\mu i} \phi_{\mu}. \quad (1.11)$$

We can deduce the Roothaan-Hall equation, if we use the matrix notation, multiply specific basis functions from the left and integrate:

$$\underline{FC}_i = \underline{SC}_i \varepsilon_i \quad (1.12)$$

with the Fock matrix elements $F_{\mu\nu} = \langle \phi_{\mu} | \hat{f}(r_1) | \phi_{\nu} \rangle$ and the overlap matrix elements $S_{\mu\nu} = \langle \phi_{\mu} | \phi_{\nu} \rangle$ and the orbital energies ε_i . Further, $\underline{C}_i = (C_{1i}, C_{2i}, \dots, C_{Ki})$ is the coefficient vector corresponding to molecular orbital i .

This equation can be solved iteratively with the self consistent field method (SCF) by taking a guess, solving the equation and then improving the guess for the next iteration accordingly, until convergence in energy and/or wave function is reached.

1.2.2 Møller Plesset Perturbation Theory

Hartree-Fock theory contains no electron correlation. In order to include correlation in wave function theory, it is necessary to apply so-called post-HF wave function methods. Although these calculations are significantly more computationally demanding they provide better results on a higher level of theory. From these, Møller Plesset perturbation theory of second order (MP2) [27] is one of the simplest methods to do so. This method is also known for periodic

systems [28]. The method nicely accounts for dynamical correlation and also for dispersion interactions (see below).

We assume that the wave function $\Psi^{(0)}$ is the ground state HF Slater determinant and is known. This however, is no eigenfunction of the electronic Hamiltonian but of an operator made up as the sum of the one-electron Fock operators, which defines an unperturbed reference system in Møller Plesset perturbation theory. In general, in perturbation theory a reference Hamiltonian \hat{H}_0 is perturbed by \hat{V} :

$$\hat{H} = \hat{H}_0 + \lambda\hat{V}. \quad (1.13)$$

\hat{H}_0 is the unperturbed Hamiltonian, here the sum of Fock operators, $\hat{H}_0 = \sum_{i=1}^{N_e} \hat{f}(i)$, λ is a parameter and $\hat{V} = \hat{H} - \hat{H}_0$. In general, \hat{V} is considered as “small”, compared to \hat{H}_0 . The perturbed Schrödinger equation is given by (we refer to a single solution, here only the ground state):

$$(\hat{H}_0 + \lambda\hat{V})\Psi = E\Psi. \quad (1.14)$$

If $\lambda = 0$, then $E = E^{(0)}$, $\hat{H} = \hat{H}_0$ and $\Psi = \Psi^{(0)}$. Generally, the perturbed energy and the perturbed wave function can be written by Taylor expansion around $\lambda = 0$

$$\Psi = \Psi^{(0)} + \lambda\Psi^{(1)} + \lambda^2\Psi^{(2)} + \dots, \quad (1.15)$$

$$E = E^{(0)} + \lambda E^{(1)} + \lambda^2 E^{(2)} + \dots \quad (1.16)$$

The superscript $E^{(n)}$ is the correction at the n -th order of perturbation theory.

Using Equations (1.15) and (1.16) in (1.14) and gathering terms belonging to the same power (n) of λ^n , one obtains in the zeroth order:

$$\hat{H}^{(0)}\Psi^{(0)} = \left(\sum_{i=1}^{N_e} n_i \varepsilon_i\right)\Psi^{(0)}, \quad (1.17)$$

with the HF Slater determinant $\Psi^{(0)}$, the occupation number n_i and the HF orbital energies ε_i .

The unperturbed energy $E^{(0)}$ is therefore:

$$E^{(0)} = \langle \Psi^{(0)} | \hat{H}^{(0)} | \Psi^{(0)} \rangle = \sum_{i=1}^{N_e} \varepsilon_i. \quad (1.18)$$

1 Methodology

In the first order one obtains

$$E^{(1)} = \langle \Psi^{(0)} | \hat{V} | \Psi^{(0)} \rangle = E_{HF} - \sum_{i=1}^{N_e} \varepsilon_i. \quad (1.19)$$

Therefore, the Møller Plesset energy in first order, $E^{(0)} + E^{(1)}$, equals the Hartree-Fock energy E_{HF} . For the energy correction in second order, both occupied orbitals i, j and unoccupied orbitals k, l and their energies ε have to be considered¹:

$$E^{(2)} = \sum_i^{occ.} \sum_{j>i}^{occ.} \sum_k^{unocc.} \sum_{l>k}^{unocc.} \frac{|\langle ij|kl\rangle - \langle ij|lk\rangle|^2}{\varepsilon_i + \varepsilon_j - \varepsilon_k - \varepsilon_l}. \quad (1.20)$$

The MP2-corrected total energy is composed of the HF energy and the second order energy:

$$E_{MP2} = E^{(0)} + E^{(1)} + E^{(2)} = E_{HF} + E^{(2)}. \quad (1.21)$$

The second order energy accounts for electron correlation. However, a main limitation of MP2 is that the wave function of the zeroth order needs to be a good approximation of the real system and the perturbation should be rather small. If the zeroth order wave function describes the system poorly, the corrections need to be higher and eventually, convergence can be slow or not be achieved at all. In this case perturbation theory might not be a good option to describe correlation.

1.3 Density Functional Theory

1.3.1 Basics

An alternative to the wave function-based theories is density functional theory (DFT). It is based on the first Hohenberg-Kohn theorem [29] that connects the ground state electronic energy E_0 to the one-electron density $n(\underline{r}_1)$: there exists a one to one correspondence. If $\Psi(\{\underline{r}_i\})$ is a N_e -electron wave function (spin neglected here for convenience), then the one-electron density can be expressed as

$$n(\underline{r}_1) = N_e \int \dots \int \Psi^*(\underline{r}_1, \underline{r}_2, \underline{r}_3, \dots, \underline{r}_N) \Psi(\underline{r}_1, \underline{r}_2, \underline{r}_3, \dots, \underline{r}_N) d\underline{r}_2 \dots d\underline{r}_N \quad (1.22)$$

¹ $\langle ij|kl\rangle = \int \int \chi_i^*(1) \chi_j^*(2) \frac{1}{r_{12}} \chi_k(1) \chi_l(2) d\underline{x}_1 d\underline{x}_2$

if the wave function is normalized to 1. The second Hohenberg-Kohn theorem, also called “the variational principle of DFT”, proves that a test density $n'(\underline{r}_1)$ will give a higher or the same energy as the exact density:

$$E_0^{exact} \leq E_0^{HK}[n'(\underline{r}_1)]. \quad (1.23)$$

The total energy $E[n]$ can be determined as a consequence of the first Hohenberg-Kohn theorem as

$$E[n] = T[n] + V_{ext}[n] + V_{ee}[n] = T[n] + \int n(\underline{r}_1)v_{ext}(\underline{r}_1)d\underline{r}_1 + E_H[n] + E_{xc}[n] \quad (1.24)$$

with the kinetic energy $T[n]$, the “external” potential energy $V_{ext}[n]$ (from interaction of electrons with nuclei and possible external fields) and the electron electron interaction $V_{ee}[n]$. Further, the external potential is given as $v_{ext}(\underline{r}_1) = -\sum_{A=1}^{N_A} \frac{Z_A}{r_{1A}}$ in the absence of external fields, and the Hartree energy as $E_H[n] = \int \frac{n(\underline{r}_1)n(\underline{r}_2)}{r_{12}}d\underline{r}_1d\underline{r}_2$, corresponding to the classical Coulomb interaction. Finally the exchange correlation energy $E_{xc}[n]$ describes the non-classical exchange correlation interactions to be defined later.

A major advantage of DFT over wave function-based methods is the size of the variational problem: without spin, only a three dimensional quantity has to be optimized for three spatial coordinates $n(x_1, y_1, z_1)$ in DFT, instead of a $3N_e$ -dimensional quantity, $\Psi_e(\underline{r}_1, \dots, \underline{r}_{N_e})$ in the case of WFT.

Problematic in this approach is that the exact form of the interacting kinetic energy $T[n]$ and the exchange correlation functional² $E_{xc}[n]$ are unknown, except for simple model cases.

1.3.2 Kohn-Sham Equations and Choice of Exchange-Correlation Functionals

Initial attempts to calculate all energy components from the pure density were not very successful because the exact form of $T[n]$ and $E_{xc}[n]$ is not known and approximations, especially the ones for $T[n]$, delivered poor results so that instead wave function-based methods were applied commonly. In 1965 Kohn and Sham showed in their work [30] that the kinetic energy can be calculated from non-interacting auxiliary particles in a set of orbitals that is used for representing the “exact” electron density. The use of orbitals makes it possible to avoid a

² To clarify the difference between a function and a functional: in a function (*e.g.* $f(x)$), a number is produced by a set of variables, whereas a functional ($F[f]$) gives a number from a function which depends on variables.

1 Methodology

direct calculation of $T[n]$ [24]. A variational calculation similar to HF leads to the so-called Kohn-Sham equations:

$$\left(-\frac{1}{2}\nabla_1^2 + v_{ext}(\underline{r}_1) + v_H(\underline{r}_1) + v_{xc}(\underline{r}_1)\right) \psi_i^{KS}(\underline{r}_1) = \varepsilon_i^{KS} \psi_i^{KS}(\underline{r}_1). \quad (1.25)$$

Here, the density is calculated in the closed shell case as

$$n(\underline{r}_1) = \sum_{i=1}^{N_e/2} 2|\psi_i^{KS}(\underline{r}_1)|^2 \quad (1.26)$$

and the kinetic energy as

$$T[n] = \sum_{i=1}^{N_e/2} 2\langle \psi_i^{KS} | -\frac{1}{2}\nabla_1^2 | \psi_i^{KS} \rangle \quad (1.27)$$

from Kohn-Sham orbitals ψ_i^{KS} . Further, Equation (1.25) contains the external potential $v_{ext}(\underline{r}_1)$, the Hartree potential $v_H(\underline{r}_1)$, the exchange-correlation potential $v_{xc}(\underline{r}_1) = \frac{\delta E_{xc}[n]}{\delta n(\underline{r}_1)}$ (where $\frac{\delta E}{\delta n}$ notes a functional derivative), and the orbital energy ε_i^{KS} . In this way, the energy can be determined self-consistently. With this, the exchange-correlation functional ($E_{xc}[n]$) remains the only unknown functional.

Several levels of theory with increasing accuracy were developed to approximate $E_{xc}[n]$. The local density approximation (LDA) is the simplest of those approaches using known expressions for $E_{xc}[n]$ from the homogeneous electron gas model. Although this is a very basic approximation it delivers still reasonable results. Better results can be achieved when the density and the first derivative (gradients) are considered, defining the generalized gradient approximation (GGA):

$$E_{xc} = E_{xc}[n(\underline{r}_1), \nabla n(\underline{r}_1)]. \quad (1.28)$$

Here, one of the most prominent and widely used functionals is PBE, introduced by Perdew, Burke and Ernzerhof in 1996 [31, 32]. PBE is implemented without any parameters fitted to experimental results and is known to give reasonable results for a wide range of applications.

Even more accurate results can be gained by mixing into the functional some amount of exact Hartree-Fock like exchange, these are called hybrid functionals. At least for molecular systems these are the most widely applied functionals, for example B3LYP [33, 34] and HSE06 [35].

1.3.3 Hybrid Functionals

When using hybrid functionals, a fraction of “exact exchange” (HF-like exchange) is mixed into the functional. For this we split the exchange correlation functional up into two parts:

$$E_{xc}[n(\mathbf{r}_1)] = E_x[n(\mathbf{r}_1)] + E_c[n(\mathbf{r}_1)]. \quad (1.29)$$

The exchange part contains a HF-like exchange contribution, and a part coming from a (non-hybrid) DFT functional:

$$E_x = aE_x^{HF} + (1 - a)E_x^{DFT}. \quad (1.30)$$

The parameter a determines the amount of exact Hartree-Fock exchange. As an example, the functional B3LYP uses 20% of exact exchange [36], $a = 0.2$. The B3LYP functional also uses different contributions (LDA and LYP=GGA) to the correlation energy,

$$E_{xc}^{B3LYP} = (1 - a)E_x^{LDA} + aE_x^{HF} + b(E_x^{B88} - E_x^{LDA}) + cE_c^{LYP} + (1 - c)E_c^{LDA}, \quad (1.31)$$

with the other two parameters, $b = 0.72$ and $c = 0.81$ being empirical parameters, like a .

Hybrid functionals are very popular for many computational applications because they deliver very good results although they need more computation time than GGA functionals (such as PBE).

1.3.4 Dispersion Corrections

A weakness of DFT is their inaccuracy in reproducing some intermolecular interactions like van der Waals interactions. To overcome this problem it is possible to add dispersion corrections. These are important, especially for the adsorbate-surface interaction and the adsorbate-adsorbate interaction. In the work of Grimme [37] and coworkers corrections for attractive dispersion interactions contributing to van der Waals interactions were developed and implemented to overcome this issue; these range from D over D2 to D3 corrections. In this work, D2 and D3 corrections were used. For the dispersion corrected energy, the dispersion energy has to be subtracted from the DFT based energy:

$$E_{DFT+D2/3} = E_{KS-DFT} - E_{disp}^{(2)/(3)} \quad (1.32)$$

The D2 correction describes pair interactions between atoms A and B in the form

$$E_{disp}^{(2)} = \sum_A \sum_{B>A}^{N_A} s_6 \frac{C_{AB}}{R_{AB}^6} f_{damp}(R_{AB}), \quad (1.33)$$

1 Methodology

with the number of atoms N_A , the scaling factor s_6 which is dependent on the functional, the averaged dispersion coefficient C_6^{AB} , the interatomic distance R_{AB} and a damping function $f_{damp}(R_{AB})$. For the more advanced D3 method, $E_{disp}^{(2)}$ is altered as follows:

$$E_{disp}^{(3)} = E_{disp}^{(2)} - \sum_A \sum_{B>A}^{N_A} s_8 \frac{C_8^{AB}}{R_{AB}^8} f_{damp}(R_{AB}) + \sum_A \sum_{B>A}^{N_A} \sum_{C>B}^{N_A} f_{damp}(\bar{R}_{ABC}) \frac{C_9^{ABC} (3 \cos \gamma_a \cos \gamma_b \cos \gamma_c + 1)}{(R_{AB} R_{BC} R_{AC})^3}. \quad (1.34)$$

Here, s_8 is a scaling factor, C_8^{AB} and C_9^{ABC} are averaged dispersion coefficients, γ_i are the angles of the corresponding triangle that is built by the three atoms A, B and C, and $C_9^{ABC} = \sqrt{C_6^{ABC} C_6^{BC} C_6^{AC}}$ and $\bar{R}_{ABC} = \sqrt[3]{R_{AB} R_{BC} R_{AC}}$ is the geometrically averaged distance of the three atoms.

1.4 Periodic Boundary Conditions

Solid-state systems such as surfaces can either be simulated by calculating cluster models that were “cut” from the surface and represent an important part of the system or can be treated as the whole system with a periodic approach. These periodic systems can be described by a unit cell and respective cell vectors, which are used to generate the infinite system by repeating the cell in each direction. This can be either realized in 1D (polymers), 2D (surfaces) or 3D (bulk crystals). Surfaces can also be described within the 3D model as a slab by three dimensional repetition of the unit cell. The third dimension includes a vacuum gap between two slabs (supercell model of a surface) in the direction perpendicular to the surface (here z). This gap has to be large enough to prevent unit cells from influencing each other in this direction and therefore lead to unphysical behavior between the surface atoms and atoms of the neighboring slabs above or below. In standard bulk and surface system software like VASP [38–42] it is not (yet) possible to mimic a 2D system, so that in the main part of this work this vacuum gap 3D model was applied. Some programs, however, (such as CRYSTAL [43]) deliver the opportunity to calculate 2D systems, repeating the slab periodically only in x/y, respectively. The corresponding results are presented in Section 2.2.

A 3D unit cell can be described by the three basis vectors of the lattice, \underline{a} , \underline{b} and \underline{c} and can be translated along these vectors to gain the infinite system [23]. The Bravais lattice is built by positions that are repeated periodically by the translational vectors. In three dimensional systems 14 different forms exist, *e.g.* hexagonal hcp. The lattice can be described in direct space by the lattice vector \underline{B} with the base vectors \underline{a} , \underline{b} , \underline{c} and integers n_i ($i = 1, 2, 3$):

$$\underline{B} = n_1 \underline{a} + n_2 \underline{b} + n_3 \underline{c}. \quad (1.35)$$

Similarly, a reciprocal space exists (the so-called k -space) which can be defined analogously to Equation (1.35) by reciprocal lattice vectors \underline{G} and a set of reciprocal base vectors $\bar{\underline{a}}, \bar{\underline{b}}, \bar{\underline{c}}$ and h, k, l being integers:

$$\underline{G} = h\bar{\underline{a}} + k\bar{\underline{b}} + l\bar{\underline{c}}. \quad (1.36)$$

The dimension of these vectors is m^{-1} .

A relation between direct and reciprocal lattice vectors is

$$e^{i\underline{G}\underline{B}} = 1. \quad (1.37)$$

Between the vectors of the direct and the reciprocal space there are fixed relations: the vectors $\bar{\underline{a}}, \bar{\underline{b}}, \bar{\underline{c}}$ can be derived from $\underline{a}, \underline{b}, \underline{c}$, by

$$\bar{\underline{a}} = 2\pi \frac{\underline{b} \times \underline{c}}{\underline{a} \cdot (\underline{b} \times \underline{c})} \quad (1.38)$$

and analogous for $\bar{\underline{b}}$ and $\bar{\underline{c}}$. Further, direct and reciprocal base vectors are perpendicular to each other:

$$\underline{i} \cdot \bar{\underline{j}} = 2\pi\delta_{ij}, \quad (1.39)$$

with $\underline{i} = \underline{a}, \underline{b}, \underline{c}$, $\bar{\underline{j}} = \bar{\underline{a}}, \bar{\underline{b}}, \bar{\underline{c}}$.

The Wigner-Seitz cell is a special primitive cell with a single lattice point in its center and reflects the full symmetry of the Bravais lattice. In the reciprocal lattice this is also referred to as first Brillouin zone, whose center is the Γ -point ($h = k = l = 0$). It is a uniquely defined primitive cell in reciprocal space that contains all critical points of interest. The integers h, k , and l from Equation (1.36) are also called Miller indices and can be used to describe the crystallographic planes (position of the surface in the coordinate system). They are determined by finding the point of intersection of the surface plane with the axes of the coordinate system, reducing, then taking the reciprocal values and multiplying with the least common multiple to obtain three integers. The vector made from these indices is analogous to the surface normal in the reciprocal space.

Within the hexagonal (and rhombohedral) lattice system, also the Miller-Bravais notation with four indices $[h, k, i, l]$ can be used. Here, i is redundant and can be defined by h and k : $i = -(h+k)$. For example, the (110) surface would be referred to as $(11-(1+1)0) = (11\bar{2}0)$. Note that the minus sign is expressed by the overbar. The advantage of this notation is that one can identify symmetry-equivalent planes easily. To express a direction vector in the basis of the direct lattice vectors, the notation $[uvw]$ is used. In general this vector is not perpendicular to the plane (uvw) , only for cubic lattices this is the case.

1 Methodology

To describe a periodic system with quantum mechanical methods, one has to introduce periodic boundary conditions. According to the Bloch theorem [44], the wave function can be expressed by a phase factor and a periodic function $u_{\underline{k}}(\underline{r})$

$$\phi(\underline{r}) = e^{i\underline{k}\underline{r}}u_{\underline{k}}(\underline{r}) \quad (1.40)$$

with the periodicity

$$u_{\underline{k}}(\underline{r}) = u_{\underline{k}}(\underline{r} + \underline{B}) \quad (1.41)$$

$$\phi(\underline{r} + \underline{B}) = e^{i\underline{k}(\underline{r} + \underline{B})}u_{\underline{k}}(\underline{r}) = e^{i\underline{k}\underline{B}}\phi(\underline{r}) \quad (1.42)$$

In case of periodic HF, we express the electronic wave function with the help of orbitals, which are now crystal rather than molecular orbitals. They depend on a band index (n , in analogy to the MO index i), and on the \underline{k} -value within the first Brillouin zone above):

$$\psi_n(\underline{r}) \rightarrow \psi_{n,\underline{k}}(\underline{r}). \quad (1.43)$$

The $\psi_{n,\underline{k}}(\underline{r})$ can be expanded, similar to the MOs, in a basis.

If the crystal orbital $\psi_{n,\underline{k}}(\underline{r})$ is represented by an atomic orbital basis (AO, compare Equation (1.10)), then one obtains in the HF case the following Roothaan-Hall equations:

$$\underline{\underline{F}}^{\underline{k}}\underline{\underline{C}}_n^{\underline{k}} = \underline{\underline{S}}^{\underline{k}}\underline{\underline{C}}_n^{\underline{k}}\varepsilon_n^{\underline{k}} \quad (1.44)$$

Here, $\underline{\underline{C}}_n^{\underline{k}}$ contains the AO coefficients of band n at \underline{k} -point \underline{k} . Further $(\underline{\underline{F}})_{\underline{\mu}\underline{\nu}}^{\underline{k}} = \sum_j e^{i\underline{k}\underline{B}_j} f_{\underline{\mu}\underline{\nu}}^{0j}$ with $f_{\underline{\mu}\underline{\nu}}^{0j} = \langle \phi_{\underline{\mu}}^0 | \hat{f} | \phi_{\underline{\nu}}^j \rangle$ are the Fock matrix elements (here $\phi_{\underline{\mu}}^i$ is the AO μ in cell i with position vector \underline{B}_i with $i = 0, j$ where 0 denotes the reference cell and j the cell with position vector \underline{B}_j) and $(\underline{\underline{S}})_{\underline{\mu}\underline{\nu}}^{\underline{k}} = \sum_j e^{i\underline{k}\underline{B}_j} s_{\underline{\mu}\underline{\nu}}^{0j}$ with $s_{\underline{\mu}\underline{\nu}}^{0j} = \langle \phi_{\underline{\mu}}^0 | \phi_{\underline{\nu}}^j \rangle$ the overlap matrix. Equation (1.44) is solved for a finite number of \underline{k} -points in the first Brillouin zone, for K bands.

In the periodic case of MP2, here a further development, the so-called local Møller Plesset perturbation theory of second order [45–47] is applied, as implemented in CRYSCOR [48] for periodic systems. In contrast to regular MP2 that scales with $\mathcal{O}(N^5)$, local MP2 allows for scaling of $\mathcal{O}(N)$ with the number of atoms per unit cell N so that it is considerably faster and more efficient also for larger systems. This is gained by a description of the electron correlation by localized orbitals (Wannier functions) since dynamical correlation is not a long-range effect but can be analyzed locally. As a disadvantage large basis sets are needed so that on top of the regular HF calculation a dual basis set expansion is recommended [49].

Density functional theory in the Kohn-Sham scheme for periodic boundary conditions is analogous to HF, where equations analogous to the Roothaan-Hall Equation (1.44) can be

solved with respective periodic Kohn-Sham orbitals. The DFT integrals can be evaluated in real space over the extended system but also by integrals over a finite number of points in the first Brillouin zone in reciprocal space (\underline{k} -point grid). Due to symmetry considerations only a reduced number of \underline{k} -points need to be evaluated (\underline{k} -points in the irreducible part of the first Brillouin zone).

1.5 Plane Wave Bases, Atom Centered Bases and Peculiarities

It is necessary for calculation of Equations (1.8) and (1.25) to use a basis set for the orbitals, as shown in Equation (1.10). Basically there are two different types of bases, atom centered basis sets and plane waves. Both types are used in this work so we introduce advantages and disadvantages [50].

When using a plane wave basis, for solid state systems both the energy and the gradient converge better (fewer steps). The system is intrinsically described periodically in 3D (no matter if the system is a 1D (polymer), 2D (surface) or 3D system (bulk)). It is possible to improve the basis systematically by setting the cutoff energy higher, which defines the number of basis functions that are considered in representing the single-particle wave functions in DFT, for example:

$$\psi_{n,\underline{k}}(\underline{r}) = \frac{1}{\sqrt{V}} \sum_{\underline{G}} C_{\underline{G}n} e^{i(\underline{k}+\underline{G})\underline{r}}, \quad (1.45)$$

where V is the cell volume and $C_{\underline{G}n}$ are the complex Fourier coefficients.

$$E_{cutoff} = \max_{\underline{k}+\underline{G}} \frac{|\underline{k} + \underline{G}|^2}{2} \quad (1.46)$$

That is, one includes plane waves up to the maximum $\underline{k}+\underline{G}$ values considered in the calculation.

The basis is not geometry dependent. Treating all electrons requires very high cutoff energies which are computationally unfeasible, so usually pseudopotentials are used, where core electrons are not treated explicitly but their presence is considered indirectly. On the negative side, when norm-conserving pseudopotentials are applied more memory is needed. To treat this, the PAW (projector augmented-wave method) [51, 52] is applied which delivers explicit treatment of the core electrons so that the accuracy is greatly increased. The system is intrinsically defined in 3D. For a good convergence however, many basis functions are necessary which is very costly, especially for calculations that depend not only on the density (like hybrid functionals or MP2). It is computationally demanding to calculate exact (Fock) exchange, which makes the use of hybrid functionals so costly, although the precision of the results is considerably enhanced. In addition, for treating surface systems, an "empty space", vacuum gap has to be

considered, which increases the computational costs.

For atom centered bases, the basis functions correspond to atomic orbitals. The use of only a small basis set already gives good results, relatively few basis functions are necessary. However, the basis is geometry dependent: whenever there are atom centered basis sets the orbitals of different atoms can overlap. This can result in the so-called basis set superposition error (BSSE) [53], which is not a problem for the plane wave basis. Let's assume a dissociation reaction: in the molecular case, the electrons can occupy orbitals of both residues (each atom has in total a higher basis set, the binding energy is stabilized), whereas in the dissociated case, this is not possible (the energy of the isolated fragments is not stabilized). Due to this difference, it is necessary to either correct the BSSE or to use a large basis, ideally at the basis set limit. By adding more basis functions, computational costs increase and linear dependencies can also be a problem, so that it makes sense to apply further corrections. With these so-called counterpoise corrections (CP) [53] one can approximately compensate for this error. This is done here by performing "ghosted" calculations with the system as a whole, the adsorbate alone, and the adsorbate with surface from ghost atoms. Then one applies a subtractive scheme to cancel out the effect of the orbital overlap.

Probably, the most powerful advantage of atom centered bases is that exact exchange and hybrid methods are available as standard methods because fewer basis functions are required, compared to plane waves.

1.6 *Ab Initio* Molecular Dynamics

Apart from solving stationary problems, *ab initio* molecular dynamics (AIMD) can deliver dynamical results for time dependent processes [23, 54]. This is useful for simulating transport/diffusion processes as well as spectral properties. In AIMD, the classical Newtonian equations of motion are solved

$$-\nabla_A V(\{\underline{R}_i\}) = M_A \frac{d^2 \underline{R}_A(t)}{dt^2} \quad (1.47)$$

where V is the potential energy that is a function of all nuclear coordinates $\{\underline{R}_i\}$, \underline{R}_A is the vector containing all coordinates of atom A , M_A is the nuclear mass of atom A and t is the time. The classical approximation is often a good one for nuclei, if they are sufficiently massive³.

³ Strictly speaking, this is not appropriate for hydrogen, since it is so lightweight that quantum effects can not be precluded. For treating quantum effects such as zero point energy and tunneling it is necessary to solve the nuclear Schrödinger equation, or to use path integral molecular dynamics [55].

In contrast to classical molecular dynamics (as opposed to "ab initio"), where predefined potentials or force fields based on empirical data are used, in *ab initio* MD the potential and the respective (Hellmann-Feynman) forces are calculated "on-the-fly" at each time step, with the help of the chosen *ab initio* method (*e.g.* DFT). This has the advantage that no further parameterization is necessary when changing atoms, molecules or surfaces. Also, the method is especially suited for reactions or dissociation processes like those considered in this work. In particular, the dissociative and molecular sticking of water molecules on an alumina surface will be studied below.

As starting conditions, positions $\underline{R}_A(t)$ and velocities \underline{v}_A of the nuclei have to be specified. Between two time steps of the propagation there is a time span Δt . The time propagation can be executed numerically with the Verlet algorithm [56], delivering the trajectory $\underline{R}_A(t)$ for each atom A . In the algorithm, by using

$$\underline{R}_A(t + \Delta t) = \underline{R}_A(t) + \underline{v}_A(t) \cdot \Delta t + \frac{1}{2} \underline{a}_A(t) \cdot \Delta t^2 + \dots \quad (1.48)$$

$$\underline{R}_A(t - \Delta t) = \underline{R}_A(t) - \underline{v}_A(t) \cdot \Delta t + \frac{1}{2} \underline{a}_A(t) \cdot \Delta t^2 \pm \dots \quad (1.49)$$

the previous and next time steps are approximated by a Taylor expansion with the velocity $\underline{v}_A(t)$ of atom A (the derivative of the coordinates with respect to time t , $\frac{\partial \underline{R}_A}{\partial t}$), and the acceleration $\underline{a}_A(t) = \frac{\partial^2 \underline{R}_A}{\partial t^2}$. These two equations are usually Taylor expanded to third order. Adding Equations (1.48) and (1.49) one can predict the positions at a later time step from the current and the previous positions and the acceleration:

$$\underline{R}_A(t + \Delta t) = 2\underline{R}_A(t) - \underline{R}_A(t - \Delta t) + \underline{a}_A(t)(\Delta t)^2 + \dots \quad (1.50)$$

The acceleration is evaluated at each time step from the potential gradient as

$$\underline{a}_A(t) = -\frac{1}{M_A} \frac{\partial V}{\partial \underline{R}_A}. \quad (1.51)$$

The time step Δt is an important parameter: It has to be small enough to describe the fastest processes of interest, but not too small to achieve reasonable total computation times. It is typically around 10^{-15} s. For comparison, a molecular vibration of 3000 cm^{-1} corresponds to a vibrational frequency of $\approx 10^{14} \text{ s}^{-1}$, *i.e.* a vibrational period of 10^{-14} s. On the other hand, a sufficiently long time of the trajectory has to be propagated to measure all chemically relevant processes. In this work we usually consider propagation times up to about 1-2 ps. Additionally, it may be necessary to compute several trajectories instead of just a single one for reasonable averaging.

1 Methodology

The AIMD simulations are characterized by the following thermodynamic parameters: total energy E , temperature T , volume V , pressure p , number of particles N and the chemical potential μ . The corresponding ensemble is named after the fixed quantities, *e.g.* NVT (=canonical) and NVE (=microcanonical).

In a microcanonical ensemble (NVE) the system is isolated (it can not exchange particles or energy with the surroundings) and the total energy E is fixed. This type of MD is deterministic, since no random processes are involved. Computationally this is easily implemented. In many experiments however, usually the temperature rather than the energy is fixed. Then, a canonical ensemble (NVT) is appropriate where the system is coupled in thermal equilibrium with a heat bath, also referred to as thermostat. T (on average) is given by the temperature of the thermostat. For this thermostat, several models are available. In this work the Nosé-Hoover thermostat [57–59] is used. The heat bath is realized by a fictitious particle which is propagated like real particles of the system and acts like a reservoir of energy for the heat bath. Here, the trajectory is subject to random perturbations along the trajectory. Multiple simulations have to be performed in order to gain reliable statistics.

1.7 Vibrational Spectroscopy: Frequencies and Intensities

In surface science vibrational spectroscopy is an important tool to characterize molecular adsorbates. One theoretical approach to simulate such spectra is to calculate vibrational frequencies and (IR-) intensities for minimum structures of the potential energy surface (PES). A characteristic of minima and stationary points in general is that the derivatives with respect to all nuclear coordinates equal zero. For stationary points the eigenvalues and -vectors of the Hessian matrix \underline{H} are of interest. The elements of this Hessian are the derivative of the potential V with respect to coordinates i and j ($i, j = 1, \dots, 3N_A$, where N_A is the number of atoms (per cell)):

$$H_{ij} = \left(\frac{\partial^2 V}{\partial Q_i \partial Q_j} \right) \Big|_{Q_i=Q_j=0} = \left(\frac{1}{\sqrt{m_i m_j}} \frac{\partial^2 V}{\partial R_i \partial R_j} \right) \Big|_{R_i=R_j=0} . \quad (1.52)$$

Here, Q_i are mass weighted coordinates $Q_i = \sqrt{m_i} R_i$, with the mass m_i corresponding to coordinate i and the displacement from the equilibrium positions, R_i . With this, the following eigenvalue problem has to be solved:

$$\underline{H} \underline{A}_i = \lambda_i \underline{A}_i, \quad (1.53)$$

1.7 Vibrational Spectroscopy: Frequencies and Intensities

with the eigenvectors \underline{A}_i , and the eigenvalues λ_i that are squares of vibrational frequencies ω_i :

$$\omega_i = \sqrt{\lambda_i}. \quad (1.54)$$

Within this approach, all frequencies are delivered in the harmonic approximation. Note, although we consider periodic systems, the vibrations here are only calculated at the Γ -point, *i.e.* formally corresponding atoms in different cells move in phase.

At minima, all eigenvalues are positive ($\lambda_i \geq 0 \forall i$). This could be the educts or products of a reaction. In this case frequencies ω_i are real and can be interpreted as vibrational frequencies, *e.g.*, for vibrational spectroscopy. Another important case is, if there is only a single negative eigenvalue, which gives one imaginary frequency according to Equation (1.54). In a mathematical sense this is a saddlepoint of first order and can be interpreted as a transition state of a chemical reaction. How to find these points is described in Section 1.8.

We want to compare to experimental SFG (sum frequency generation) spectra, for this it is our desire not only to calculate frequencies but also intensities. However, in this work IR intensities are calculated instead, with two different methods (with the dipole model (I) and Born effective charges (II)). Also, the vibrational density of states ((III), VDOS, via velocity-velocity autocorrelation functions) is evaluated. None of those methods delivers intensities for SFG spectroscopy, but can be seen as approximations to them [60].

- I) In the dipole model, we approximate an IR spectrum polarized perpendicular (z-direction) to the surface. This was done, because only modes with a high perpendicular component can be measured in respective SFG spectra. Further, we invoke the double harmonic approximation, *i.e.*, vibrational modes are treated in harmonic approximation, and the z component of the dipole moment is approximated as

$$\mu_z(\tilde{Q}_1, \dots, \tilde{Q}_{3N_A}) = \mu_z(0) + \sum_{i=1}^{3N_A} \frac{\partial \mu_z}{\partial \tilde{Q}_i} \Big|_{\tilde{Q}_1=\tilde{Q}_2=\dots=0} \cdot \tilde{Q}_i, \quad (1.55)$$

where $\mu_z(0)$ is the dipole moment at the equilibrium geometry, and \tilde{Q}_i are the displacements of normal modes from equilibrium. Assuming for the moment a single normal mode, \tilde{Q}_n , in the double harmonic approximation the intensity for IR induced dipole transition from $\phi_{\nu=0}^{(n)}(\tilde{Q}_n)$ to $\phi_{\nu=1}^{(n)}(\tilde{Q}_n)$ is, according to Fermi's golden rule,

$$I_{\mu}^{(n)} \propto |\langle \phi_0^{(n)}(\tilde{Q}_n) | \frac{\partial \mu_z}{\partial \tilde{Q}_n} | 0 \cdot \tilde{Q}_n | \phi_1^{(n)}(\tilde{Q}_n) \rangle|^2 \quad (1.56)$$

1 Methodology

$$I_{\mu}^{(n)} \propto \mu_{z,n}^{\prime 2} \frac{\hbar}{2m_{red}^{(n)}\omega_n} \quad (1.57)$$

where $\mu_{z,n}^{\prime} = \frac{\partial \mu}{\partial Q_n} |_0$, $m_{red}^{(n)}$ is the reduced mass of mode \tilde{Q}_n and the $\phi_i^{(n)}$ are the vibrational eigenfunctions.

In practice, *e.g.* in VASP, the vibrational frequencies are calculated numerically by displacing each atom. For each displaced structure we obtain a dipole moment (here only in z-direction). From the difference in dipole moment for the equilibrium position and the displaced one, we can calculate the derivative of the dipole moment for each atom individually. Since we know the displacement of each atom for each normal mode, we can add the contributions to the dipole moment (and its derivative) to gain the intensity according to Equation (1.57). With this, in the harmonic approximation, using normal modes, the total dipole spectrum is then given as [61, 62]

$$I_{\mu}(\omega) \propto \sum_{n=1}^{3N_A} I_{\mu}^{(n)} \cdot \delta(\omega - \omega_n). \quad (1.58)$$

- II) Another way to obtain IR intensities for periodic systems is by applying density functional perturbation theory (DFPT) [63, 64], which is a linear response theory. Within this approach a Born effective charge matrix is determined [65]. These charges can be understood as coefficients that are related to the change of the polarization due to displacing an atom. They can be expressed as the derivative of the macroscopic polarization in a (cartesian) direction β , with respect to the displacement of an atom i in a direction α , $\tau_{i\alpha}$, as⁴

$$Z_{\alpha\beta}^*(i) = \frac{\partial P_{\alpha}}{\partial \tau_{i\alpha}}. \quad (1.59)$$

One can calculate the contribution $I_{BEC}^{(n)}$ [66, 67] of mode n to the total IR intensity, as published in the work of Grillo *et al.* [68]⁵:

$$I_{BEC}^{(n)} \propto \sum_{\alpha=1}^3 \left| \sum_{i=1}^{N_A} \sum_{\beta=1}^3 Z_{\alpha\beta}^*(i) e_{\beta}^{(n)}(i) \right|^2. \quad (1.60)$$

Here, α and β range over three cartesian directions (1, 2, 3 for x, y, z), $e_{\beta}^{(n)}(i)$ is the β component of atom i in the normalized vibrational eigenvector of the n -th mode, N_A is

⁴ Strictly speaking, the dimension of P is $[\frac{Asm}{m^3}]$, but in this work it is not divided by the cell volume.

⁵ In their work, Grillo *et al.* [68] calculate HREELS spectra, but the software also computes IR intensities.

the total number of atoms in the unit cell. It is possible to weight the results to consider a fictional beam angle, corresponding to weights for x , y and z . Here an angle of 45° is applied. For this the sum over α in Equation (1.60) is split into three parts⁶, where x , y is weighted with 0.5 and z with $1/\sqrt{2}$.

A total IR intensity is then given as

$$I_{BEC}(\omega) \propto \sum_{n=1}^{3N_A} I_{BEC}^{(n)} \times \delta(\omega - \omega_n). \quad (1.61)$$

Note, that both methods are based on normal mode analyses and Equations (1.58) and (1.61) give stick spectra. While normal modes are a good approximation for high energy vibrations, for example OH stretch vibrations, they become worse for low energy lattice vibrations, for which the minima are typically more shallow.

III) As a fundamentally different method, power spectra can be calculated from *ab initio* MD trajectories [69]. This is carried out by analyzing the velocity of the atoms along the trajectories, giving the vibrational spectrum via Fourier transformation of the velocity-velocity autocorrelation function:

$$VDOS(\omega) \propto \sum_{i=1}^{N_A} \int_0^{+\infty} \langle \underline{v}_i(t) \cdot \underline{v}_i(0) \rangle e^{i\omega t} dt. \quad (1.62)$$

VDOS is the vibrational density of states as a function of the frequency ω , which is obtained by summing over all N_A atoms, and then Fourier transform the ensemble average of the velocity-velocity autocorrelation function $\langle \underline{v}_i(t) \cdot \underline{v}_i(0) \rangle$. $\underline{v}_i(0)$ and $\underline{v}_i(t)$ are the atomic velocities at time 0 and a later time, t , respectively. In practice one only integrates from 0 to a finite propagation time, t_{prop} . The resulting spectra implicitly include anharmonic effects and mode couplings. Also, the thermal motion of the atoms is taken into account [70, 71], giving rise to broadened spectra.

1.8 Transition States and Kinetics

In the Born-Oppenheimer approximation [26], nuclear and electronic degrees of freedom are separated. In this picture, stable systems are minima on the PES and chemical reactions can be understood as nuclei moving on the PES from educt to product valleys. On a multi-

⁶ The z -component is calculated as $\cos \theta = \cos(\pi/4) = \frac{1}{\sqrt{2}}$. It is then $x = y$ and for $x^2 + y^2 + z^2 = 1$ we obtain values for $x = y = 0.5$.

1 Methodology

dimensional PES, one can define an energetically most favorable reaction path, which is the minimum energy path, MEP, see Figure 1.1. The highest point along the MEP is called the transition state (TS). As mentioned before, in a multi-dimensional space this is a first-order saddle point.

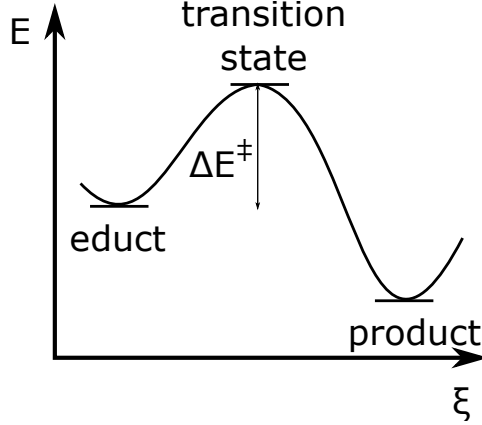


Figure 1.1: Schematic view of a minimum energy path (MEP) with coordinate ξ for a chemical reaction. The activation energy $\Delta E^\ddagger = E_{TS} - E_{educt}$ for the reaction is also shown.

Transition state theory is a semi-classical theory: dynamics along the reaction coordinate ξ are treated classically, but perpendicular modes are treated quantum mechanically in harmonic approximation.

Once a transition state is found (see below), ΔE^\ddagger and also the corresponding activation free energy

$$\Delta G^\ddagger = G_{TS} - G_{educt} \quad (1.63)$$

can be computed, where $G = H - TS$. The free energy G is a sum of the components for translation, rotation and vibration: $G_{trans} + G_{rot} + G_{vib}$, where only the latter is non zero for reactions studied in this work, where educts and transition state species are adsorbed at a surface. It can also be expressed by the sum of the SCF energy (E_{SCF}) and the vibrational component of the Gibbs free energy using the vibrational frequencies ν_i from a normal mode analysis:

$$G = E_{SCF} + G_{vib} = E_{SCF} + \sum_{i=1}^{N_A} \left(\frac{h\nu_i}{2} + k_B T \ln(1 - e^{-h\nu_i/(k_B T)}) \right). \quad (1.64)$$

With ΔG^\ddagger , reaction rates $k(T)$ can be calculated with the help of transition state theory, according to Eyring [72, 73]:

$$k(T) = \kappa \frac{k_B T}{h} e^{-\Delta G^\ddagger(T)/(k_B T)}. \quad (1.65)$$

Here, κ is a correction factor (accounting for, *e.g.*, tunneling), which we won't use here. k_B is Boltzmann's constant k_B . The equation gives the reaction rate constant as a function of temperature. Note that this equation is only valid for cases where all reactants reaching the TS react to the product site. No re-crossing is employed, so the rate is an upper limit in the classical picture.

For the barrier height one needs to find the free energies of the transition state and the educt. The educt geometry can simply be obtained by geometry optimization as a minimum on the PES. Among different methods to find the transition state geometry, we used nudged elastic band calculations (NEB) [74], with climbing image [75]. This method approximates the reaction path as a series of associated images, which are connected via spring forces. These spring forces prevent the images from optimizing into the local minimum next to the transition state. First a regular NEB, then on top of this climbing image was applied which gives better convergence. In NEB calculations the energetically highest image is "optimized" towards higher energies in the opposite direction of the potential gradient. Any point found by this scheme must be checked whether it is a transition state via frequency analysis, since a TS of first order has to have one imaginary mode that vibrates along the reaction path. Otherwise there is no transition state.

1.9 Software and Computational Details

The majority of computations in this work were carried out using the Vienna *ab initio* simulation package (VASP version 4 and 5.2) [38–42], which makes use of a plane wave basis. With VASP we did stationary, periodic DFT calculations and AIMD for a slab model.

For all the VASP calculations with the (0001) surface the parameters from prior work [22, 76–78] were used. Total energy convergence was achieved when energies between two SCF steps were smaller than 10^{-5} eV, structures were assumed minima if the change in forces between two structures was below 0.01 eV/Å and if all frequencies are real. The energy cutoff was set to 400 eV. A vacuum gap of 26.4 Å was used.

These convergence parameters were also adopted for the (11 $\bar{2}$ 0) surface. Here, the vacuum gap ranged from 17 Å for the 10 layer slab to 11 Å for the 25 layer slab, depending on the slab size in z-direction. (For the different slab models used for (11 $\bar{2}$ 0), see Section 3).

DFT (PBE and B3LYP) calculations were also done with the program CRYSTAL [43] (version 14), using a real-space representation. The same program was used for periodic HF

1 Methodology

calculations. Further, we performed LMP2 calculations with CRYSCOR [48]. Both use atom centered bases instead of plane waves. In all cases, no 3D slabs were calculated but 2D supercells were considered, treating only x and y directions periodically. Both programs were not applied in our group before so no convergence test had been done so far. The geometries and cell parameters from the VASP (PBE+D2) output were used as starting points and the usual convergence criteria of the programs were applied, convergence for SCF was achieved when energies between two steps were smaller than 2.7×10^{-6} eV (with some exceptions when convergence was hard to achieve).

2 Water on α -Al₂O₃(0001)

As mentioned earlier, the (0001) surface is the most stable surface site of alumina under UHV conditions, and it was subject of several studies so far [14, 21, 79–91]. Both experimental and theoretical studies discovered characteristics and specialties of this crystal cut. Experimentally, a whole zoo of methods was applied to study the (0001) surface, among which IR [83], LEED [84] and TEM [85] studies contributed to characterize the structure of the clean surface and of the latter in contact with water. Laser-induced thermal desorption spectroscopy [14, 86] showed that H₂O adsorbs dissociatively on the surface with a variety of hydroxyl surface sites with different binding energies. Theoretical studies were conducted by means of periodic *ab initio* calculations by Kurita [21] who studied the stability of distinct surface cuts without water. Also the system in contact with H₂O was studied by Hass and coworkers [79, 80] with *ab initio* molecular dynamics and they found that dissociation of molecular water is favored. Several studies found, that water adsorption is preferred at aluminum sites of the Al-terminated surface [80, 87], but dissociation is energetically more stable than molecular adsorption. Dissociation creates two distinct OH groups, the so-called OH_{ads} (adsorbed OH fragment) and OH_{surf} (OH from surface O and dissociated H atom) [87, 88]. Further, vibrational frequencies were calculated and compared to experiment [22, 91], and also reaction rates for the dissociation were evaluated [76, 91]. Also cluster studies were conducted approving the findings with periodic models [89, 90].

In our workgroup previous work concerned the adsorption, reactions and vibrational spectroscopy of water on α -Al₂O₃(0001) in the low-coverage limit. Furthermore, higher water coverages and hydroxylated surface systems were studied [22, 60, 76, 77].

In these studies, periodic DFT in the generalized gradient approximation was used. It is known (from other systems) that this may lead to errors in computed vibrational frequencies and, notably, in reaction barriers - the latter being typically too low with DFT-GGA. Further, in none of the studies on Al₂O₃(0001) the water dosing of the surface with a molecular beam, as used by our experimental partners at the Fritz-Haber Institute, was studied. In this work, the focus is therefore on two topics:

(i) The testing of methods beyond DFT with GGA functionals (as PBE) for adsorption ener-

gies, vibrational frequencies and activation energies for reactions.

(ii) Understanding the scattering processes of a water being shot at the surface with a molecular beam source with the help of AIMD.

First, the surface and the most stable adsorption patterns are introduced (Section 2.1), followed by the testing of methods beyond DFT-GGA (Section 2.2), and the results for the molecular beam scattering [92] (Section 2.3).

2.1 Supercell Model for the Adsorption of Water

In vacuum, the most stable surface cut of $\alpha\text{-Al}_2\text{O}_3(0001)$ is a stoichiometric, Al-terminated one. In this topmost Al layer, the aluminum atoms are undercoordinated and are referred to as coordinatively unsaturated site (CUS). Also, all oxygen atoms are threefold coordinated. We apply here a (2×2) supercell for the Al-terminated (0001) surface with cell vectors that were optimized from the bulk structure (adopted from previous work of Dr. J. Wirth [76]). The surface slab used in this work consists of nine atomic layers that equal three repeating units perpendicular to the surface of the type Al-O₃-Al-Al-O₃-Al-Al-O₃-Al (for the unit cell), with the top five layers being allowed to relax during optimization and AIMD and the lowest four layers being fixed to bulk values, see Figure 2.1.

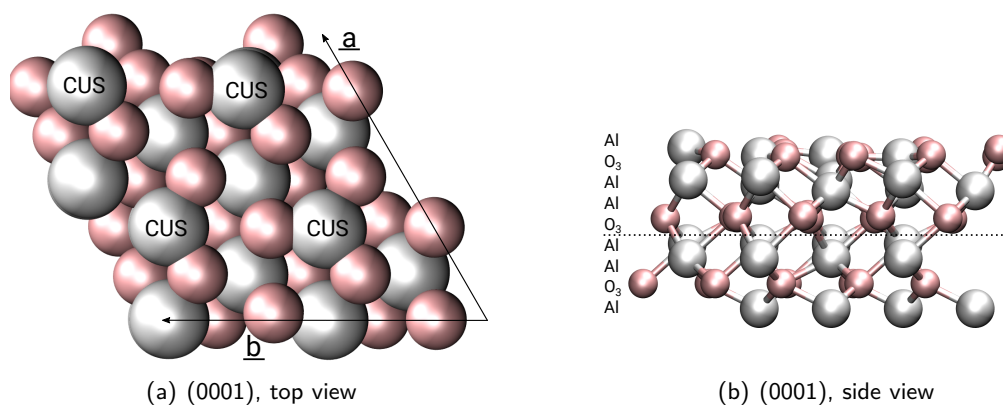


Figure 2.1: Surface model of the (0001), the most stable surface cut under UHV conditions. The top view (a) shows four Al CUS atoms (gray) for the (2×2) cell, which are surrounded by three threefold coordinated surface oxygen atoms (pale red). (b) reveals the side view of the Al-terminated surface cut in detail with the atomic layers indicated. Atoms below the dashed line are kept fixed to bulk values.

2.1 Supercell Model for the Adsorption of Water

The unit cell vectors are equal to $|\underline{a}| = |\underline{b}| = 9.66 \text{ \AA}$ and there is a 60° angle between them. The \underline{c} -vector of the slab model is perpendicular to the plane spanned by \underline{a} and \underline{b} and is 31.4 \AA long, hence the vacuum gap between two slabs in this direction is 26.4 \AA .

The adsorption behavior, vibrations and reactivity of one water molecule per (2×2) supercell (coverage $1/4$) were already studied in Reference [76]. As mentioned there, there is one molecular minimum on top of a CUS atom and three most stable, dissociated states (see Figure 2.2): the next neighboring 1-2 dissociated state, the 1-4 dissociated structure with the hydrogen atom being one position farther away and the 1-4' that is an example for a species with even greater distance from the OH group. Of these, according to periodic DFT calculations

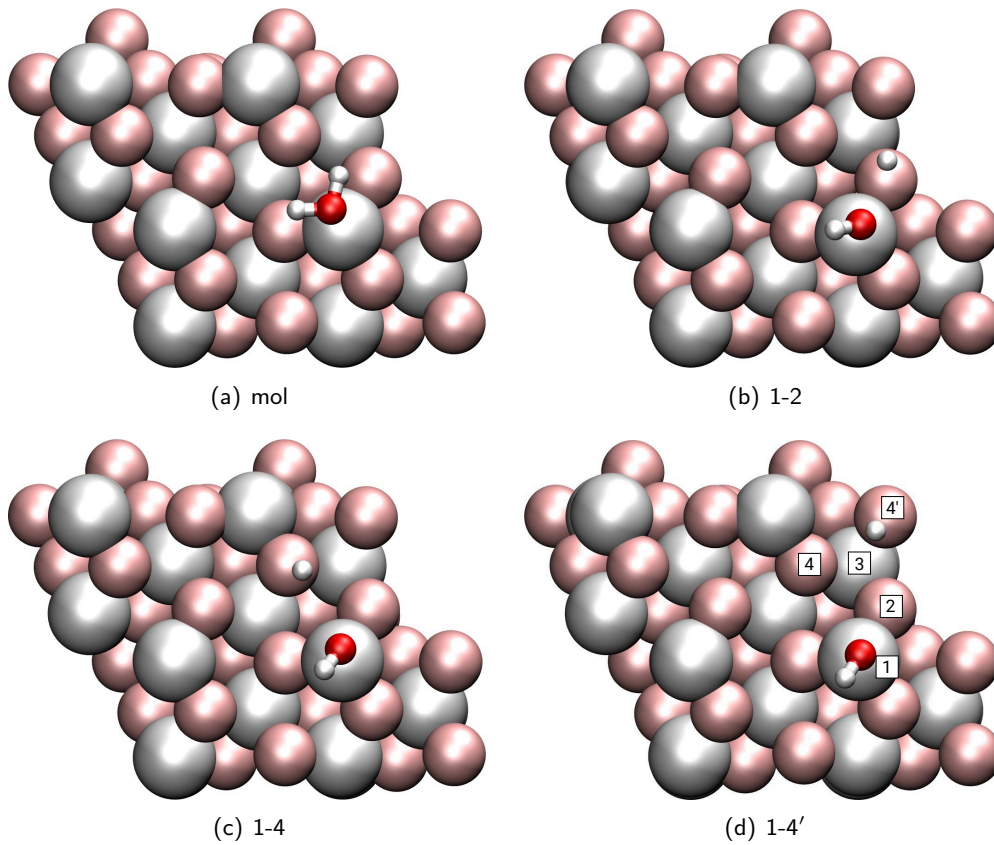


Figure 2.2: Adsorption geometries for the plane wave PBE+D2 optimized geometries of the molecular and the three dissociated species. Additionally, panel (d) shows the numbering of the surface atoms that provides the nomenclature. Adsorption energies are given in Table 2.1. The adsorption energy of 1-4' is not listed there and is $E_{\text{ads}} = 1.21 \text{ eV}$ for PBE+D2. These figures are from unpublished work of Dr. J. Wirth.

of Reference [76] using a plane wave basis and the PW91 exchange-correlation functional, the

1-2 dissociated species is the most stable one and the 1-4' is the least stable one, see Table 2.1 below.

The adsorption energy is defined as follows:

$$E_{\text{ads}} = E_{\text{ads. species}} - (E_{\text{free water molecule}} + E_{\text{surface}}). \quad (2.1)$$

For the stability of the molecular and the 1-4 dissociated species, the situation is more controversial in the literature [76, 80, 87]. In Reference [76] PW91 with dispersion corrections gives almost the same adsorption energy for both species.

We shall see below (Section 2.2) that the relative stability of the molecular and the various dissociated species, depends somewhat on the functional, on the treatment (or lack) of dispersion, on the basis (plane wave vs. atomic orbital basis), and on the level of electronic structure method (DFT vs. WFT). Further, the influence of these methods/basis sets on vibrational frequencies will be studied in Section 2.2.2.

In Reference [76], also reactions linking these minima were studied: dissociation of adsorbed water, OH- and H-diffusion on the surface, as well as rotation of an OH group and molecular water diffusion from one CUS site to another CUS site. To study the influence of the method/basis set on reaction barriers and rates (the latter obtained by Eyring's transition state theory in Section 2.2.3), we will exemplarily refer to the hydrogen diffusion from the 1-4 to the 1-2 adsorbed water (called Df-H-4-2 in [76] and here). The corresponding reaction path (obtained from a NEB calculation in [76]) is shown in Figure 2.3 below.

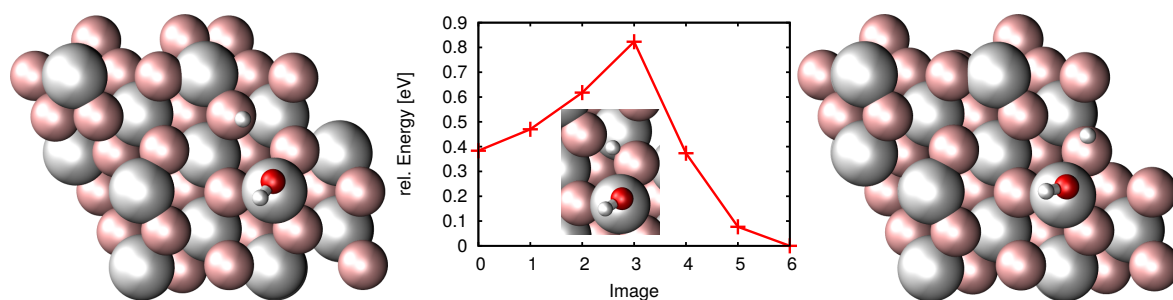


Figure 2.3: Reaction path of the Df-H-4-2 proton diffusion reaction obtained on the PBE+D2 level of theory via a NEB calculation (middle panel, the inset there shows the transition state), the left panel shows the educt (the 1-4 dissociated species), and on the right the product species (1-2). *Unpublished data by Jonas Wirth, with friendly permission.*

2.2 Adsorption Energies, Vibrations and Reactions of Water on α -Al₂O₃(0001) with and beyond DFT-GGA

As stated in the introduction, GGA functionals deliver poor barrier heights and reaction rates. In order to improve reaction rates with a high-level method, we chose the hydrogen diffusion reaction DF-H-4-2 as indicated in Figure 2.3. There, the transition state was calculated with PBE+D2 with the implementation of nudged elastic band in VASP using a plane wave basis. Rates were calculated via Eyring transition state theory (Equation (1.65)).

It is now our goal to test the accuracy of gradient-corrected DFT using, plane wave bases, against alternative methods/approaches. Specifically, the following will be done:

- (1) Using VASP, we will first compare various flavors of plane wave, three-dimensional supercell DFT-GGA: PBE+D2, PBE+D3, PW91 and PW91+D2.
- (2) We will then, using atom centered orbital basis (AO), test the performance of PBE+D3. This will be done with the CRYSTAL code, using a two-dimensional slab model. This allows us to test not only basis set effects, but also effects due to the choice of slab vs. supercell models.
- (3) Using CRYSTAL, 2D slab models and AO bases, we will test a hybrid DFT functional common in molecular chemistry, B3LYP (with dispersion corrections, D3).
- (4) Finally, we will also test pure wave function methods within 2D-slab/AO models, namely the Hartree-Fock (using CRYSTAL) and local Møller-Plesset perturbation theory of second order, LMP2 (using CRYSCOR).

We will apply these methods not only for barriers and kinetics, but also for adsorption energies and vibrational frequency analyses.

2.2.1 Adsorption Energies

2.2.1.1 GGA-DFT Calculations using PW Bases

For the GGA-DFT calculations using PW bases and VASP, a k -point mesh of $(3 \times 3 \times 1)$, an energy cutoff of 400 eV and a convergence criterion of 10^{-5} eV was adopted. In all cases, geometry optimizations for reactants and products were performed with the respective method.

In Table 2.1 the adsorption energy of VASP calculations with different functionals (PBE and PW91) with and without dispersion corrections are shown. The adsorption energy is calculated according to Equation (2.1).

Table 2.1: Adsorption energies E_{ads} (in eV) of the molecular and two dissociated adsorption states of H_2O on the alumina(0001) surface, obtained with VASP using a supercell approach and a plane wave basis.

method	mol	1-2 diss	1-4 diss
PW91 ^a	-1.25	-1.59	-1.25
PW91+D2 ^a	-1.40	-1.81	-1.45
PBE+D2 ^b	-1.31	-1.69	-1.21
PBE+D3	-1.29	-1.63	-1.30

^a J. Wirth, Reference [76,93]^b J. Wirth, unpublished

The adsorption energy is in favor of the 1-2 dissociated species for all methods. The next stable species is either the molecular adsorbate or 1-4, depending on the dispersion corrections used, or not, and on functional. The molecular and 1-4 dissociated species are equally stable (PW91, PBE+D3), or the latter is slightly more stable (PW91+D2), or less stable (PBE+D2). With dispersion corrections for PW91, all adsorbates get stabilized, but the molecular species is less stabilized than the dissociated adsorbates. In the case of PBE with dispersion corrections, we see that D2 and D3 do not change the results strongly, and also both stabilization (1-4 is stabilized with D3) and destabilization (mol and 1-2) occur.

2.2.1.2 GGA-DFT Calculations using AO Bases

We now compare for a particular GGA functional, PBE+D3, the performance of AO bases (and a two-dimensional slab model), to the plane wave results just mentioned. Calculations are done with the CRYSTAL code. We use a $(4 \times 4 \times 1)$ k -point grid and a convergence criterion for the total energy is 2.7×10^{-6} eV. When employing the CRYSTAL program, we first have to choose suitable basis sets. The basis sets which were tested are summarized in Table 2.2. The basis sets are numbered with increasing size, so that the largest number corresponds to the highest number of basis functions.

Again, in each case, the geometries of H_2O , the clean surface and the three adsorbed species (mol, 1-2 and 1-4) were optimized. The corresponding adsorption energies for PBE+D3 can be found in Table 2.3.

All basis sets that were tested predict with PBE+D3 the stability order $1-2 > \text{mol} > 1-4$. In contrast the VASP PBE+D3 plane wave calculation predicts an almost equal energy for mol and 1-4 diss. Most of the absolute values of the adsorption energies are too large when compared to the PBE+D3 values for the plane wave basis, by up to ~ 0.6 eV. We attribute

2.2 Adsorption Energies, Vibrations and Reactions of Water on α -Al₂O₃(0001)

Table 2.2: Applied basis sets for Al, O and H in the CRYSTAL calculations. The ordering is according to their size. Citations can be found in the table footnotes. The basis set names are adopted from the CRYSTAL basis set database. Basis sets 8 and 9 are developed further from basis sets in the CRYSTAL basis set data base. Further details can be found in Appendix A.

basis set	Al	O	H
1	Al_85-11G*_catti_1994	O_m-6-311G(d)_Heyd_2005	H_pob_TZVP_2012
2	Al_86-21G*_harrison_1993	O_m-6-311G(d)_Heyd_2005	H_pob_TZVP_2012
3	Al_85-11G*_catti_1994	O_pob_TZVP_2012	H_pob_TZVP_2012
4	Al_86-21G*_harrison_1993	O_pob_TZVP_2012	H_pob_TZVP_2012
5	Al_s8511p511d11_Heifets_2013	O_8411(d11)_Heifets_2013	H_pob_TZVP_2012
6	Al_m-6-311G(d)_Heyd_2005	O_m-6-311G(d)_Heyd_2005	H_pob_TZVP_2012
7	Al_pob_TZVP_2012	O_pob_TZVP_2012	H_pob_TZVP_2012
8	customized, high angular momentum basis		
9	basis set 8 with dual basis set expansion, adding further diffuse functions		

Heifets: [94], pob_TZVP: [95], Heyd: [96,97], Catti: [98], Harrison: [99,100]

Table 2.3: Adsorption energies E_{ads} (in eV) from Equation (2.1) for the three considered adsorption states of water on alumina(0001) surface (PBE+D3, geometry optimizations were evaluated with the respective basis set from Table 2.2).

basis set	mol	1-2 diss	1-4 diss
1	-1.87	-2.11	-1.75
2	-1.74	-1.96	-1.58
3	-1.53	-1.78	-1.43
4	-1.48	-1.73	-1.40
5	-1.57	-1.77	-1.38
6	-1.72	-1.96	-1.59
7	-1.47	-1.69	-1.35
8	-1.41	-1.68	-1.32

these larger values to some extent to basis set superposition errors (BSSE) which occur in AO-based calculations but not when using plane wave bases. In fact, as shown in Appendix B, for the case of basis 4, where the BSSE was evaluated, about 10% of the adsorption energy is due to BSSE for this basis. To overcome this problem, the larger “customized” basis set 8 was introduced for which the BSSE is expected to be smaller. In fact, the PBE+D3/AO absolute adsorption energies shown in Table 2.3 agree with PBE+D3/plane wave to within 0.02 eV (for 1-4 diss) to 0.12 eV (for mol). Deviations in the order of 0.1 eV are easily expected also due to the (other) computational settings (*e.g.*, 2D slab vs. 3D supercell models).

More important than absolute energies are energy differences between adsorbed species. Here most AO bases agree with energy differences obtained with PBE+D3/PW within ~ 0.1 - 0.2 eV. For basis set 8, for example, the energy difference between mol and 1-2 diss is -0.27 eV while the PW calculation gives -0.34 eV, and the energy difference between mol and 1-4 diss is $+0.09$ eV compared to -0.01 eV.

Going beyond pure density functionals and also beyond DFT has been too costly for a long time, and it is simply not applicable for a surface adsorbate system as large and electron rich as ours. However, in the CRYSTAL14 [43] and CRYSCOR [48] codes atom centered bases are used instead of plane waves so that large scale systems can also be computed. With this methodology it is possible to calculate periodic structures with GGA as well as with hybrid functionals and, moreover, with wave function-based techniques like LMP2.

2.2.1.3 Hybrid-DFT Calculations using AO Bases

Going beyond PBE (GGA functional), the hybrid functional B3LYP including D3 dispersion corrections was applied. Geometry optimizations were performed and adsorption energies were examined, see Table 2.4.

Table 2.4: Adsorption energies E_{ads} (in eV) from Equation (2.1) for the three considered adsorption states of water on alumina(0001) surface (B3LYP+D3, AO basis, geometry optimizations were evaluated with the respective basis set from Table 2.2). The basis sets 4, 7 and 8, which are highlighted are used for further calculations.

basis set	mol	1-2 diss	1-4 diss
1	-1.90	-2.25	-1.83
2	-1.80	-2.14	-1.69
3	-1.62	-2.01	-1.62
4	-1.57	-1.95	-1.57
5	-1.56	-1.88	-1.45
6	-1.78	-2.15	-1.68
7	-1.57	-1.92	-1.53
8	-1.43	-1.81	-1.40

Most basis sets also give the same ordering as PBE+D3, but basis 3 and 4 qualitatively give the same trends as VASP (adsorption energy for mol and 1-4 diss equal, like PW91 and PBE+D3) and also basis set 7 is very close to this. Henceforth, basis sets 4, 7 and 8 are used in further calculations; for the more computationally demanding transition state optimization the smaller basis 4 is used, for normal mode analyses, basis set 7 is used and basis 8 for adsorption energies.

2.2.1.4 Wave Function Theory with AO Basis

Table 2.5: Adsorption energies for basis set 8 (in one case 9) for the method given in the first column. All values are given in eV. The HF and LMP2 calculations use single point calculations on top of B3LYP+D3 optimized geometries with basis set 8. The dual basis LMP2 calculation applies the expanded basis 9, in which further functions are added to basis set 8.

	mol	1-2 diss	1-4 diss
PBE+D3	-1.41	-1.68	-1.32
B3LYP+D3	-1.43	-1.81	-1.40
HF	-1.14	-1.67	-1.19
LMP2 (basis 8)	-1.34	-1.69	-1.26
LMP2 (basis 9)	-1.31	-1.61	-1.18

To go beyond density functional theory, first Hartree-Fock and on top of it LMP2 calculations were applied, using basis set 8. The HF and LMP2 calculations were carried out as single point calculations using the optimized geometries from B3LYP+D3/AO basis 8. The resulting adsorption energies can be found in Table 2.5.

For the calculation of LMP2 the HF calculations have to be converged with a large basis set 8. Then the HF orbitals from this calculation are localized and in an optional step, additional basis functions (basis set 9) can be added by the dual basis set expansion [49], so that a basis set of the size of approximately augmented triple zeta can be achieved. This expansion was adopted for Al and O, see Appendix A. For this dual basis set expansion, one step of a HF calculation was executed. With these orbitals, LMP2 is then calculated.

All methods in Table 2.5 suggest, that the 1-2 is the most stable species. In contrast to all other methods, HF predicts the 1-4 dissociated species to be more stable, so that there might be correlation effects relevant. These two LMP2 results for basis set 8 (without dual basis set expansion) and 9 (including the dual basis set expansion) are compared in Table 2.5. One can see that there is indeed a difference in stability with and without the dual basis set. Especially the 1-2 diss gets stabilized without additional basis functions but also the 1-4 dissociated structure gains stability, compared to the molecular minimum that is predicted to be almost equal by both methods. The adsorption energies for the LMP2 calculation without the dual basis set expansion are more negative, which means increased stability. This could be due to different (de)stabilization of the adsorbed system, the clean surface and water, that contribute to the adsorption energy (Equation (2.1)).

The results of HF and LMP2 (both with and without dual basis set expansion) are also compared to DFT results with PBE+D3/AO and B3LYP+D3/AO in Table 2.5. Here the

overall trend for DFT that mol is more stable than 1-4 diss is confirmed by the dual basis set expanded LMP2 calculation (basis 9), but without this expansion (basis 8), LMP2 gives both geometries an almost degenerate energy. In summary, DFT and LMP2 agree qualitatively and also quantitatively within 0.1-0.2 eV which is within the tolerance of the methods.

The geometries of VASP/PBE+D2/PW and CRYSTAL/PBE+D3/B3LYP+D3/AO calculations do not differ strongly. Differences are shown exemplarily for basis set 8. In principle it can be seen from the data in Table 2.6, that both bond lengths and angles with respect to the surface normal are slightly higher with PBE+D3/PW from VASP than with PBE+D3/AO and B3LYP+D3/AO from CRYSTAL, although angles do not differ much. B3LYP+D3/AO

Table 2.6: Comparison of geometric properties OH bond lengths (BL/Å) and OH angles (θ /°) with respect to the surface normal (compare Table 3.7). For the dissociated species, the first number gives the value for the adsorbed group and the second for the surface OH group. The first block gives results for VASP/PBE+D3/PW, the second for CRYSTAL/PBE+D3/AO and the last one for CRYSTAL/B3LYP+D3/AO, both with the basis set 8.

		mol	1-2 diss	1-4 diss
PBE+D3/PW	BL	0.98, 0.99	0.97, 0.98	0.97, 0.98
	θ	87.94, 99.07	51.70, 34.94	51.21, 27.17
PBE+D3/AO	BL	0.98, 0.98	0.96, 0.98	0.96, 0.98
	θ	87.383, 97.86	51.96, 34.21	52.40, 26.54
B3LYP+D3/AO	BL	0.97, 0.97	0.95, 0.97	0.96, 0.97
	θ	85.04, 95.84	49.81, 33.03	49.94, 26.74

gives the shortest bond lengths and the smallest angles in the comparison but still the results are in very good agreement.

2.2.2 Frequency Analysis: Normal Modes and Beyond

Apart from calculating adsorption energies, also normal modes with CRYSTAL were calculated with the functional B3LYP+D3 and PBE+D3, both with basis set 7 from Table 2.2. To compare with experimentally suggested values [22], which presented OD-vibrational frequencies, we replaced O-H for the normal mode analysis, by O-D. Additionally, anharmonic corrections for both O-D bonds (OD_1 and OD_2 for molecular or for dissociated water OD_{surf} and OD_{ads} for the group with D from water and a surface O atom and from the adsorbed OD species, respectively) for the three stable minima (molecular adsorbed, 1-2 and 1-4 dissociated water) have been performed. For these, the O-D distances around the equilibrium position are varied from -0.2 to $+0.3$ Å. A potential energy is calculated for each value of O-D distance, at seven points

in total. To these points a polynomial curve of 6th degree was fitted. A corresponding nuclear Schrödinger equation was solved numerically and the anharmonic wavenumber calculated as $\tilde{\nu}_{\text{anh}} = \frac{1}{hc}(E_1 - E_0)$, where E_1 and E_0 are vibrational energies of the lowest two vibrational states.

In Table 2.7 the results for PBE+D3 and B3LYP+D3 for the (0001) surface are summarized. In comparison with former PBE+D2/plane wave calculations, the PBE+D3 results with AO

Table 2.7: Harmonic and anharmonic wavenumbers for OD stretch vibrations of $\text{D}_2\text{O}/\text{Al}_2\text{O}_3(0001)$, calculated at the PBE and B3LYP level of theory with D3 corrections with the AO basis set 7 (first two blocks), compared to harmonic PBE+D2/PW values third block (calculations done by J. Wirth [93]) and experimental SFG data from Reference [22].

stretch	PBE+D3/AO		B3LYP+D3/AO		PBE+D2/PW	Exp. [22]
	$\tilde{\nu}$ [cm^{-1}]	$\tilde{\nu}_{\text{anh}}$ [cm^{-1}]	$\tilde{\nu}$ [cm^{-1}]	$\tilde{\nu}_{\text{anh}}$ [cm^{-1}]	$\tilde{\nu}$ [cm^{-1}]	$\tilde{\nu}$ [cm^{-1}]
mol: OD ₁	2657	2562	2747	2650	2664	-
mol: OD ₂	2539	2490	2627	2584	2550	-
1-2: OD _{surf}	2596	2521	2697	2623	2629	2729
1-2: OD _{ads}	2808	2727	2883	2805	2810	2910
1-4: OD _{surf}	2621	2531	2715	2631	2647	2764
1-4: OD _{ads}	2795	<i>not converged</i>	2873	2788	2795	2900

basis do not deviate much. In contrast to that, B3LYP+D3 results with AO are systematically higher in energy. For both functionals anharmonic corrections decrease the wavenumbers of the OD vibrations, such that the B3LYP+D3+anharmonic corrections are again at the same level as uncorrected PBE+D3 with CRYSTAL and the PW PBE+D2 results with VASP. In comparison with experimental SFG spectra [22], the vibrations could be assigned to respective OD vibrations of different (dissociatively) adsorbed species. The suggested OD vibrational wavenumbers in the SFG experiments [22] are: 2729 (1-2: OD_{surf}), 2764 (1-4: OD_{surf}), 2790 (1-4': OD_{surf}, was not considered here), 2900 (1-4: OD_{ads}, 1-4': OD_{ads}) and 2910 cm^{-1} (1-2: OD_{ads}). Hence, the absolute agreement with plane wave PBE+D2 results was not very good (see Table 2.7)¹. However, differences between the peaks with respect to the highest energy peak (OD_{ads} of 1-2 diss) were in very good agreement, see Table 2.8. Applying the same for the AO basis calculations, even better results can be reached with B3LYP+D3.

¹ In Reference [101], average scaling factors for B3LYP = 1.004 and for PBE = 1.034 are reported. If one multiplies $\tilde{\nu}(\text{harm.})$ with those factors, we approach the experiment by $\approx 15 - 30 \text{ cm}^{-1}$ (B3LYP), and $\approx 15 - 50 \text{ cm}^{-1}$ (PBE), respectively.

Table 2.8: Vibrational frequency differences of the results presented in Table 2.7 with respect to the highest energy mode, OD_{ads} of 1-2 diss. All wavenumbers $\tilde{\nu}$ are given in cm⁻¹.

resonances	PBE+D3/AO		B3LYP+D3/AO		PBE+D2/PW	Exp. [22]
	$\Delta\tilde{\nu}$	$\Delta\tilde{\nu}_{\text{anh}}$	$\Delta\tilde{\nu}$	$\Delta\tilde{\nu}_{\text{anh}}$	$\Delta\tilde{\nu}$	$\Delta\tilde{\nu}$
1-2: OD _{ads} -1-2: OD _{surf}	212	206	186	182	181	191
1-2: OD _{ads} -1-4: OD _{surf}	187	196	168	174	163	146
1-2: OD _{ads} -1-4: OD _{ads}	13	-61	10	17	15	10

2.2.3 Activation Energies and Reaction Rates

For the reaction Df-H-4-2 introduced earlier and shown in Figure 2.3, a transition state was recalculated with B3LYP+D3 and AO basis set 4 [102, 103]. Additionally from this optimized transition state, single point calculations were performed with larger basis sets 7 and 8 (B3LYP), with basis 8 for HF and also with LMP2 (basis 9) to correct ΔE^\ddagger , while vibrational contributions to ΔG^\ddagger were taken from the respective normal mode analysis. For HF and LMP2 no normal modes could be calculated, so instead the vibrational contributions of B3LYP+D3/AO basis 8 were employed. The respective educt optimizations and frequency analyses were done with the respective basis set (for LMP2 the B3LYP+D3/AO-8 optimized geometry was used). Activation energies, free energies and corresponding rates at 300 K were calculated with Equation (1.65) to check the accuracy of GGA, see Table 2.9. For comparison, plane wave VASP results with PW91 and PBE+D2 are also given in the Table.

Table 2.9: ΔE^\ddagger , ΔG^\ddagger (300 K) in eV and k (300K) in s⁻¹ for the reaction Df-H-4-2 with B3LYP+D3 obtained with CRYSTAL for different basis sets (4, 7, 8 for B3LYP+D3, 8 for HF and 9 for LMP2). HF and LMP2 results for ΔG^\ddagger and k are estimated by the difference of ΔE^\ddagger and ΔG^\ddagger from the B3LYP+D3 with basis 8, the corresponding rate inherits the same approximation. VASP results are given for PW91 and PBE+D2 using a plane wave basis.

basis	B3LYP+D3 AO-4	B3LYP+D3 AO-7	B3LYP+D3 AO-8	HF* AO-8	LMP2* AO-9	PW91 PW	PBE+D2 PW
ΔE^\ddagger	0.65	0.65	0.69	1.17	0.60	0.42	0.44
ΔG^\ddagger	0.53	0.54	0.58	1.06	0.49	0.27	0.29
k (300K)	8.0×10^3	5.8×10^3	1.2×10^3	1.0×10^{-5}	3.7×10^4	2.0×10^8	9.1×10^7

* The contribution of the vibrations is estimated from B3LYP+D3 with basis set 8, the corresponding rate is also affected by this approximation.

The plane wave based barrier with PBE+D2 is $\Delta G^\ddagger = 0.29$ eV, resulting in a rate at 300 K of 9.1×10^7 s⁻¹. Similar results are obtained for PW91/PW. For all the atom centered calculations with CRYSTAL/AO basis, the (free) energy barriers are higher by 0.24-0.29 eV for B3LYP+D3

(AO bases 4, 7 and 8) and 0.2 eV for LMP2 (AO basis 9) and the respective rate constants are smaller. The result for HF, however, seems to be an outlier with a very high barrier leading to a small reaction rate constant, which could be explained by the lack of correlation. With the hybrid functional B3LYP+D3/AO, we get (free energy) barriers of $\Delta G^\ddagger \sim 0.53\text{-}0.58\text{ eV}$ and rates in the order of 10^3s^{-1} , and with LMP2 barriers are slightly lower (0.49 eV), giving higher rates (10^4s^{-1}) whereas the rate constant with PBE+D2/PW basis is in the order of 10^7s^{-1} and the PW91 rate (without dispersion corrections) is even higher ($9.1 \times 10^7\text{s}^{-1}$). This shows the potential of B3LYP and/or LMP2 methods towards the improvement of reaction rates and barriers of surface reactions.

2.3 AIMD Simulation of Molecular Beam Scattering Experiments [92]

Water that is probed at the $\alpha\text{-Al}_2\text{O}_3(0001)$ surface via a molecular beam experiment can adsorb molecularly and dissociatively. In comparison to pinhole dosing scientists could find an enhanced dissociation probability [92]. The mechanism behind this increased dissociation is unknown and shall be revealed in the current section. In these simulations heavy water (D_2O) collides with the $\alpha\text{-Al}_2\text{O}_3(0001)$ surface, to compare with experiments.

Previous studies by Hass *et al.* [79, 80] discussed the question whether water will adsorb molecularly and dissociate in a consecutive step or if it can dissociate directly. This study considered an adsorbed water molecule propagated rather than water being shot on the surface. On this basis, the results are not comparable to ours because the dynamical influence of the beam is what we are interested in.

To tackle this question, AIMD calculations were conducted for a water (D_2O) molecule or a water cluster approaching the surface, with different beam and surface models applied. In all cases VASP PBE+D2 plane wave calculations with a stoichiometric (2×2) supercell were applied with a ($3 \times 3 \times 1$) k -point grid. A plane wave energy cutoff of 400 eV was used and SCF energies were converged if the energy between two cycles was smaller than 10^{-5} eV. Dipole corrections perpendicular to the surface were applied. For the MD simulations, a time step of $\Delta t = 0.2\text{ fs}$ was used. As in the previous section, a slab with nine atomic layers was used with the lowest four layers fixed at bulk positions (compare Figure 2.1).

2.3.1 Beam Model

For the understanding of a molecular beam source experiment, the introduction of a beam is an essential part of the model. As a first order approach to a beam, a cold water (D_2O)

molecule (initial parameters are $d_{OD} = 0.97 \text{ \AA}$ and bond angle of 104.5°) was shot in agreement with the experiment perpendicularly to the surface. In the simulation this was done from a center of mass position with a distance of 4 \AA from the surface. Also higher distances were tested but no difference could be detected. Having internal degrees of freedom excluded, five are still left which can be seen in Figures 2.4, 2.5 and Table 2.10: two for the impact site $[a_0, b_0]$ given in units of the supercell vectors \underline{a} and \underline{b} , three Euler angles α , β and γ for the rotational orientation of the molecule with respect to the surface. An additional parameter is the kinetic energy E_{kin} that gives the molecule a momentum towards the surface, solely as translational motion, with no vibration or rotation included. These parameters were varied systematically to gain insight into the process. Six different impact points $[a_0, b_0]$ are considered, which are shown in Figure 2.5, eight rotational orientations (see Table 2.10) and kinetic energies were probed from 0.5 eV to 0.9 eV in steps of 0.1 eV .

As mentioned before and in Reference [76], the barriers for diffusion reactions on the surface can be high (and corresponding rates low), especially for the H-diffusion reactions. The adsorption process itself was found to be barrierless since upon impact the adsorption energy (in the order of 1.5 eV is released) and additionally the incoming water molecule holds kinetic energy. With this processes that are slow at room temperature otherwise, can be speeded up considerably under MBS conditions.

This basic beam model is later refined through improvements presented in Section 2.3.6, which addresses clustering as well as rotationally and vibrationally excited water.

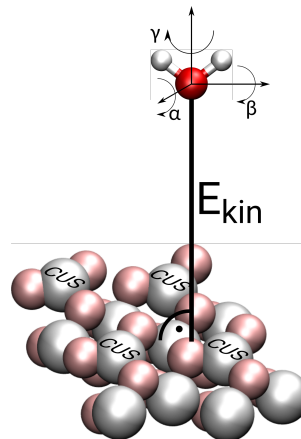


Figure 2.4: Initial parameters of the trajectories, for MB scattering of D_2O at $\text{Al}_2\text{O}_3(0001)$ considered in this work. Gray spheres Al, pale red O of alumina, red O and white H. The water molecule approaches the surface perpendicularly with its center of mass situated 4 \AA above the surface with a kinetic energy E_{kin} , at an impact site $[a_0, b_0]$ given by fractions of the \underline{a} and \underline{b} vectors of the (2×2) cell. The orientation is given by three Euler angles with respect to three perpendicular rotation axes, $[\alpha, \beta, \gamma]$.

2.3 AIMD Simulation of Molecular Beam Scattering Experiments

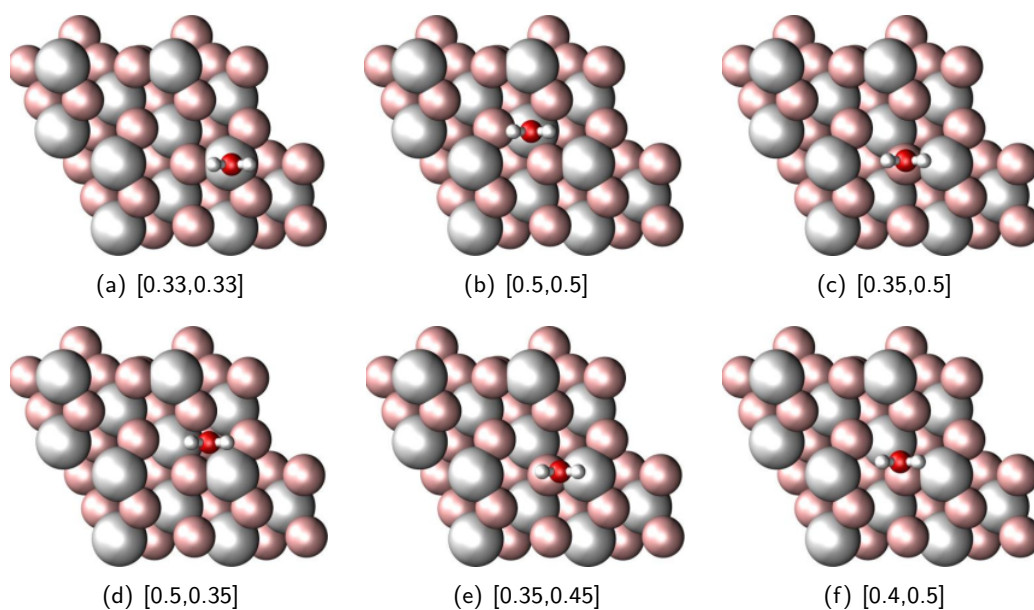
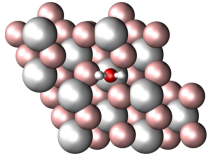
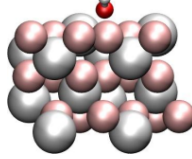
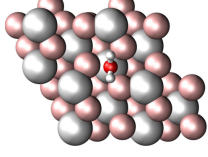
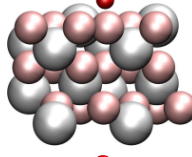
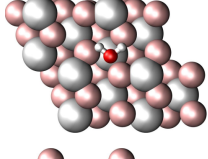
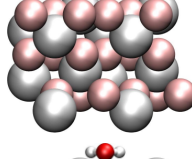
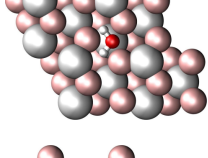
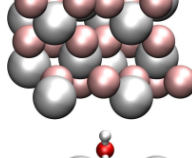
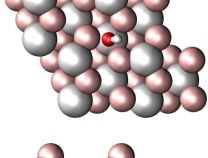
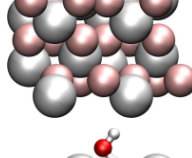
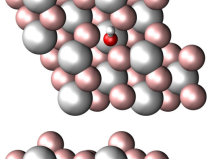
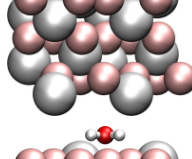
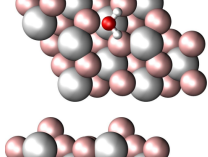
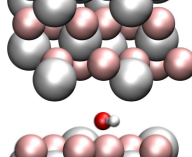
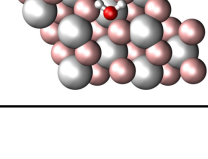
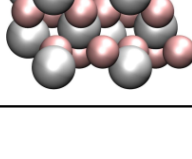


Figure 2.5: The six impact points $[a_0, b_0]$ which were used in the AIMD calculations (shown for the rotational orientation $[0, 0, 0]$, top view).

While many initial conditions were considered, it was not possible to compute a fully realistic beam, because this would require wide knowledge about energy and velocity distributions and a systematic high dimensional sampling. This is not feasible with the computational power available for this work.

Table 2.10: Orientations of the water molecule characterized by three Euler angles $[\alpha, \beta, \gamma]$, the latter given in $^\circ$. Shown are both top view and side view at impact point $[0.5, 0.5]$.

orientation $[\alpha, \beta, \gamma]$	top view	side view
$[0, 0, 0]$		
$[0, 0, 90]$		
$[0, 90, 0]$		
$[0, 90, 90]$		
$[90, 0, 0]$		
$[90, 0, 90]$		
$[90, 90, 0]$		
$[90, 90, 90]$		

2.3.2 Example Trajectories

Before going to the details, example trajectories for each process leading to one of the four most stable adsorbed species, molecular adsorption, 1-2 dissociation, 1-4 dissociation and 1-4' dissociation are shown in Figure 2.6. The applied parameters are reported in the respective caption. These figures were all obtained from canonical calculations (NVT) at 300 K (the trajectory shown in (d) was additionally preexcited in the asymmetric stretch mode leading to 1-4' dissociation). As one can see, molecular, 1-2 and 1-4 dissociated species can occur within sub-ps time scale at the surface; this process is henceforth called direct dissociation from the gas phase. Note that in the 1-2 and 1-4 dissociated species, the dissociated deuteron undergoes large-amplitude motion, while the hydroxyl OD vibration is hardly excited after dissociation. For the 1-4' dissociation shown in Figure 2.6(d), such direct process does not happen. Instead this species can be reached indirectly via a short-lived intermediate also within a sub-ps time scale. This is an example of a slow reaction (diffusion from 1-2 to 1-4' dissociated species with $\Delta G^\ddagger = 0.67$ eV [76]) being enormously accelerated under MBS-like conditions.

This indirect process, however, is not unique for the 1-4' dissociated species, all the other species including the molecular one can be observed to happen indirectly by either being reflected first from the surface before adsorbing/dissociating or by adsorbing molecularly before dissociating. However, the 1-4' species was the only one that could not be reached by direct dissociation.

2.3.3 Microcanonical AIMD at a Clean Surface at $T = 0$

The effects of a single D₂O shot to the cool surface with an NVE ensemble (microcanonical AIMD, the 0 K optimized geometry of the surface has no initial momenta) were studied systematically by probing over six parameters: Five different kinetic energies (from 0.5 to 0.9 eV in 0.1 eV steps), six lateral impact points at the surface ([0.33,0.33], [0.5,0.5], [0.35,0.5], [0.5,0.35], [0.35,0.45], [0.4,0.5], as introduced in Figure 2.5), and eight different orientations of the water molecule with respect to the surface ([0,0,0], [0,0,90], [0,90,0], [0,90,90], [90,0,0], [90,0,90], [90,90,0], [90,90,90], see also Table 2.10). These $5 \times 6 \times 8 = 240$ AIMD trajectories for the clean surface at $T = 0$ K were simulated for ca. 1.2 ps each.

In the trajectories either molecular adsorption, 1-2 dissociation or reflection could be observed. Dissociation was assumed if the OD distance was greater than 1.3 Å, but it was ensured that the results did not differ for a greater cutoff distance by looking at each individual trajectory. Interestingly, only 1-2 dissociation and no 1-4 dissociation could be observed for these conditions (NVE, clean surface), although the molecular and the 1-4 dissociated species are almost equal in energy, and also the barrier heights ΔE^\ddagger for the dissociation to 1-2 (0.13 eV)

2 Water on $\alpha\text{-Al}_2\text{O}_3(0001)$

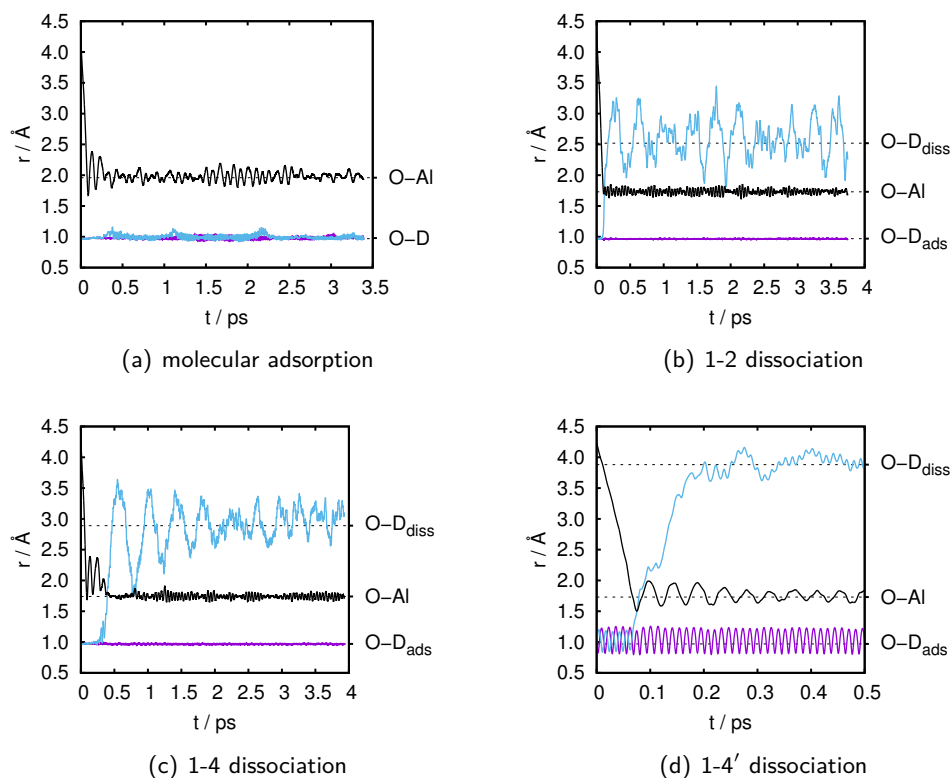


Figure 2.6: The four adsorbed states of water, as shown in Figures 2.2(a)-(d) are obtained in these exemplary trajectories. All of them are from canonical (NVT) trajectories at $T = 300\text{ K}$. The initial parameters: (a) $E_{\text{kin}} = 0.7\text{ eV}$, $[a_0, b_0] = [0.33, 0.33]$, $[\alpha, \beta, \gamma] = [0, 0, 90]$; (b) $E_{\text{kin}} = 0.7\text{ eV}$, $[a_0, b_0] = [0.35, 0.45]$, $[\alpha, \beta, \gamma] = [0, 0, 0]$; (c) $E_{\text{kin}} = 0.7\text{ eV}$, $[a_0, b_0] = [0.33, 0.33]$, $[\alpha, \beta, \gamma] = [0, 90, 0]$; (d) $E_{\text{kin}} = 0.7\text{ eV}$, $[a_0, b_0] = [0.35, 0.5]$, $[\alpha, \beta, \gamma] = [0, 0, 0]$. As specified in Subsection 2.3.6.2, for the latter the water molecule was vibrationally preexcited along the asymmetric stretch normal coordinate. The r values (y axis) correspond to bond length distances between water-O and the CUS Al atom on which either D_2O or the water hydroxyl unit OD adsorb (O-Al), the distance between water-O and D in non-dissociated (fragments of) D_2O (O-D or O-D_{ads}), and the distance between water-O and D in dissociated (fragments) of D_2O (O-D_{diss}), respectively. Also the interatomic distances of the minimum geometries are given as horizontal dashed lines. Panel (d) shows that the 1-4' state is not obtained directly but reached *via* a short-lived 1-2 dissociation intermediate.

and 1-4 (0.19 eV) do not differ largely [76]. As shown later, other conditions are necessary for reaching 1-4 dissociation.

As an example and also for later reference, we list in Table 2.11, the outcomes of all 48 trajectories for a particular kinetic energy, $E_{\text{kin}} = 0.7\text{ eV}$, which illustrates the points just made.

2.3 AIMD Simulation of Molecular Beam Scattering Experiments

In this case, molecular adsorption dominates, followed by 1-2 dissociation and reflection.

Table 2.11: Outcome of microcanonical (NVE, $T = 0$) trajectories with $E_{\text{kin}} = 0.7$ eV, after the end of propagation, for different combinations of initial impact points and rotational orientations. R=reflection, M=molecular adsorption, D(1-2)=1-2 dissociation.

orientation [α, β, γ]	impact position [a_0, b_0]					
	[0.33,0.33]	[0.5,0.5]	[0.35,0.5]	[0.5,0.35]	[0.35,0.45]	[0.4,0.5]
[0, 0, 0]	M	R	D(1-2)	M	D(1-2)	D(1-2)
[0, 0, 90]	M	R	M	M	M	M
[0, 90, 0]	M	R	M	M	D(1-2)	M
[0, 90, 90]	D(1-2)	R	M	M	D(1-2)	M
[90, 0, 0]	M	R	R	M	M	R
[90, 0, 90]	M	R	M	D(1-2)	D(1-2)	M
[90, 90, 0]	M	M	D(1-2)	M	D(1-2)	M
[90, 90, 90]	M	R	M	M	D(1-2)	M

Figure 2.7 is a statistical analysis of the data, where the probabilities for reflection, molecular adsorption and 1-2 dissociation are shown as a function of the kinetic energy (a), impact point (b) and the orientation (c). It was distinguished between direct and indirect dissociation. Admittedly, this analysis is restricted by the number of trajectories (240). From these figures and the data one can derive the following conclusions:

As anticipated, all three processes could be observed, reflection (20.4%, 49 of the 240 trajectories), molecular adsorption (55.4%, 133 trajectories) and 1-2 dissociation (24.2%, 58 trajectories). Probabilities for all outcomes can be found in Appendix C.

Looking at the influence of the kinetic energy in Figure 2.7(a), the results do not depend largely on the initial kinetic energy of the molecule, at least for the probed energy range. In all cases molecular adsorption dominates, followed by 1-2 dissociation and reflection, both of which are in the same range around 20-25%. This reflection probability P_{diss} is only increased for 0.9 eV, at the expense of the molecular species.

We chose the set of parameters ($[a_0, b_0] = [0.35, 0.45]$; $[\alpha, \beta, \gamma] = [0, 0, 0]$), for which $P_{\text{diss}} = 1$ for all energies ≥ 0.5 eV. To evaluate whether this will hold true for the low energy regime, one additional trajectory with the kinetic energy of 0.1 eV was calculated. In the case of $E_{\text{kin}} = 0.1$ eV, the trajectory only shows molecular adsorption. This result was rather surprising, since the kinetic energy plus the adsorption energy minus the barrier height is with $(0.1 + 1.31 - 0.13)$ eV=0.28 eV in the same order as the reaction barrier ($\Delta G^\ddagger = 0.29$ eV [76]). This allows to draw the conclusion that a minimum kinetic energy is necessary for the dissociation process. In the experimental studies of R. K. Campen [104], a kinetic energy of the beam between 0.6

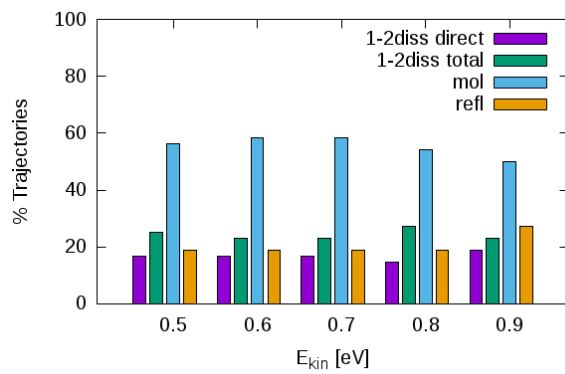
and 0.75 eV is used. This minimum energy constraint can be one possible explanation of the difference between MBS and pinhole dosing. In the latter case, the only energy of a water molecule comes from the thermal energy. For a D_2O molecule in the gas phase at 300 K this can be estimated to be around $\frac{3}{2}k_B T \approx 40$ meV.

In contrast to the kinetic energy, the lateral impact point at the surface has a great influence on adsorption and dissociation probabilities as can be seen in Figure 2.7(b). For the impact point [0.5,0.5], a non-surface Al position, 88% of the trajectories get reflected and molecular adsorption and 1-2 dissociation are oppressed, whereas for [0.33,0.33], directly on top of an Al CUS position, 83% adsorb molecularly which dominates clearly over 1-2 dissociation. In contrast to both sites, [0.35,0.45] which is located at a gap between the CUS position and a neighboring oxygen atom leads to a high dissociation probability of $P_{\text{diss}} \approx 68\%$ with a minor percentage of indirect dissociation. This high dissociation probability can be explained by the fact that the molecule hits the surface already in a “product-like” geometry, so that the OD bond breakage is facilitated.

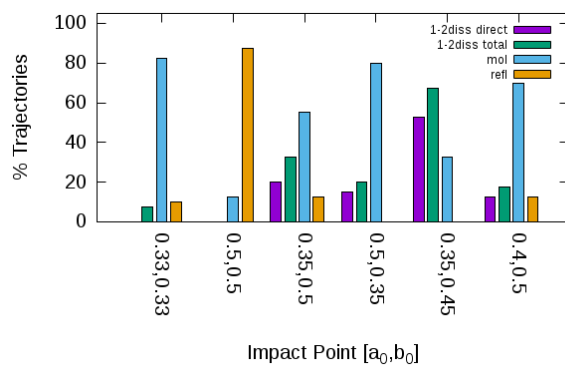
The initial rotational orientation also has an effect (*cf.* Figure 2.7(c)), although not as drastic as the impact point dependence. This might be explained when looking at the trajectories in detail, where one can see that the water molecule rotates due to the attractive and repulsive interaction with the surface atoms. This leads to a reorientation of the water molecule right before adsorbing, so that the initial orientation is not remembered reliably by the system. The orientation of the molecule shortly before reaching the surface is more important. As before, if the molecule’s orientation is already in a product-like state, the dissociation probability is elevated.

The data shows that direct dissociation dominates mostly over indirect dissociation, although it is dependent on the initial conditions, *e. g.* for the initial orientation [0,90,90] only indirect dissociation is observed.

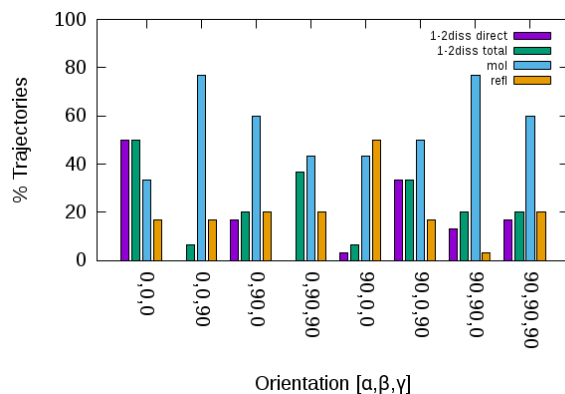
2.3 AIMD Simulation of Molecular Beam Scattering Experiments



(a) Energy



(b) Impact Point



(c) Orientation

Figure 2.7: Bar charts showing the statistics of NVE AIMD trajectories at 0 K for a single D_2O molecule approaching the clean alumina(0001) surface. (a) summarizes the findings for all kinetic energies E_{kin} averaged over $6 \times 8 = 48$ combinations of impact point and orientation. In (b), for all impact points $[a_0, b_0]$ is averaged over $5 \times 8 = 40$ combinations of kinetic energy and rotational orientation and (c) gives an overview over all rotational orientations $[\alpha, \beta, \gamma]$, averaged over $5 \times 6 = 30$ combinations of kinetic energy and impact points. The columns give percentages of the different outcomes - here labeled as direct and total 1-2 dissociation (“1-2 diss direct” in purple and “1-2 diss total” in green), “mol” molecular adsorption (blue) and “refl” reflection in yellow. If one type of outcome did not occur, no column is shown.

2.3.4 Thermalized Surface

The effects of a thermal surface were studied for single D₂O molecules approaching a clean α -Al₂O₃(0001) surface, using an initial kinetic energy of 0.7 eV with momentum perpendicular to the surface. First, we selected five initial parameter sets, which all led to (1-2) dissociation in the microcanonical (NVE, $T = 0$) case: $[a_0, b_0], [\alpha, \beta, \gamma] = [0.35, 0.45], [0, 0, 0]; [0.35, 0.45], [0, 90, 90]; [0.35, 0, 45], [90, 90, 90]; [0.4, 0.5], [0, 0, 0]; [0.5, 0.35], [90, 0, 90]$. For all of these sets, 100 NVT trajectories were run at a temperature of 300 K, following the protocol: (1) The naked surface was preequilibrated for 1 ps; (2) then the water was fired using an analogous setting as in Section 2.3.3 on the thermal surface now, and the AIMD trajectories were run for another 1-ps period. For testing longer propagation periods, see below. In practice in step (2), the thermostat acted also on water, however, since the molecule quickly hits the surface (400 steps, ~ 0.08 ps), this slight inconsistency hardly affects the dynamics.

As a result of this procedure, we found that *all* 500 trajectories (100 trajectories \times 5 parameter sets) led to 1-2 dissociation. No reflection, molecular adsorption and other modes of dissociation (1-4 or 1-4') were observed, at least on the time scale considered. The inefficiency of thermal surface motion was slightly surprising (and disappointing) to us, since the energy of a thermalized surface, $\sim N_s \times 3k_B T = 2.8$ eV (where $N_s = 36$ is the number of movable surface atoms), is comparable to the kinetic energy of the molecule when crashing into the surface (~ 2 eV). On the other hand, when only a single surface atom (*e.g.*, an impact site) is considered, the surface atom's energy is much smaller than that of the impinging molecule which may rationalize the observation.

Next, all $6 \times 8 = 48$ combinations of impact sites $[a_0, b_0]$ and rotational orientations $[\alpha, \beta, \gamma]$ as in Section 2.3.3 were (re-)considered, for a single initial translational energy of $E_{\text{kin}} = 0.7$ eV. Now, only two NVT AIMD calculations were run per initial condition, after the surface had been equilibrated at 300 K for 1 ps before. The restriction to two trajectories gives only a quite limited statistical significance but was dictated by restricted computational resources. We did allow for longer propagation times after the equilibration phase, though, propagating each trajectory for 4 ps now. For six of the 48 initial conditions, our NVT AIMD trajectories terminated due to numerical problems. For the remaining $42 \times 2 = 84$ AIMD trajectories, a "statistics" for various events, reflection, molecular and dissociative adsorption, was obtained as shown in Table 2.12, third line. These values are to be compared to the corresponding 42 microcanonical, $T = 0$ trajectories for $E_{\text{kin}} = 0.7$ eV, given in the second row of Table 2.12. For reference, the corresponding values for $E_{\text{kin}} = 0.7$ eV averaged over all 48 initial conditions

2.3 AIMD Simulation of Molecular Beam Scattering Experiments

(see also Figure 2.7(a) and Table 2.11), are given in the first row of the table. Probabilities for other impact energies are supplied in Appendix C.

Table 2.12: Statistical results for NVE (upper two rows) and NVT trajectories at 300 K (lower row). The models differ only by the thermalized surface, for all trajectories a single D_2O was sent on a clean surface with a kinetic energy of $E_{kin} = 0.7$ eV. The initial parameters were the 48 and selected 42 from Section 2.3.3, respectively, as explained in the text.

ensemble	no. of trajectories	P_{refl}	P_{mol}	P_{diss} (1-2)	P_{diss} (1-4)
NVE ¹	48	0.19	0.58	0.23	0.00
NVE ^{1,3}	42	0.19	0.55	0.26	0.00
NVT ²	42×2	0.12	0.54	0.24	0.11

¹ Propagation time 1.22 ps. ² Propagation time 4 ps. ³ A subset of the NVE/48 data set, corresponding to the same initial impact parameters as used for the NVT ensembles.

Thus, compared to the corresponding microcanonical trajectories (for 42 initial impact parameters), for the thermal surface we see the following differences: (i) The reflection probability is diminished (from 0.19 to 0.12); (ii) molecular adsorption is not much affected: a bit more than half of the trajectories adsorb molecularly in both cases; (iii) the *total* dissociation probability is increased (from 0.26 to 0.35); (iv) 1-4 dissociation appears in the thermal case to some extent. Among the 1-4 dissociations (nine trajectories out of 84), four reacted directly and five indirectly, *via* a molecular adsorbate. Note that all nine 1-4 dissociated trajectories led to molecular adsorption under microcanonical ($T = 0$) conditions. Despite the statistical limitations and short trajectories we note that surface temperature seems to have some effect, in particular on the probability and type of dissociation. Further inspection of the canonical / NVT trajectories shows that among the cases leading to molecular adsorption after 4 ps, also trajectories were found in which D_2O ended up at different Al CUS sites than expected from the position of first impact, due to molecular diffusion on the surface and / or trajectories undergoing multiple bounces.

2.3.5 Refined Surface Model

During a MBS experiment, after some time the surface will be precovered with water (fragments), which in turn will affect the reactivity of further molecules approaching the surface. In order to study the effects of precoverage, we considered a single water (D_2O) molecule on a (2×2) α - $Al_2O_3(0001)$, adsorbed as shown in Figure 2.2, either molecularly (a), as 1-2 dissociated species (b), or as 1-4 dissociated species (c). Note that in all cases, the water or hydroxyl group is adsorbed in the lower right (1×1) sub-cell, on the CUS Al site at lateral position

[0.33, 0.33] (*cf.* Figure 2.5(a)).

We now fire a second D₂O molecule with an initial kinetic energy of $E_{\text{kin}} = 0.7$ eV onto the surface as described in the previous section(s), choosing various rotational orientations and impact sites. The total propagation time is 1 ps. The selected, lateral impact points $[a_0, b_0]$ were chosen to be (i) either in the lower-right (1×1) sub-cell close to the Al CUS where the preadsorbed water (fragment) is situated, or (ii) in a neighbor (the lower left) (1×1) sub-cell around the corresponding CUS there. Individual trajectories are analyzed with respect to two criteria: (i) Their influence on the preadsorbed molecule (or molecular fragment), and (ii) the (reactive) behavior of the second, incoming molecule. We do this first for $T = 0$, using NVE AIMD calculations as in Section 2.3.3.

Let us consider what happens when D₂O hits the (1×1) subcell with already preadsorbed water (fragments). In Table 2.13, we list in analogy to Table 2.11, the outcomes of a subset of NVE trajectories for two selected impact sites $[a_0, b_0] = [0, 33, 0.33]$ (*i.e.*, direct hit of preadsorbed water or water fragment), and $[a_0, b_0] = [0, 35, 0.45]$ (*i.e.*, slightly nearby the Al CUS site, see Figure 2.5(e)). The table gives information for all preadsorption cases: molecular, 1-2 dissociated and 1-4 dissociated. In contrast to Table 2.11, we show *two* symbols for each entry, *e.g.*, “M, D(1-2)” to illustrate the fates both of the incoming molecule (the first symbol, “M” in this case) and the preadsorbed species (the second symbol, “D(1-2)” in this example). Further, a star (*) has been added to the second symbol, if the character of the preadsorbed species changed during the scattering process.

From the table, the following observations can be made.

- When the *incoming* molecule hits the Al CUS site with preadsorbed water or hydroxyl (*i.e.*, $[a_0, b_0] = [0.33, 0.33]$), in the (six) cases shown it is either reflected from there (first symbol, R), or it molecularly adsorbs after having diffused to another Al CUS site (first symbol, M).

Interestingly, during scattering the *preadsorbed* species may change its character in case of molecular preadsorption. In this case, preadsorbed D₂O is dissociated to 1-2 (second symbol, D(1-2)*), showing that part of the energy of the incoming water is used to overcome the barrier towards dissociation. Note that the character of the preadsorbed dissociated species (1-2 or 1-4) didn’t change in any of the examples shown.

- When the *incoming* molecule hits a position near the Al CUS of the preadsorbed species (*i.e.*, $[a_0, b_0] = [0.35, 0.45]$), we find a number of possible outcomes. In case of molecular

Table 2.13: Selected results of preadsorbed surface trajectories for the microcanonical ensemble (NVE, $T = 0$ K, $E_{\text{kin}} = 0.7$ eV). The three investigated cases are: molecular, 1-2 and 1-4 dissociated preadsorption. R=reflection, M=molecular adsorption (chemisorption), P=molecular physisorption, D(1-2)=1-2 dissociation, D(1-4)=1-4 dissociation. The two letters for each cell give the outcomes for the *incoming* molecule (first entry) and the *preadsorbed* water (second entry). For the case, that the preadsorbed species changed its character, a * is attached. "term." refers to terminated trajectories. Missing entries mean that no calculation was performed.

orientation [α, β, γ]	type of preadsorption					
	molecular		1-2 dissociated		1-4 dissociated	
	impact position [a_0, b_0] [0.33,0.33] [0.35,0.45]		impact position [a_0, b_0] [0.33,0.33] [0.35,0.45]		impact position [a_0, b_0] [0.33,0.33] [0.35,0.45]	
[0, 0, 0]		P, D(1-2)*		M, D(1-2)		R, D(1-4)
[0, 0, 90]		M, D(1-2)*		M, D(1-2)		P, D(1-4)
[0, 90, 0]	M, D(1-2)*	P, D(1-4)*	R, D(1-2)	M, D(1-2)	R, D(1-4)	P, D(1-4)
[0, 90, 90]		P, D(1-4)*		M, D(1-2)		term.
[90, 0, 0]		P, D(1-2)*		M, D(1-2)		M, D(1-4)
[90, 0, 90]		P, M		D(1-2), D(1-2)		P, D(1-4)
[90, 90, 0]		P, D(1-4)*		M, D(1-2)		R, D(1-4)
[90, 90, 90]	M, D(1-2)*	P, D(1-4)*	R, D(1-2)	M, D(1-2)	M, D(1-4)	P, D(1-4)

preadsorption, the second molecule physisorbs on the surface (P), adsorbing on the first water molecule or molecular fragment (hydroxyl). In general in this work we define a D_2O molecule as being physisorbed if it does not directly bind to an Al CUS, but instead to water (fragments), *e.g.*, by hydrogen bonds. As a result, one observes water clustering on the surface.

If the preadsorbed species on the CUS Al is hydroxyl (for 1-2 and 1-4), then reflection (R), molecular adsorption on a neighbor CUS (M), dissociation on a neighbor CUS (D), or physisorption (P) may occur. Note that molecular adsorption (on a neighbor CUS) clearly dominates, in particular for the 1-2 dissociated preadsorbed species. Concerning the fate of the *preadsorbed* species, we note that in case of molecular preadsorption all except one previously intact molecules have dissociated after 1 ps. Among the eight trajectories shown for $[a_0, b_0] = [0.35, 0.45]$, three dissociate to 1-2, three to 1-4, one to 1-4' and one preserves its molecular character. Again, none of the 1-2 or 1-4 preadsorbed species change their character upon impact of a second molecule, for the examples shown.

We also considered the case when D_2O hits the lower-left (1×1) sub-cell of the (2×2) cell where *no* water (fragment) is preadsorbed. First of all, we find that the preadsorbed water (fragment) is hardly affected in this case: out of 36 trajectories in total, only in a single

trajectory the preadsorbed species changed its character. Concerning the incoming D_2O , we find, somewhat surprisingly, an effect of preadsorbed neighbors: The dissociation probability increases, and, as a new reaction compared to Table 2.11, 1-4 dissociation occurs to some extent. Quantitatively, from 36 AIMD trajectories the incoming molecule dissociated in 13 cases ($P_{\text{diss}} = 0.36$), in five cases 1-4 dissociation was found ($P_{\text{diss}(1-4)}=0.14$). Further, the reflection probability drastically decreased to $P_{\text{ref}}=0.06$. Despite limited statistics, we interpret the reduced reflection probability as being due to attractive interaction of the incoming molecule with preadsorbed water, which also leads to enhanced dissociation. For a more complete statistics and a figure showing the impact points on the neighboring CUS see Appendix C.

In summary, we observe that preadsorption leads to new outcomes in water-alumina surface scattering (*e.g.*, physisorption, or clustering on the surface), and to the formation of 1-4 and 1-4' dissociated species, in particular by dissociating of preadsorbed, intact water molecules. Not too surprisingly, the effects are larger if the incoming molecule hits an area around an Al CUS where water or water fragments were preadsorbed.

We have also performed analogous calculations for thermal NVT ensembles at $T = 300\text{ K}$, with a single water molecule or its fragments preadsorbed on the surface. As in Section 2.3.4 we used molecular, 1-2 and 1-4 dissociated species of Figure 2.2 as starting points, equilibrated at 300 K for 1 ps and started a 1-ps “production run” with an incoming, additional water molecule ($E_{\text{kin}} = 0.7\text{ eV}$) from there. Here, once again, one has to differentiate between the incoming molecule hitting the (1×1) sub-cell with preadsorbed water (fragments), or a nearby sub-cell. Without going into details for 144 calculated trajectories run (see Appendix C for probabilities), we find similar results as for the NVE ensemble calculations with preadsorption, *e.g.*, physisorption (and clustering) and dissociation of molecularly preadsorbed species in addition to previously observed processes. However, there are also differences compared to the NVE calculations: For instance, reactivity towards dissociation for the preadsorbed, molecular species is somewhat diminished. As a further difference, in case of the second molecule hitting not the same, but a neighboring (1×1) sub-cell of the preadsorbed species instead, the dissociation probability of the incoming molecule increases somewhat compared to NVE, *i.e.*, the processes becomes more “non-local” in the thermal ensemble.

Furthermore, compared with the microcanonical clean surface AIMD, there is less dissociation.

2.3.6 Refined Beam Model

Enhancing the beam is a further refinement and is realized here in two different ways: by assuming a water cluster as the approaching species rather than a single molecule, and as a second improved method by exciting the water molecule rotationally, vibrationally and with a combination of both.

2.3.6.1 Clustering

As a cluster, the $(\text{D}_2\text{O})_4$ system was optimized in the same periodic boundary conditions as the cell before but without the surface, for the geometry see Figure 2.8. The same cluster was already shown to be the most stable one by Wales *et al.* [105], there it is called “up-down-up-down”. This cluster was then fired with a kinetic energy of 0.9 eV at the cold clean surface (NVE) from a distance of 4 Å (distance to the center of mass of the cluster) above the Al surface layer, with a duration of around 1.22 ps. Once again, several impact points (again defined for the center of mass position) and orientations of the cluster were considered. These orientations were applied analogously to the previous ones with the axes of the rotations shown in Figure 2.8(b).

Evaluating the data shows that the cluster breaks up upon contact with the surface into in-

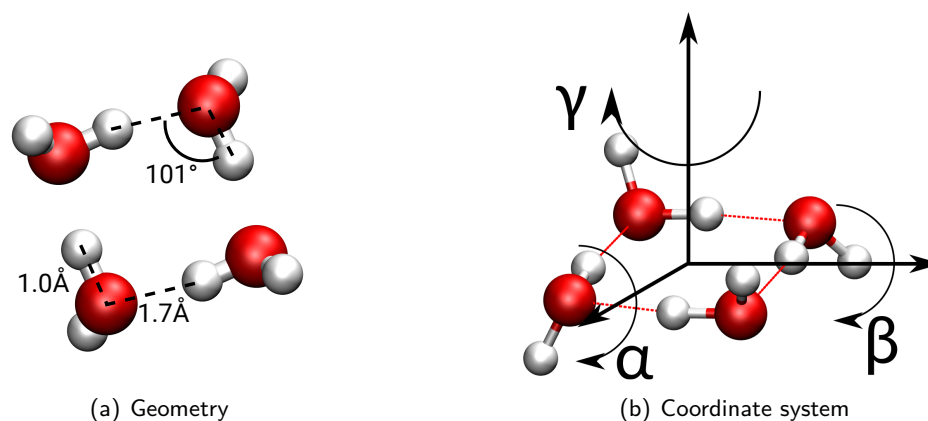


Figure 2.8: $(\text{D}_2\text{O})_4$ cluster for simulation of effects of higher coverages. (a) shows the optimized geometry, explaining the DOD bond angle and the OD bond lengths and (b) illustrates the coordinate system for the rotations along the axes with the angles α , β and γ .

dividual D_2O molecules and these undergo different processes, to a great extent influenced by the surrounding water molecules, due to the high coverage of 1 ML (the (2×2) supercell with its four CUS positions can hold up to four water molecules in one monolayer). The water can adsorb molecularly or dissociatively (both directly and indirectly), physisorb, deuterium atoms

can diffuse or single molecules can be reflected totally. Two examples of the final geometries can be found in Figure 2.9.

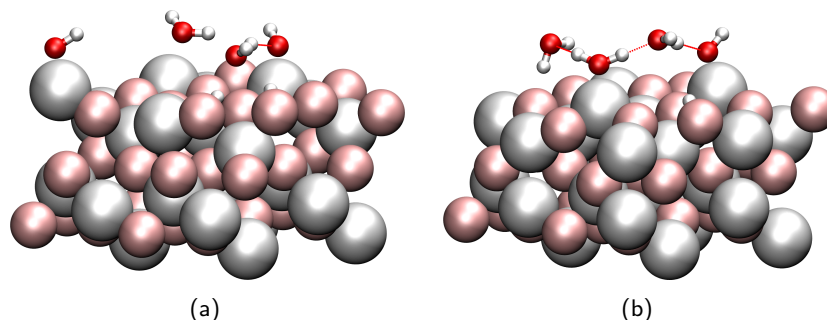


Figure 2.9: Side views of the last time step (1.22 ps) for two initial conditions: (a) $E_{\text{kin}} = 0.9 \text{ eV}$, $[a_0, b_0] = [0.5, 0.35]$, and $[\alpha, \beta, \gamma] = [0, 0, 0]$ and (b) $E_{\text{kin}} = 0.9 \text{ eV}$, $[a_0, b_0] = [0.35, 0.5]$, and $[\alpha, \beta, \gamma] = [90, 90, 0]$. Hydrogen bonds are shown as red dashed lines. Physisorption, molecular adsorption and dissociation can be seen in both snapshots.

Mostly independent of the settings, the molecules interact strongly with each other showing a profoundly dynamic behavior. This gives rise to processes that were not possible for the clean surface NVE and a single water situation, where no 1-4 dissociation nor physisorption were observed. Of course, the probabilities for dissociation, molecular adsorption and reflection are different, the probability of molecular adsorption is strongly diminished to the advance of 1-2, 1-4 and 1-4' dissociation and physisorption. For details see Appendix C.

2.3.6.2 Rotationally and Vibrationally Preexcited Water

Qualitative results are given for a D_2O molecule which is not cold as before but excited rotationally and/or vibrationally at the beginning of the trajectory. It is shot with a kinetic energy of 0.7 eV at the clean surface in an NVE ensemble for a trajectory duration of 2 ps at the impact point $[0.35, 0.5]$ with the initial orientation $[0, 0, 0]$. With these applied conditions in the “cold” case (microcanonical ensemble at 0 K without rotational or vibrational excitation), the molecule dissociates to the 1-2 structure, the same for the thermalized surface at $T = 300 \text{ K}$.

The vibrational excitations were chosen as follows: For the single water molecule in the periodic boundary conditions a normal mode analysis was executed. The eigenvectors of the dynamical matrix for the symmetric stretch, asymmetric stretch and the bending mode were used: The eigenvectors of the dynamical matrix equal normal mode displacements. They were scaled by a factor of 0.1 and these positions were used as initial positions for the dynamics, giving a vibrational energy of around 0.05 eV. This corresponds to an atom displacement along

2.3 AIMD Simulation of Molecular Beam Scattering Experiments

normal modes out of the equilibrium position, *i.e.*, a vibrational excitation. It was used as an input for the MD trajectories in addition to the initial momentum towards the surface. For the rotational preexcitations along the three axes, D atoms were given initial momenta to induce a rotational motion corresponding to rotational energies of ~ 0.2 eV.

The results for the rotation around the γ -axis (*cf.* Figure 2.4) shows molecular adsorption whereas rotations around the other two axes give 1-2 dissociation as in the initial microcanonical trajectories without rotational excitation. In the cases of vibrational preexcitation, the symmetric stretch leads to reflection, the asymmetric stretch gives 1-4' dissociation after initial 1-2 dissociation (as was already addressed in Figure 2.6(d)) and with the bending mode being excited, the water dissociates to 1-2. Also, a small collection of combinations of vibrations with rotations were calculated that lead to either molecular adsorption (rotation around α and bending mode), or 1-2 dissociation (rotation around γ and asymmetric stretch; rotation around β and symmetric stretch).

Quantitatively, the results may depend strongly on the excitation energy which was not of concern here, one can say that preexcitation has an effect on the dynamics of the water adsorption and dissociation, respectively that were not possible with the cold water molecule.

In this section, AIMD calculations were done to model molecular beam scattering of heavy water on an α -Al₂O₃(0001) surface. In respective experiments, molecular and dissociative adsorption has been observed, the latter in the form of modes of the 1-2, 1-4 and 1-4' dissociated species, with a much higher dissociation probability than in pinhole dosing.

In the simplest model, where a single D₂O molecule approaches the cold, clean surface, we find reflection, molecular adsorption and 1-2 dissociation only. For dissociation, a minimum translational energy of the incoming molecule seems to be required, which may already be a hint to the fact why under MBS conditions dissociation is facilitated compared to pinhole dosing.

To find the experimentally verified 1-4 and 1-4' dissociated species, at least one of the following conditions has to be fulfilled: A thermal surface (here 300 K), the preadsorption with molecular or dissociated water, the formation of water clusters in the beam, and the internal excitation (rotational or vibrational) of the incoming water molecules.

Apart from the mentioned processes, we have observed other channels and phenomena such as clustering of water (fragments) on the surface by H-bonding, chemisorption and physisorption, diffusion of water fragments, and collision induced chemical reactions, *e.g.*, dissociation of adsorbed molecular water by the incoming D₂O molecule.

A rich chemistry evolves already on the ps time scale under more complex and realistic conditions. The aforementioned processes can be direct or indirect, *i.e.*, via (multiple) bounces

2 Water on α - $\text{Al}_2\text{O}_3(0001)$

at the surface or by sequences of reactions in which certain species appear as short-lived intermediates.

The main focus of this work was the qualitative analysis of water scattering at the α - $\text{Al}_2\text{O}_3(0001)$ surface under increasingly complex conditions. However, also semi-quantitative analyses were carried out, notably for the relative occurrence of the different products under different initial conditions. We could find dependencies on the initial translational energy, rotational orientation, but even more on the impact site. Also, dissociation is strongly favored when the incoming molecule hits the surface already in a “product-like” configuration. These findings were published in Reference [92].

Although a large number of trajectories were computed with the contingent at the HLRN facility, a reliable statistical analysis was not possible. Also some parameters (*e.g.* different angles under which the beam hits the surface) have not been studied, and quantum effects were not considered. The dynamics were restricted to the ps time scale.

3 Water on α -Al₂O₃(11 $\bar{2}$ 0) [104]

The (11 $\bar{2}$ 0) surface of α -Al₂O₃ is the third most stable one under UHV conditions and was not studied extensively so far, as discussed in the introduction. Until now only a few experimental studies were performed for the (11 $\bar{2}$ 0) surface: X-ray reflectivity measurements by J. Catalano [106], who found that the surface is oxygen terminated and has two differently coordinated kinds of surface Al atom dimers (groups of two Al atoms that form dimers by the reconstruction of the surface). LEED measurements by Becker *et al.* [107] showed a well defined (1 × 1) diffraction pattern and found evidence that the surface is unreactive with hydrogen at room temperature. The theoretical work of Marmier [108] suggested that hydrogen is unreactive because the surface is fully hydroxylated at room temperature, even under UHV conditions. In the work of Waychunas and coworkers [109], SFG spectra were measured under ambient conditions (room temperature and air). They found two different types of oxygen atoms on the surface, twofold and threefold coordinated ones. The authors assumed that the threefold coordinated O will only be protonated under highly acidic conditions. They also gave evidence for molecularly adsorbed water on the surface. However, all experimental studies [106,107,109] assume a high-coverage situation, whereas this theoretical study is mostly focused on the low-coverage regime. With theoretical methods, so far only the clean surface was studied by two different groups: Kurita *et al.* [21] and Marmier [108]. Both papers disagree concerning the stability, in the work of Kurita, the (11 $\bar{2}$ 0) surface is the third most stable surface cut, whereas in the publication of Marmier, it is the fourth most stable cut.

In this work we want to relate to SFG results for low-coverage experiments conducted by the Campen group from FHI Berlin, and to study reactivity of water at (11 $\bar{2}$ 0) surface.

3.1 Surface Models

Our studies were done for a slab model of the O-I terminated (11 $\bar{2}$ 0) surface, which was found to be the most stable one of five possible terminations in the theoretical work of Kurita *et al.* [21]. This is a stoichiometric, oxygen-terminated surface that is lower in energy than any other Al- or O-terminated (11 $\bar{2}$ 0) surface. In Section 3.2.3 the less stable O-II termination is also studied to account for a defect site.

3 Water on α - $\text{Al}_2\text{O}_3(11\bar{2}0)$

To allow for low water coverages, a (2×2) supercell was cut from the bulk. In Figure 3.1(a), the $(11\bar{2}0)$ surface plane and the (0001) surface which was studied earlier in this work (Section 2) can be seen. In Figure 3.1(b) the top view is shown and Figure 3.1(c) gives the side view and

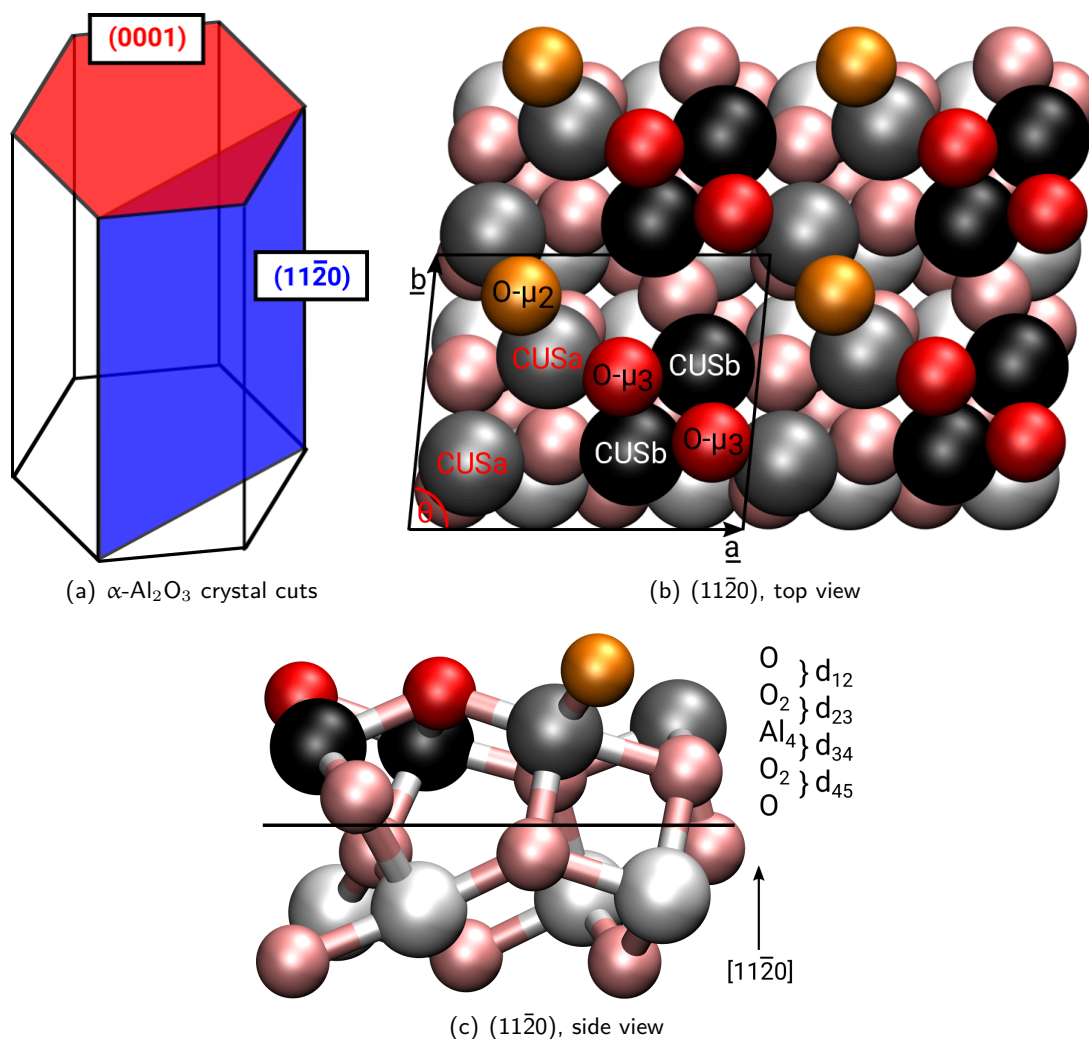


Figure 3.1: The $(11\bar{2}0)$ surface cut of α - Al_2O_3 , (a) schematic view of the Al_2O_3 crystal, where both the (0001) and the $(11\bar{2}0)$ surface are shown, (b) a top view of the geometry optimized (2×2) supercell of $(11\bar{2}0)$ of the most stable O-I termination, with the nomenclature of the surface atoms used in this work. We distinguish two types of surface Al atoms (gray CUSa and black CUSb, where CUS is the abbreviation for coordinatively unsaturated site) as well as the twofold and threefold coordinated oxygen atoms (orange $\text{O}-\mu_2$ and red $\text{O}-\mu_3$). Subsurface atoms are indicated by pale colors. (c) gives the side view, for convenience of the (1×1) cell, showing the distinct atomic layers, again with the same color code as in (b). The atoms below the solid line (the lowest five from ten layers) were fixed to bulk coordinates for optimizations and frequency analyses.

the atomic layer sequence O-O₂-Al₄-O₂-O... for the (1 × 1) cell which is O₄-O₈-Al₁₆-O₈-O₄..., respectively for the (2 × 2) cell that was applied in this work. The supercell model that is mostly used in this work has ten atomic layers (two times this layer sequence, 32 Al and 48 O atoms), with the lowest five fixed to the bulk value to mimic the surface situation. However, for the calculations of the lattice vibrations up to 30 layers were considered (in steps of five, see Figure 3.2). For each system size, the lowest five layers were fixed (to the bulk values optimized with PBE+D2/PW). The largest system (30 layers) was only used for one MD calculation due to its high computational effort, so in most cases the maximum layer thickness was 25.

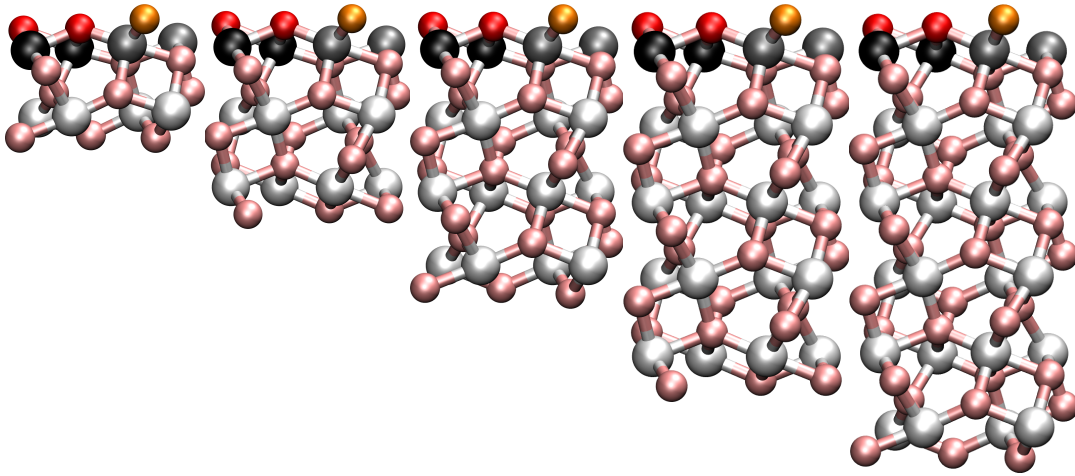


Figure 3.2: Side view for the different cell sizes for 10, 15, 20, 25 and 30 layers in z-direction. Surface atoms are shown in the color code clarified before. For each model size, the lowest five layers were kept fixed to bulk values.

For the (2 × 2) supercell with the 10 layer system k -points were sampled for five different grid sizes from (1 × 1 × 1) to (5 × 5 × 1) Monkhorst-Pack grids [110]. In contrast to the even grid sizes, the odd ones contain the Γ -point and therefore are favorable. It can be deduced from Figure 3.3 that the (3 × 3 × 1) grid is already converged with respect to the energy of the clean surface and will be used for all further calculations.

The unit cell has a topmost layer of oxygen (O layer) in which each O atom is coordinated to two Al atoms of the underlying lattice. Below this layer is a second oxygen layer (O₂ in Figure 3.1(c)). These O atoms are threefold coordinated by Al atoms. Following the usual nomenclature in coordination chemistry, the two types of O atoms are denoted as O- μ_2 and O- μ_3 , respectively. In previous studies these have also been described as Al₂O and Al₃O [109]. Below these surface oxygen layers is a layer of surface Al atoms (Al₄, consisting of four Al atoms in the (1 × 1) cell). Within this Al layer there are two different coordinatively unsaturated (CUS) Al atoms, called here CUSa and CUSb, respectively. By inspecting Figure 3.1(b) it

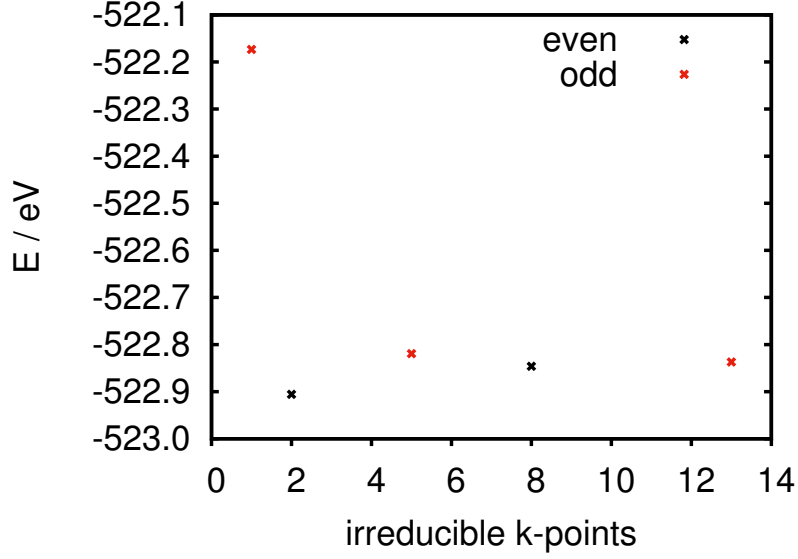


Figure 3.3: PBE+D2 energies for the clean surface (10 layer slab) as a function of the number of \underline{k} -points. Shown is the energy of the optimized supercell with respect to the number of \underline{k} -points in the irreducible part of the first Brillouin zone. The even values correspond to the $(2 \times 2 \times 1)$ (2 \underline{k} -points in the irreducible part of the first Brillouin zone) and $(4 \times 4 \times 1)$ (8), whereas the odd, which contain the Γ -point, are described by $(1 \times 1 \times 1)$ (1), $(3 \times 3 \times 1)$ (5) and $(5 \times 5 \times 1)$ (13).

may become clear that CUSa Al atoms are covalently bound to one $\text{O-}\mu_2$, one $\text{O-}\mu_3$ and three deeper lying oxygen atoms, while CUSb atoms are covalently bound to two $\text{O-}\mu_3$ and three deeper lying oxygens. In this work, the gray spheres denote the CUSa atoms, the black ones depict the CUSb atoms. The twofold coordinated oxygen atoms ($\text{O-}\mu_2$) are shown in orange and the threefold coordinated ($\text{O-}\mu_3$) in red. Atoms of the underlying layers are illustrated in pale colors, light gray for alumina and pale red for oxygen.

In the upper three layers of the (2×2) cell, we have 16 CUS sites (eight CUSa and eight CUSb), four $\text{O-}\mu_2$ and eight $\text{O-}\mu_3$ sites. The corresponding cell vectors \underline{a} and \underline{b} were adopted from the bulk structure. These are for this particular surface cut $|\underline{a}| = 10.36 \text{ \AA}$, $|\underline{b}| = 14.16 \text{ \AA}$ and for the vector \underline{c} perpendicular to the surface a length of $|\underline{c}| = 20.5 \text{ \AA}$ was assumed. The angle θ between \underline{a} and \underline{b} is 84.56° .

For the supercell model, a vacuum gap in z -direction (perpendicular to the surface, 17 \AA for the 10 layer slab, 15 \AA , 13 \AA , 11 \AA and 9 \AA for the 15, 20, 25 and 30 layer slabs, respectively) was introduced to avoid spurious, unphysical interaction between the slabs in this direction.

The spacing between the five top layers for each slab size is also displayed in Table 3.1. Upon relaxation the spacing between these layers is slightly changed compared to the bulk

crystal as given in Table 3.1. The uppermost layer distance increases while it decreases for the deeper ones. A major issue of the optimization apart from layer spacing is that the interatomic

Table 3.1: Distances between the top five layers (see also numbering in Figure 3.1(c)) for different PBE+D2 optimized slab sizes ($(3 \times 3 \times 1)$ k -point grid) and the unrelaxed bulk structure (right column) from theory. All values are given in Å.

distance	atomic layers				bulk
	10	15	20	25	
d_{12}	0.23	0.23	0.25	0.25	0.19
d_{23}	0.64	0.65	0.64	0.64	0.74
d_{34}	0.66	0.66	0.67	0.67	0.74
d_{45}	0.20	0.21	0.21	0.21	0.19

distances of surface Al species change, here exemplarily for the 10 layer slab: the CUSa–CUSa distance increases from 2.682 to 2.994 Å, the CUSa–CUSb distance increases from 2.833 to 2.876 Å whereas the CUSb–CUSb distance decreases from 2.682 to 2.499 Å. The pairs of CUSa and CUSb can be interpreted as the Al dimers in the work of Catalano [106].

3.2 Water Adsorption: Adsorption Energies and Geometries

3.2.1 Low Coverage

After optimization of the UHV surface termination, in a next step, water adsorption on the 10 layer relaxed $(11\bar{2}0)$ surface model was studied, using PBE+D2, and the same computational parameters as above. To study water adsorption, first a low-coverage regime was investigated: One water molecule per (2×2) supercell, which equals a coverage of $1/12^{1,2}$. For this a water molecule was put at different positions on the surface and the system was relaxed. By doing so one molecular minimum and several dissociated species including both CUS and oxygen types were found. The multitude of different surface atoms gives rise, for the dissociated water molecule, to a large variety of possible adsorption geometries for the next neighboring situation (OH and H residue are adsorbed on two neighboring surface atoms). The variety is even increased when considering adsorbate structures with greater distance between the dissociated

¹ There are 16 CUS sites per (2×2) supercell, but adsorption does not occur on CUSa but only at a position between two CUSa atoms, which gives a maximum of 12 adsorption sites for 1 monolayer. See also Section 3.2.2.

² Tests with a symmetric slab (where at the top and the bottom water is adsorbed) were computed, confirming that the asymmetric model (water is only adsorbed on one side of the slab) including dipole corrections is sufficient to describe the system. Details for this are given in Appendix D.

3 Water on $\alpha\text{-Al}_2\text{O}_3(11\bar{2}0)$

water fragments. Adsorption energies and Gibbs free energies at various temperatures of the resulting, dissociated next neighbor species can be seen in Table 3.2, along with the molecular species (see also Figure 3.4). The adsorption energy is defined (analogously to Equation (2.1) in Section 2) as the energy of the adsorbed species compared to the energies of the clean surface and the free water molecule. The nomenclature for the adsorption sites which is used in the following gives at first the type of Al site where the OH residue (or OH^-) is adsorbed and at second place the oxygen type where the H (H^+) is adsorbed: OH site||H site. The term “inter” characterizes a position between two CUS atoms which leads to a bidentate adsorption pattern. The additional notation with ' denotes greater distances between the residues. Direct neighbors do not have a ', the next neighbor structure is displayed by a single ', one position farther '' and the most distant position is ''' due to the periodic boundary conditions.

Table 3.2: For molecular and (singly) dissociated water on a (2×2) cell of $\alpha\text{-Al}_2\text{O}_3(11\bar{2}0)$, adsorption energies E_{ads} and Gibbs free energies G_{ads} for different temperatures for the 10 layer slab are given in eV. E_{ads} was calculated from Equation (2.1) and G_{ads} is defined analogously. These results were obtained with PBE+D2. The three most stable species are marked with bold letters.

Adsorbed Species		E_{ads}	$G_{\text{ads}, 130 \text{ K}}$	$G_{\text{ads}, 300 \text{ K}}$	$G_{\text{ads}, 400 \text{ K}}$
molecular	CUSb	-1.78	-1.60	-1.51	-1.46
	inter-CUSa O-μ_2	-2.50	-2.27	-2.16	-2.09
	inter-CUSa O- μ_3	-1.67	-1.44	-1.33	-1.27
dissociated	CUSb O-μ_2	-2.28	-2.12	-2.03	-1.97
	CUSb O- μ_3	-1.19	-1.05	-0.98	-0.95
	inter-CUSb O-μ_2	-2.09	-1.88	-1.80	-1.76
	inter-CUSb O- μ_3	-1.89	-1.71	-1.63	-1.58

Our structure search suggests that a single water molecule adsorbs with an adsorption energy of -1.78 eV on CUSb. Molecular adsorption between two CUSa (inter-CUSa) or between to CUSb (inter-CUSb) does not occur at the level of theory employed here. Geometries with starting conditions at these sites show dissociation. The molecular minimum is substantially less stable than most of the dissociated species. Also, we find that all six next neighbor combinations of OH^- and H^+ sites are minima in our model. On the contrary, the dissociated water, where the twofold coordinated surface oxygen atom is addressed, is very stable, even in comparison to the more stable surface cuts (0001) and $(11\bar{1}02)$ that were previously investigated in our group in References [76, 78]. Dissociated species where the proton is located at a twofold coordinated surface oxygen are far more stable than the corresponding systems where the threefold coordinated oxygen is occupied. This is due to the higher negative charge and the

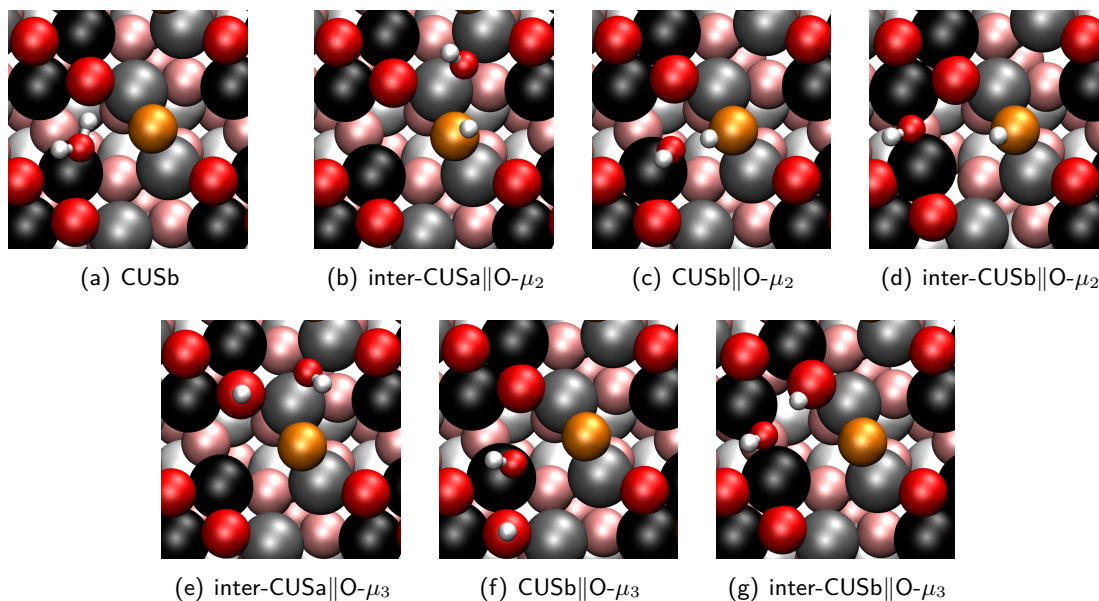


Figure 3.4: Top view of the adsorption geometries for molecular CUSb (a) and the next neighbor dissociated water ((b)-(g)). The color code is the same as in Figure 3.1(b) and (c), CUSa gray, CUSb black, O- μ_2 orange and O- μ_3 red; hydrogen is illustrated in white; the oxygen from water is in red but as a smaller sphere to make it distinguishable from the surface O atoms; subsurface layers are shown in pale colors.

higher basicity of such twofold coordinated oxygen atoms O- μ_2 , in comparison with the more saturated threefold coordinated O- μ_3 oxygen atom. In fact, the adsorption can be seen as a Lewis acid / base reaction [111] with the undercoordinated aluminum being the Lewis acid and the oxygen of the water molecule being the base.

The adsorption of OH at an inter-CUSa site is more favorable than at a CUSb site, because the former corresponds to a site where in the bulk system another oxygen atom would be situated, which is not the case for the CUSb position. Additionally, the CUSb position is electronically³ and sterically more hindered because of the twofold and threefold coordinated oxygen atoms in the surroundings.

Dissociated species with fragments in direct neighborhood as shown in Table 3.2 and Figure 3.4 are more stable than those where the proton and the OH residue are farther apart (see Table 3.3), given the OH residue has a stabilizing effect on the H and vice versa. What first seems to disagree with the former said is that the inter-CUSb||O- μ_3''' -species is more stable than the species inter-CUSb||O- μ_3'' (where the OH groups are closer to each other). However, this

³ Two electron rich oxygen atoms are nearby, that also cause a repulsion by the elevated local negative charge.

is due to the fact that in the unit cell the fragments of $\text{inter-CUSb}\|\text{O-}\mu_3''$ are closer but in the periodic boundary conditions actually the distance between OH and H in $\text{inter-CUSb}\|\text{O-}\mu_3'''$ is smaller. The distances between the neighboring OH groups in the $\text{O-}\mu_3''$ system are 6.76 and 7.71 Å, compared to 9.34 and 6.16 Å in the $\text{O-}\mu_3'''$ system (the numbers refer to the two possible distances in the periodic system, direct and “over the border” of the unit cell). The latter seems to be farther away, but due to the periodic boundary conditions, one of the inter-adsorbate distances is smaller (6.16, compared to 6.76 Å), which leads to the stabilization.

Table 3.3: Comparison of adsorption energies for next neighbor dissociated species (without '), and dissociated species where OH and H are farther apart (with one, two or three '). Results are given in eV (10 layer slab).

Adsorbed Species	E_{ads}
$\text{inter-CUSa}\ \text{O-}\mu_3$	-1.67
$\text{inter-CUSa}\ \text{O-}\mu_3'$	-1.42
$\text{inter-CUSb}\ \text{O-}\mu_3$	-1.89
$\text{inter-CUSb}\ \text{O-}\mu_3''$	-1.16
$\text{inter-CUSb}\ \text{O-}\mu_3'''$	-1.22

Besides, water adsorption for systems with additional atomic layers (up to 25 in total) were studied to check convergence with respect to layer thickness. These optimized geometries do not differ strongly from the 10 layer ones and hence are not shown. The corresponding adsorption energies are shown in Table 3.4. The adsorption energies do not change largely with increasing slab size. The molecular species still is less stable than the $\text{O-}\mu_2$ dissociated species and is more stable than the $\text{O-}\mu_3$ dissociated ones (except for $\text{inter-CUSb}\|\text{O-}\mu_3$ dissociated system). $\text{inter-CUSa}\|\text{O-}\mu_2$ is the most stable structure for all sampled system sizes, $\text{inter-CUSb}\|\text{O-}\mu_2$ and $\text{CUSb}\|\text{O-}\mu_2$ change their stability (it approaches to nearly the same value for 25 layers) depending on the number of layers but still are some orders of magnitude less probable than $\text{inter-CUSa}\|\text{O-}\mu_2$ ⁴. Dissociated systems occupying the threefold coordinated surface oxygen atom remain in the same stability order. Table 3.4 shows that the most stable systems are already converged for the 10 layer slab with regard to adsorption energies (and also vibrational OD stretch frequencies as it will be seen in Section 3.4.1).

⁴ See discussion in Section 3.4.1.1.

Table 3.4: Adsorption energies E_{ads} calculated from Equation (2.1) for molecular and dissociated species, as a function of layer thickness. All values are given in eV. The most stable systems (inter-CUSa||O- μ_2 , CUSb||O- μ_2 and inter-CUSb||O- μ_2) are highlighted in bold letters.

System	10 layers	15 layers	20 layers	25 layers
CUSb	-1.78	-1.80	-1.81	-1.83
inter-CUSa O-μ_2	-2.50	-2.46	-2.54	-2.56
inter-CUSa O- μ_3	-1.67	-1.67	-1.78	-1.80
CUSb O-μ_2	-2.28	-2.35	-2.36	-2.35
CUSb O- μ_3	-1.19	-1.71	-	-
inter-CUSb O-μ_2	-2.09	-2.43	-2.48	-2.36
inter-CUSb O- μ_3	-1.89	-1.59	-1.65	-2.09

3.2.2 Higher Coverages

Furthermore, systems with a higher water coverage were investigated, which offer the possibility to consider interaction between the adsorbate molecules. For the (2×2) supercell approach of the clean surface there are 16 CUS Al-atoms. Theoretically, these 16 atoms could be covered with water to gain 1 monolayer (ML). Eight of these 16 CUS atoms are CUSa and eight CUSb. On top of CUSb, a water molecule/OH residue can adsorb, but on top of a CUSa the adsorbate roams to a bridging inter-CUSa position between two CUSa. Thus, the number of potential adsorbates is decreased to twelve forming 1ML. Some exemplary cases for two water molecules ($2/12=16.6\%$ coverage), four inter-CUSa||O- μ_2 ($4/12=33.3\%$ coverage) and a fully covered supercell (twelve molecules, $12/12=100\%$ coverage) within a (2×2) supercell 10 layer slab model are shown in Figures 3.5 and 3.6. For these systems also normal mode analyses were carried out to get vibrational spectra, see Section 3.4.1.3 and Appendix E.

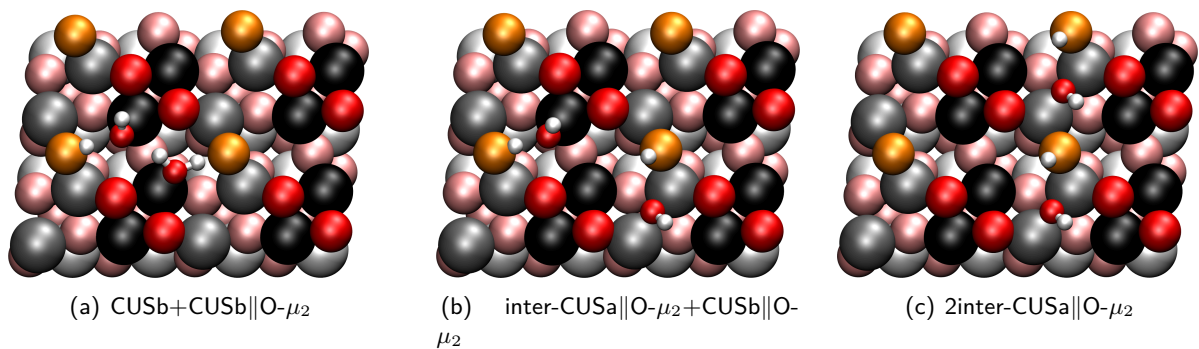


Figure 3.5: PBE+D2 optimized geometries of systems with two water adsorbates per (2×2) cell: (a) molecular CUSb and CUSb||O- μ_2 , (b) the two most stable species inter-CUSa||O- μ_2 and CUSb||O- μ_2 and (c) 2inter-CUSa||O- μ_2 .

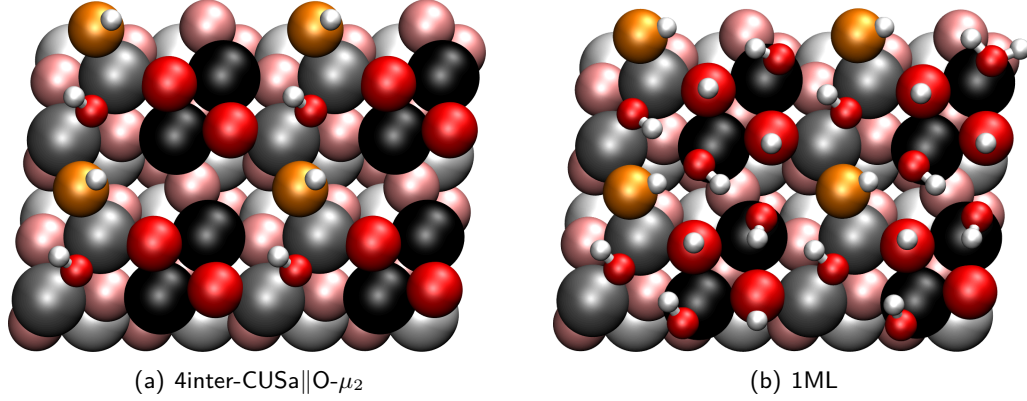


Figure 3.6: Optimized structures of the (a) 4inter-CUSa||O- μ_2 (four water molecules) and (b) fully covered (1ML) system (twelve water molecules). The latter one shows one molecular species and several hydrogen-bonded OH groups.

The adsorption energy of species with n adsorbed water molecules was calculated as

$$E_{\text{ads}} = E_{\text{ads. species}} - (n \times E_{\text{free water molecule}} + E_{\text{surface}}). \quad (3.1)$$

In Table 3.5, the adsorption energies for the high-coverage species mentioned above are given. There are also the results for the higher coverages in comparison to results in the low-coverage

Table 3.5: Adsorption energies E_{ads} from Equation (3.1) for higher water coverages in eV. For better comparison the adsorption energy per water molecule, the non-interacting adsorption energy from Equation (3.2) and the stabilization energy $E_{\text{stab.}}$ from Equation (3.3) are given. Also the coverage and number of water molecules per cell can be found here.

Adsorbed Species	E_{ads}	$E_{\text{ads,non-int.}}$	$E_{\text{stab.}}$	$\frac{E_{\text{ads}}}{n}$	Coverage	H ₂ O/cell
CUSb(mol)+CUSb O- μ_2	-4.57	-1.78+(-2.28)=-4.06	-0.51	-2.29	1/6	2
inter-CUSa O- μ_2 +CUSb O- μ_2	-4.77	-2.50+(-2.28)=-4.78	+0.01	-2.39	1/6	2
2inter-CUSa O- μ_2	-4.84	$2 \times (-2.50) = -5.00$	+0.16	-2.42	1/6	2
4inter-CUSa O- μ_2	-9.55	$4 \times (-2.50) = -10.00$	+0.45	-2.39	1/3	4
12H ₂ O	-23.39	^a	-	-1.95	1/1	12

^a In good approximation, there are 4 inter-CUSa-OH groups, 8 CUSb-OH groups, 8 O- μ_3 and 4 O- μ_2 OH groups, hence one can not calculate $E_{\text{ads,non-int.}}$.

limit presented by calculating the non-interacting adsorption energy with Equation (3.2) (see also Table 3.5)

$$E_{\text{ads,non-int.}} = E_{\text{ads, species 1}} + E_{\text{ads, species 2}}, \quad (3.2)$$

3.3 Dissociation and Diffusion Reactions of Water Species

and with that the stabilizing energy $E_{\text{stab.}}$:

$$E_{\text{stab.}} = E_{\text{ads}} - E_{\text{ads,non-int.}} \quad (3.3)$$

The structures were chosen exemplarily such that the neighborhood effect shows three different outcomes: it can have a stabilizing effect, where the dissociated water stabilizes the molecularly adsorbed water in CUSb(mol)+CUSb||O- μ_2 (Figure 3.5(a)). It can also have the contrary effect, as can be seen in the 2inter-CUSa||O- μ_2 , which becomes less stable (Figure 3.5(c)). On the other hand, there is the inter-CUSa||O- μ_2 +CUSb||O- μ_2 , which is merely affected by the neighboring OH residues (Figure 3.5(b)).

3.2.3 Other Surface Terminations

Up to this point, only the most stable O-I termination was considered.

In experimental LEED data of the clean surface [104], the analysis of the data gave two sublattices, one of them can be clearly identified as the most stable O-I termination and the other one remains unidentified. This unknown lattice could be a defect surface or another surface termination but this suggestion could not be confirmed yet by experimental data since preparation and probing turns out to be difficult. To pursue this thesis, a “defect surface”, the O-II terminated surface, as it is called in the nomenclature of Kurita [21], was calculated. This is the second most stable surface termination under most chemical potential conditions, mostly in Al-rich environment. In this termination, the topmost oxygen layer of the O-I termination is missing. As for the O-I termination, ten layers were considered and from these the lowest five layers were kept fixed to bulk values. Both the clean surface and one possible configuration of the fully covered (1 ML) surface were optimized (see Figure 3.7) and frequency calculations were performed to obtain vibrational modes, see Appendix E. The structure of the clean surface, of course, differs by the “missing” oxygen O- μ_2 atoms in the topmost layer, and the fully covered system is even more different: out of twelve water molecules that can adsorb, seven adsorb molecularly and five dissociatively. In comparison, the fully covered system for the O-I termination only shows one molecularly adsorbed molecule (*cf.* Figure 3.6(b)).

3.3 Dissociation and Diffusion Reactions of Water Species

Based on the minimum structures one has to identify reaction pathways linking these minima to fully understand the reactivity of a system. We utilize the NEB method including climbing image to search for transition states between the minima of the 10 layer slab. For coverage 1/12 (one molecule per (2×2) cell of the O-I terminated surface), we examined three different

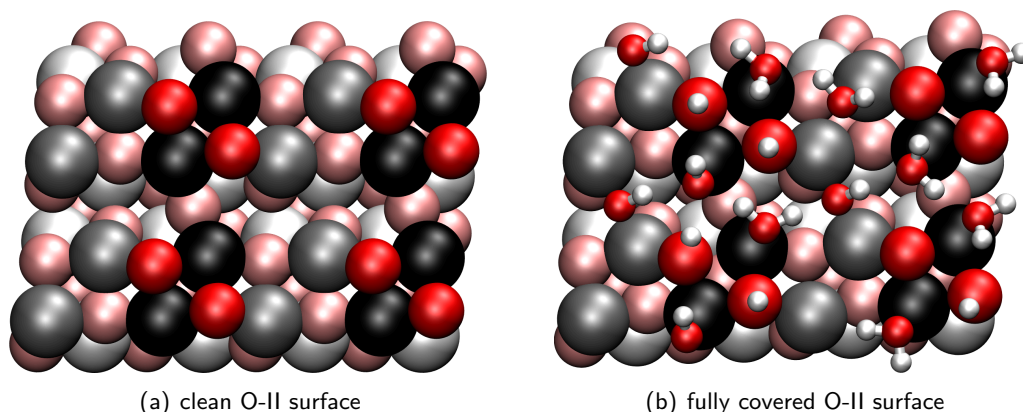
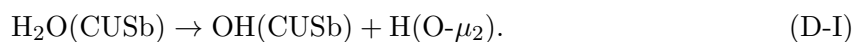


Figure 3.7: O-II terminated surface, as an example of a defect site optimized with PBE+D2. The top layer oxygen atom from the O-I terminated surface is missing and gives rise to a different chemical behavior. (a) clean surface, (b) 1ML water adsorbed surface.

types of reactions: dissociation from the molecular minimum, as well as OH- and H-diffusion. The dissociation reactions are named D, diffusion reactions as Df-OH and Df-H, respectively, in Table 3.6 and Figures 3.8 and 3.9. In addition, molecular water diffusion on the surface is supposable but due to the low stability, it will dissociate before diffusion can occur.

We investigated two distinct dissociation reactions: the reactions from CUSb to the twofold coordinated oxygen (D-I) and one to the threefold coordinated $\text{O-}\mu_3$ (D-II).

As can be seen from Table 3.2 (Section 3.2), the molecular minimum CUSb has a lower stability compared to the $\text{O-}\mu_2$ dissociated minimum. The reaction D-I leads from the molecular minimum at CUSb to the twofold coordinated oxygen of $\text{CUSb}||\text{O-}\mu_2$:



This reaction is very exoenergetic and exergonic. The free energy barrier is very low, about 0.002 eV as one can see from Table 3.6 and Figure 3.8(a), hence the reaction rate constant is very high, in the order of $k(300\text{ K}) = 5.76 \times 10^{12}\text{ s}^{-1}$. This barrier is probably too low due to the underestimation of barrier heights [112] with the used functional PBE. However, the same applies for all other transition states and rate constants for analogous dissociation reactions also on (0001) and $(1\bar{1}02)$ surfaces so that a comparison can be made. This analysis suggests, that the $(11\bar{2}0)$ surface is the most reactive of the three surfaces [76, 78].

3.3 Dissociation and Diffusion Reactions of Water Species

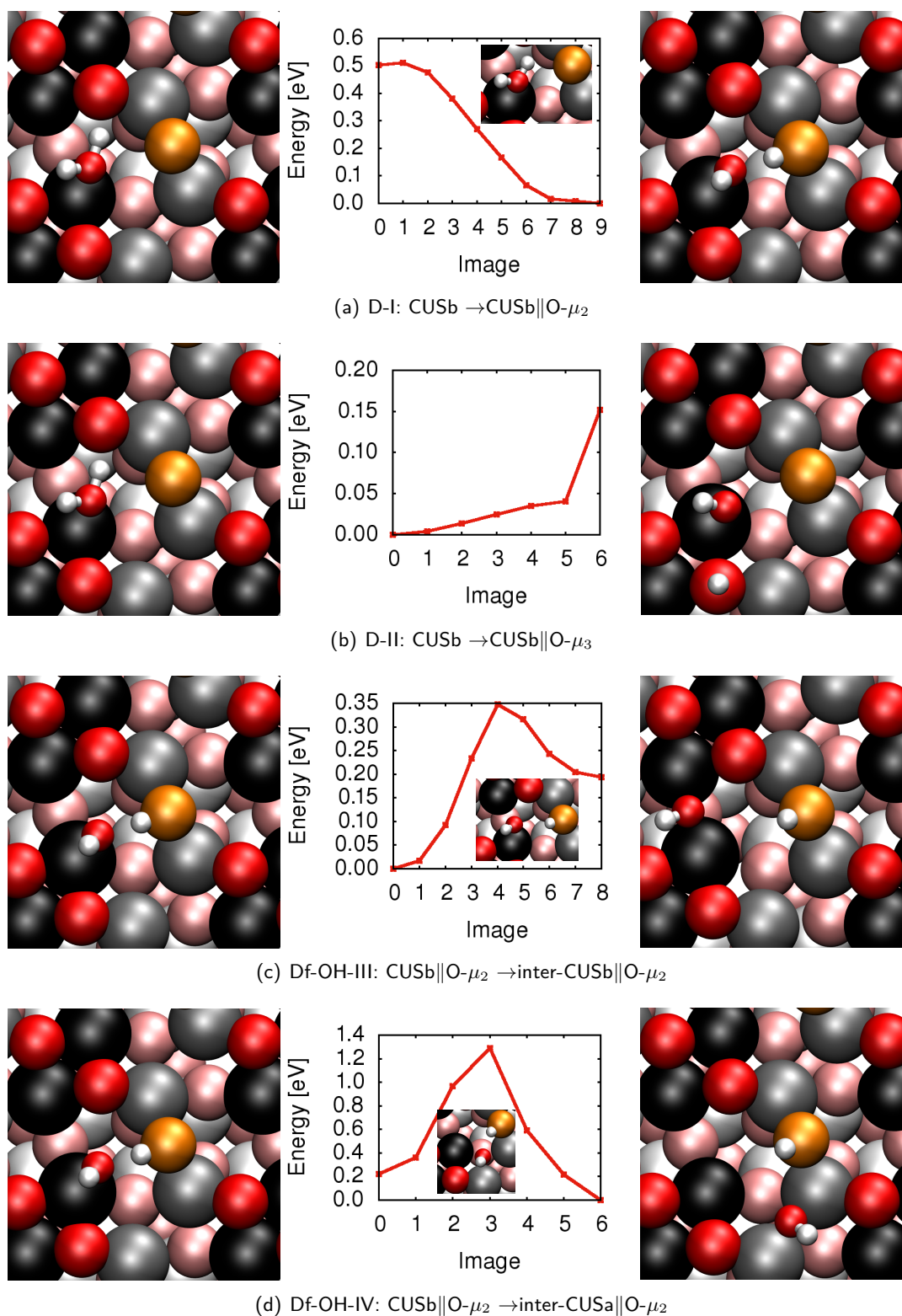
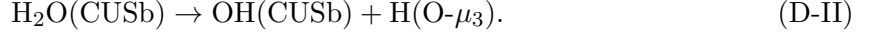


Figure 3.8: Minimum energy paths with transition states (inlay; if available), and both educt (left) and product (right) states for D-I, D-II, Df-OH-III and Df-OH-IV reactions, respectively. The color code is as explained above.

A second possible dissociation reaction is D-II from CUSb to the less favorable CUSb||O- μ_3 :



This reaction is endoenergetic ($\Delta E = 0.59$ eV) and endoergic ($\Delta G = 0.53$ eV). No additional energy barrier could be found although both educt and product are minima. The reaction pathway shows simply an upgoing path in energy without any barrier (see Figure 3.8(b)). Thus, a reaction rate constant based on transition state theory can not be obtained. The molecular minimum is more stable than the dissociated structure on CUSb||O- μ_3 by 0.15 eV.

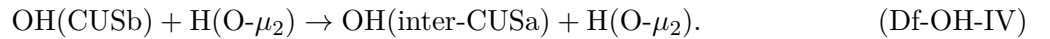
Other dissociated minima can not be reached from the molecular minimum CUSb directly, because both fragments (OH and H) have to move after the dissociation. With the low barrier the dissociation channel to CUSb||O- μ_2 , reaction D-I will clearly dominate those reactions. Starting from the product of D-I, CUSb||O- μ_2 , further diffusion reactions are possible.

The OH diffusion reaction, Df-OH-III, moves from CUSb||O- μ_2 to the inter-CUSb position, which is the third most stable species (see Table 3.2):



In this particular reaction, the OH residue diffuses from a CUSb position into a gap between two CUSb atoms (inter-CUSb position), where there is not much repulsion with neighboring surface oxygen atoms and other CUS atoms nearby during the diffusion, see Figure 3.8(c). The process is slightly endoenergetic/endoergic with ~ 0.2 eV and has a barrier of $\Delta E^\ddagger = 0.35$ eV/ $\Delta G^\ddagger(300\text{ K}) = 0.39$ eV. With the corresponding rate constant of $k(300\text{ K}) = 1.8 \times 10^6\text{ s}^{-1}$, it is relatively fast for OH diffusion reactions compared to the reactions at other alumina surfaces [76, 78].

In contrast to that the real CUS-to-CUS diffusion reaction, Df-OH-IV, is much slower. It is a diffusion of the OH fragment from CUSb to inter-CUSa with the hydrogen residue staying at an O- μ_2 position (see Figure 3.8(d)):



This process is exoenergetic/exergonic because the inter-CUSa||O- μ_2 is 0.22 eV more stable than CUSb||O- μ_2 . However, the barrier of $\Delta G^\ddagger = 1.10$ eV is relatively high and leads to a slow reaction rate constant $k(300\text{ K}) = 2.41 \times 10^{-6}\text{ s}^{-1}$ (slow when compared to Df-OH-III). This is still faster than OH diffusion on the alumina(0001) surface [76, 93] due to high activation barriers, where the rate constant of a comparable CUS-to-CUS diffusion reaction is $k(300\text{ K}) = 4 \times 10^{-45}\text{ s}^{-1}$. For the (1 $\bar{1}$ 02) surface no OH diffusion was calculated, but the

3.3 Dissociation and Diffusion Reactions of Water Species

corresponding H₂O diffusion process has around $k(300\text{ K}) = 1.4 \times 10^{-3}\text{ s}^{-1}$, and a comparable H₂O diffusion process for the (0001) surface has a rate constant of $k(300\text{ K}) = 8 \times 10^{-3}\text{ s}^{-1}$. For the (11 $\bar{2}$ 0) surface no H₂O diffusion reactions can be observed due to the instability of the molecularly adsorbed species which would rather dissociate than diffuse.

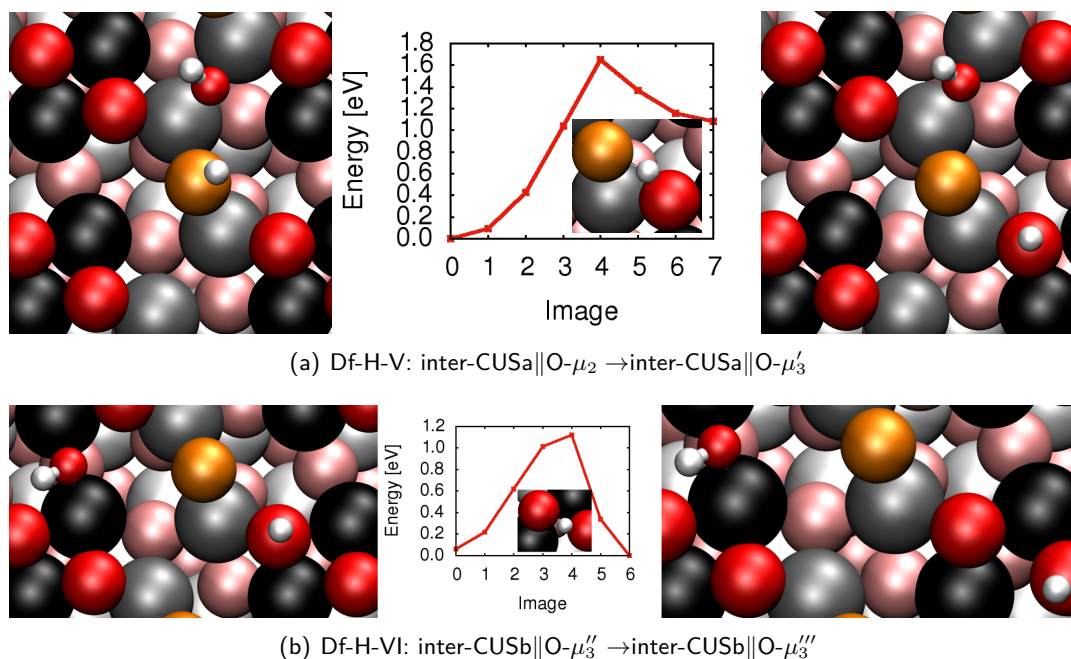
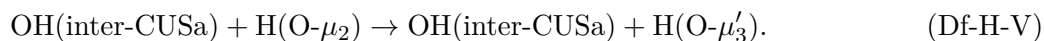


Figure 3.9: Minimum energy paths with transition states, and both educt and product states for Df-H-V and Df-H-VI reactions. The color code is as explained above.

In addition to OH diffusion processes, also diffusion of adsorbed H can be imagined. The different types of surface oxygen atoms and also the distances between OH and H residues can affect the adsorption energy and the relative reaction kinetics. Two of these processes were studied.

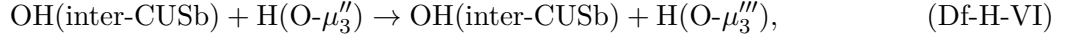
One reaction, called Df-H-V, starting from the most stable inter-CUSa||O- μ_2 with a twofold coordinated oxygen atom to a threefold coordinated oxygen atom can be seen in Figure 3.9(a):



Here, the prime indicates a second next neighbor position rather than a next neighbor adsorbed species. The reaction is significantly endoenergetic/endoergic with a free energy barrier of 1.50 eV, giving a rate constant at 300 K of $4.90 \times 10^{-13}\text{ s}^{-1}$. This process is so unlikely because a less favored O- μ_3 position is occupied and this position is also less stabilized because of the greater distance between OH_{surf} and OH_{ads} groups. In general, reactions that involve an H

atom traveling from an O- μ_2 position to an O- μ_3 position are energetically costly and often show high barriers, making these reactions unmeasurably slow.

The second type of hydrogen diffusion reaction studied is



where H diffuses from an O- μ_3 position to another neighboring O- μ_3 position. Double and triple primes indicate even higher distances between OH and H fragments. The adsorption energies for both educt and product are similar now because the only difference is the distance between fragments. Nevertheless, the free energy barrier of 0.94 eV is quite high and the corresponding rate constant is $k(300 \text{ K}) = 1.1 \times 10^{-3} \text{ s}^{-1}$, see also Figure 3.9(b).

The simulation of all possible reactions forming the complete kinetic network was not possible yet, however, already from the results above the following conclusions can be made: Starting from molecularly adsorbed water, dissociated species can be obtained fast, especially the CUSb||O- μ_2 can be reached easily from the molecular CUSb state.

The other two most stable adsorbed species, inter-CUSa||O- μ_2 and inter-CUSb||O- μ_2 , can be reached at room temperature by OH diffusion reactions from CUSb||O- μ_2 fast (inter-CUSb||O- μ_2) or slow (inter-CUSa||O- μ_2) reactions.

Hydrogen diffusion reactions involving the energetically less stable O- μ_3 sites are typically also kinetically hindered. With this we come to the conclusion that the low-energy dissociated species with protonated O- μ_2 sites will form on the surface in the course of time.

Table 3.6: Energy and free energy differences are given: $\Delta E = E(\text{product}) - E(\text{educt})$, $\Delta E^\ddagger = E^\ddagger - E(\text{educt})$, respective for G . Thermodynamic properties are given at $T = 300 \text{ K}$. k is the rate constant from Equation (1.65). The three types of reactions are dissociation (D), OH diffusion (Df-OH) and H diffusion (Df-H). "n.f." indicates "not found".

Reaction Type		$\Delta E(\text{eV})$	$\Delta G(300 \text{ K})(\text{eV})$	$\Delta E^\ddagger(\text{eV})$	$\Delta G^\ddagger(300 \text{ K})(\text{eV})$	$k(300 \text{ K})(\text{s}^{-1})$
H ₂ O dissociation	D-I	-0.50	-0.52	0.01	0.002	5.76×10^{12}
	D-II	0.59	0.53	n.f.	n.f.	n.f.
OH diffusion	Df-OH-III	0.19	0.22	0.35	0.39	1.88×10^6
	Df-OH-IV	-0.21	-0.13	1.07	1.10	2.41×10^{-6}
H diffusion	Df-H-V	1.08	1.04	1.65	1.49	4.90×10^{-13}
	Df-H-VI	-0.06	-0.07	1.05	0.94	1.05×10^{-3}

As mentioned before a well known problem of GGA is that barriers are underestimated [112]. In fact, as has been shown in Section 2.2.3, for H₂O at the (0001) surface, the use of hybrid functionals/LMP2 is costly but improves the rates towards more realistic orders of magnitude.

3.4 Interpretation of Vibrational Spectra

Vibrational spectroscopy is a great source of knowledge about chemical systems. The frequencies of vibrations give hints about the chemical environment, *e.g.* as hydrogen bonds and other atoms nearby that bind to each other. These vibrational frequencies were calculated for the surface system adsorbed with OD. Our experimental partners from FHI use deuterated water (D_2O) instead of H_2O because the chemical reactivity is the same but the spectroscopic properties are clearer with their applied laser system, so that all results presented in this particular section are given for D_2O . The experimental sum frequency generation spectra (SFG) for the OD range of the low-coverage regime for two different coverages are shown in Figure 3.10 as they were published in [104].

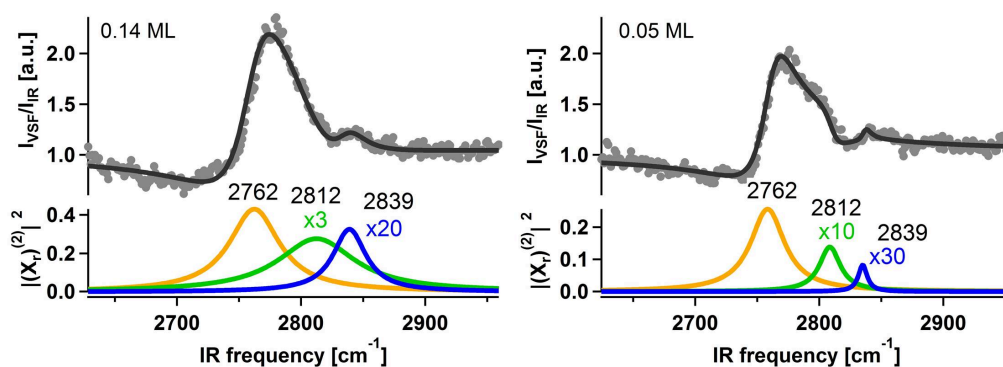


Figure 3.10: Experimental SFG results for $(11\bar{2}0)$ surface with 0.14ML (monolayer, left spectrum) and 0.05ML water coverage (right) including fit (colored lines) according to Reference [104]. Coverage only influences intensity of the peaks but not the peak position itself. The different coverages are achieved via different preparing temperatures of the sample. The y-axis for experimental data points is given as $I_{V_{SF}}/I_{IR}$ (with $V_{SF} = SFG$) to make sure that only the atoms of the interface contribute to the spectrum and for the fitted data we assume that the square of the absolute values of the susceptibility of second order ($|\chi^{(2)}|^2$) is proportional to the SFG intensity [22].

In experiment D_2O was brought onto the $(11\bar{2}0)$ surface with a molecular beam source (MBS). The SFG measurement was then done at 130 K. For further experimental details see [104] and the supporting information therein.

To calculate the vibrational modes in this work mainly two methods were applied: Normal mode analyses and VDOS spectra from AIMD via the velocity-velocity autocorrelation function, see Section 3.4.3.

In Section 3.4.1.1, the focus is mainly on the peak position rather than their intensities, because in the first place it is of greater importance what kind of vibrations gives which peak than the intensity of the peak itself. Also, it is still challenging to determine the frequencies in good comparison with experimental findings before heading to intensities.

Still, intensities for vibrational transitions are also computed. In the normal mode analyses this work follows two distinct approaches to do so: the dipole model and Born effective charges. Also, in the power spectra from MD calculations intensities are retrieved. However, as stated earlier, the VDOS intensities are not directly related to intensities in SFG or IR vibrational spectroscopies, see Section 1.7.

In Subsection 3.4.1, OD stretch vibrations are presented for low-coverage situations (one molecule per (2×2) cell). However, also modes for higher coverage systems will be examined. Further, we will also consider lattice vibrations, which are dominantly of the Al-O type. Intensities in this section are calculated with the dipole model. Subsection 3.4.2 gives the spectra including intensities determined via Born effective charges in comparison to intensities from the dipole model, and in Subsection 3.4.3 the results from the velocity-velocity autocorrelation function are shown.

3.4.1 Vibrational Analysis Based on Normal Modes

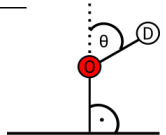
3.4.1.1 Normal Mode Frequencies for OD Vibrations

The normal modes are calculated within the harmonic approximation, using the PBE+D2/PW approach with VASP. We assume that the OD stretching modes for the three most stable dissociated structures (see bold entries in Tables 3.2 and 3.4) would contribute to the spectrum the most, since the less stable adsorbed species are improbable to appear (see discussion about the Boltzmann weight later). The corresponding wavenumbers are presented in Table 3.7 for different slab sizes, as given in Figure 3.2. Also the angle of the OD bond with respect to the surface is given (see Table 3.7), since vibrations which are parallel to the surface cannot be detected with SFG spectroscopy and hence the intensity is a function of this angle.

Following this approach we expect six modes to appear: an OD_{surf} and an OD_{ads} for each of the three, where “ads” corresponds to the O-D bond of the dissociated water, and “surf” to the O-D bond arising from the binding of the dissociated D, to a surface aluminol O atom, as before. In all cases the relationship between the two individual modes for each considered structure is portrayed by $\tilde{\nu}(\text{OD}_{\text{ads}}) > \tilde{\nu}(\text{OD}_{\text{surf}})$. This can be explained with the different reduced mass for both vibrations: The OD_{surf} oscillator has a slightly larger reduced mass since

Table 3.7: Wavenumbers $\tilde{\nu}$ of normal modes for single dissociated D₂O molecules on a α -Al₂O₃(11 $\bar{2}$ 0) (2 × 2) surface for different slab sizes: OD stretching modes for each of the three most stable minima. All values are given in cm⁻¹; in parantheses, the angle of the OD bonding vector to the surface normal (θ in °) is provided. In each column, the left value reflects the adsorbed OD_{ads} group and the right wavenumber the surface OD_{surf} group, respectively. In the sketch the angle θ between the OD bond and the surface normal is shown. Experimental values according to the assignment made in Reference [104].

Layers	inter-CUSa O- μ_2	CUSb O- μ_2	inter-CUSb O- μ_2
10	2731 (44), 2694 (36)	2785 (26), 1711 (61)	2692 (41), 2689 (54)
15	2728 (44), 2695 (36)	2783 (24), 1812 (60)	2711 (34), 2656 (60)
20	2729 (44), 2694 (35)	2783 (24), 1838 (60)	2715 (34), 2665 (58)
25	2728 (44), 2696 (35)	2767 (59), 1750 (62)	2764 (29), 2724 (41)
Exp. [104]	2812, 2762	2839	



the deuterium is bound directly to the surface, whereas the adsorbed OD group can act more as a quasi-free OD group [22]. Assuming the same force constant, we get $\tilde{\nu}(\text{OD}_{\text{ads}}) > \tilde{\nu}(\text{OD}_{\text{surf}})$, as observed. All these vibrations are clearly localized on one of the OD groups. While normal modes of all molecular and next neighbor dissociated structures from 10 to the 25 layer slab model were calculated, we find that the results were already converged to within a few wavenumbers with 10 layers concerning OD stretch frequencies as mentioned above. An exception to this is the dissociated species inter-CUSb||O- μ_2 , which is not as stable and hence not so probable to appear.

To consider the probability of observing the three dissociated species, their respective Boltzmann weights P_i were evaluated,

$$P_i \sim e^{-G_i/(k_B T)} \quad (3.4)$$

with the free energy G_i of Table 3.2. With this analysis it is possible to show the relative population for different temperatures for the three most stable dissociated species, as given in Table 3.8, for the 10 layer case. In the temperature range relevant for the experiments⁵, it is shown that the population of the species inter-CUSa||O- μ_2 clearly dominates and furthermore that the population of inter-CUSb||O- μ_2 is very low compared to the other two.

⁵ Measurements were done at 130 K. Also, the sample is flashed to either 300 K or 400 K during the sample preparation.

Table 3.8: Boltzmann population P relative to the most stable inter-CUSa $\parallel\text{O}-\mu_2$, calculated according to Equation (3.4) for 130, 300 and 400 K. Values are given for the 10 layer system.

	P_{130K}	P_{300K}	P_{400K}
inter-CUSa $\parallel\text{O}-\mu_2$	1	1	1
CUSb $\parallel\text{O}-\mu_2$	1.4×10^{-6}	6.1×10^{-3}	3.2×10^{-2}
inter-CUSb $\parallel\text{O}-\mu_2$	1.0×10^{-15}	1.2×10^{-6}	6.6×10^{-5}

For these two most stable structures, we expect four relevant modes to be seen in a spectrum. For the 10 layer slab, there would be signals at 2731, 2694, 2785 and 1711 cm^{-1} , respectively, according to Table 3.7. One of them is noticeably lower in energy due to hydrogen bonding (OD_{surf} vibration of CUSb $\parallel\text{O}-\mu_2$ at 1711 cm^{-1}). Also the angle of the corresponding bonding vector with respect to the surface normal is very high in this case (61°), so that the expected intensity is remarkably lower and may be not visible in experiment because the intensity of the SFG decreases rapidly with increasing angle [22].

With this in mind, we expect three visible peaks, which fits well to the experimental results shown in Figure 3.10. Similar to existing literature for other surface cuts [22], absolute theoretical wavenumbers (2731, 2694, 2785 cm^{-1} , harmonic, unscaled) are only in rough agreement with experiment (2762, 2812, 2839), showing a redshift in the order of 60-70 cm^{-1} for the former. However, relative wavenumbers are in reasonable agreement, see results for experiment and all different sized slabs in Table 3.9.

Table 3.9: Wavenumber differences $\Delta\tilde{\nu}$ are given in [cm^{-1}]. $\Delta\tilde{\nu}_1$ is the difference between the surface OD group of the inter-CUSa $\parallel\text{O}-\mu_2$ species and the respective surface OD group on $\text{O}-\mu_2$ and $\Delta\tilde{\nu}_2$ is the difference between the same surface OD group and the adsorbed OD group on CUSb from CUSb $\parallel\text{O}-\mu_2$.

layers	$\Delta\tilde{\nu}_1$	$\Delta\tilde{\nu}_2$
10	37	91
15	33	88
20	35	89
25	32	71
exp.	50	77

3.4.1.2 Normal Mode Frequencies and Anharmonic Corrections for an Atom Centered Basis

Analogous to the AO basis calculations for the (0001) surface in Section 2.2.2, the most stable adsorbed species at the (11 $\bar{2}$ 0) surface were also reoptimized with PBE+D3 and B3LYP+D3 (with AO basis set 7 from Table 2.2), respectively, and the corresponding vibrational frequencies were evaluated, using CRYSTAL. These results are shown in Table 3.10. Similar to the

Table 3.10: Stretch wavenumbers $\tilde{\nu}$ for both types of the OD groups at the (11 $\bar{2}$ 0) surface for the three most stable species (10 layer slab). Frequencies were calculated with CRYSTAL at the B3LYP+D3 and PBE+D3 level of theory with basis set 7, wavenumbers including anharmonic corrections $\tilde{\nu}_{\text{anh}}$ are also given. VASP results were obtained with a plane wave basis and PBE+D2, see Subsection 3.4.1.1. The abbreviations stand for: iCa2=inter-CUSa||O- μ_2 , Cb2=CUSb||O- μ_2 and iCb2=inter-CUSb||O- μ_2 .

stretch	PBE+D3/AO		B3LYP+D3/AO		PBE+D2/PW	Exp. [104]
	$\tilde{\nu}$ [cm $^{-1}$]	$\tilde{\nu}_{\text{anh}}$ [cm $^{-1}$]	$\tilde{\nu}$ [cm $^{-1}$]	$\tilde{\nu}_{\text{anh}}$ [cm $^{-1}$]	$\tilde{\nu}$ [cm $^{-1}$]	$\tilde{\nu}$ [cm $^{-1}$]
iCa2: OD $_{\text{surf}}$	2682	2599	2773	2695	2694	2762
iCa2: OD $_{\text{ads}}$	2728	2644	2811	2729	2731	2812
Cb2: OD $_{\text{surf}}$	1658	1310	2019	1722	1711	-
Cb2: OD $_{\text{ads}}$	2769	2687	2843	2765	2785	2839
iCb2: OD $_{\text{surf}}$	2657	2569	2778	2694	2689	-
iCb2: OD $_{\text{ads}}$	2688	2595	2777	2689	2692	-

results for the (0001) surface cut, the PBE+D2/D3 results for both plane wave and AO basis are in good agreement and B3LYP+D3 vibrations are higher in energy. Anharmonic corrections deliver lower energy modes, so that B3LYP+D3 including anharmonic corrections is again in the same range as the PBE+D3 results without anharmonic corrections. As mentioned above, in the experiments [104] three peaks were assigned to both OD groups of inter-CUSa||O- μ_2 and the OD $_{\text{ads}}$ group of CUSb||O- μ_2 . The corresponding wavenumbers are 2762, 2812 and 2839 cm $^{-1}$. Differences between the highest-energy and respective peaks, analogous to Table 2.8, are shown in Table 3.11.

Comparing the experimental wavenumbers to PBE+D2/PW results and PBE+D3/AO, these experimental wavenumbers are shifted by around 50-80 cm $^{-1}$ which is significantly better than for the (0001) surface (also compare to Tables 2.8 and 3.9). With anharmonic corrections, the wavenumbers are shifted towards lower wavenumbers, which worsens the agreement to experiment. Only the B3LYP+D3 results agree very well with deviations of one to eleven wavenumbers in the absolute numbers, which is an astonishingly well compliance. One has to

Table 3.11: Vibrational frequency differences $\Delta\tilde{\nu}$ of the results presented in Table 3.10 with respect to the highest energy mode, Cb2: OD_{ads}. $\Delta\tilde{\nu}_1$ refers to the difference OD_{ads}(inter-CUSa||O- μ_2)–OD_{surf}(inter-CUSa||O- μ_2) and $\Delta\tilde{\nu}_2$ =OD_{ads}(CUSb||O- μ_2)–OD_{surf}(inter-CUSa||O- μ_2), as in Table 3.9. All values are given in cm⁻¹.

resonances	PBE+D3/AO		B3LYP+D3/AO		PBE+D2/PW	Exp. [104]
	$\Delta\tilde{\nu}$	$\Delta\tilde{\nu}_{\text{anh}}$	$\Delta\tilde{\nu}$	$\Delta\tilde{\nu}_{\text{anh}}$	$\Delta\tilde{\nu}$	$\Delta\tilde{\nu}$
$\Delta\tilde{\nu}_1$	46	45	38	34	37	50
$\Delta\tilde{\nu}_2$	87	88	70	70	91	77

mention that the influence of the basis set is strong and larger basis sets were not feasible due to high computational costs. As shown before, anharmonic corrections shift the results to lower wavenumbers and decrease the overall agreement. With the computational power available during this work, B3LYP+D3/AO seems by far the best choice for reproducing experimental vibrations⁶.

3.4.1.3 Harmonic Vibrational Spectra from the Dipole Model

In the following, vibrational spectra in the harmonic approximation in the form of stick spectra will be shown for the OD region (1650-3000 cm⁻¹) and also for the low-frequency, lattice vibrational (mainly Al-O vibrations) region (0-1000 cm⁻¹). (All calculations are based on PBE+D2/PW calculations in this subsection.) We begin with the latter, and we compute spectra without and with water in this case. All spectra shown in this section were normalized to the most intense peak, with the intensities being determined by the dipole model introduced in Section 1.7. In some figures short notations for the adsorbed species are used: iCa2 for inter-CUSa||O- μ_2 , Cb2 for CUSb||O- μ_2 and iCb2 for inter-CUSb||O- μ_2 . Unfortunately, not for all coverages experimental results for the spectral range of the lattice vibrations are obtained by our experimental partners yet, so that only the clean and the fully covered surface can be compared to SFG spectra.

In contrast to OD vibrations, for the lattice Al-O vibrations we need to consider many layers of the bulk in order to get more reliable results [77]. Therefore, we performed calculations for the most stable adsorption geometries for more layered systems, up to 30 atomic layers, for the clean surface, and for up to 25 layers for the adsorbate covered surface as before.

⁶ Applying the scaling factors from Reference [101] again, gives improved results for PBE+D3/AO really close to experimental values, whereas B3LYP+D3/AO, which showed by itself excellent agreement with experimental results, is slightly too high with the scaling compared to experiment. PBE+D2/PW wavenumbers also improve strongly with the respective scaling.

Vibrational spectra for the clean surface in the Al-O lattice regime are shown in Figure 3.11(a). For differently sized slabs, the results differ largely. Especially the 10 layer system is shifted strongly to lower frequencies/wavenumbers compared to the other slab sizes. From Table 3.12 it can be concluded that the most intense peak is shifted to higher wavenumbers with increasing slab size. This demonstrates that in contrast to the OD vibrations (see below), the lattice vibrations are largely dependent on slab size. Two major conclusions can be drawn: (1) the intense peaks within the dipole model are at high frequencies, the lower wavenumbers are less intense. (2) The most intense peak is shifted with growing slab size and converges to $\sim 850 \text{ cm}^{-1}$.

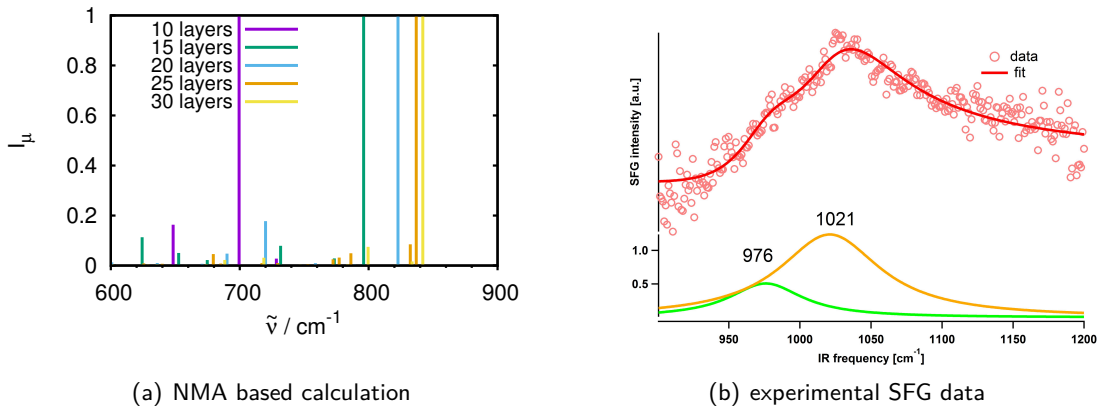


Figure 3.11: (a) Comparison of vibrational spectra for different slab sizes from 10 to 30 layers for the clean $(11\bar{2}0)$ (2×2) surface obtained with normal mode analyses and intensities from the dipole model. For each layer thickness, the highest intensity peak is normalized to 1. (b) Experimental SFG spectra by the group of K. Campen (FHI) for the clean $(11\bar{2}0)$ surface, red circles show data, red line is a fit of these data points and the green and yellow lines are the peaks that are obtained by analyzing the data with a fitting procedure.

For the clean surface, the experimental data (see Figure 3.11(b)) reveal two broad peaks, one at 976 and the other at 1021 cm^{-1} . With the 30 layer model, we obtain respective peaks at 800, 834 (with low intensity) and 842 cm^{-1} , which is redshifted to experimental results by 176, 187 and 180 cm^{-1} , respectively. As for the OD stretch vibrations, the absolute comparison is not good, but the difference between those peaks is well described: for the experiment $\Delta\tilde{\nu} = 45 \text{ cm}^{-1}$ and for the 30 layer model $\Delta\tilde{\nu} = 34/42 \text{ cm}^{-1}$. Also for the 25 layer model we observe 46 and 51 cm^{-1} differences, which is in good agreement.

While the trend of higher wavenumbers with increasing slab size is true for the clean surface and the lattice region of the covered systems, it does not hold for the OD vibrations regime. As already mentioned, the OD frequencies are more or less converged for the 10 layer slab.

Table 3.12: Comparison of results for the different slab sizes with NMA: three most intense peaks $\tilde{\nu}_{max}$ from the dipole model of the vibrational spectrum for the clean surface. All values are given in cm^{-1} . The Δ are defined as follows: $\Delta\tilde{\nu}_1 = \tilde{\nu}_{max1} - \tilde{\nu}_{max2}$, $\Delta\tilde{\nu}_2 = \tilde{\nu}_{max1} - \tilde{\nu}_{max3}$ and $\Delta\tilde{\nu}_3 = \tilde{\nu}_{max2} - \tilde{\nu}_{max3}$. The value from the SFG experiment is $\Delta\tilde{\nu}_{exp} = 45 \text{ cm}^{-1}$.

Layers	10	15	20	25	30
$\tilde{\nu}_{max1}$	700	796	823	837	842
$\tilde{\nu}_{max2}$	648	773	720	832	834
$\tilde{\nu}_{max3}$	552	732	690	786	800
$\Delta\tilde{\nu}_1$	52	23	103	5	8
$\Delta\tilde{\nu}_2$	148	64	133	51	42
$\Delta\tilde{\nu}_3$	96	41	30	46	34

In fact, when comparing OD spectra with the dipole model, we see again that the frequencies show no marked differences, for more than 10 layers, relative to the 10 layer case, according to Figure 3.12(a) and (b), exemplarily for the dissociated species inter-CUSa||O- μ_2 . In contrast, the low-frequency part in the full spectra which are also shown in the figures, change clearly.

All of the results so far were for the low-coverage case, *i.e.* one (dissociated) water per (2×2) cell. The influence of higher coverage on adsorption energies was examined already in Section 3.2. There coverages with $2\text{D}_2\text{O}$, four and twelve water molecules per (2×2) cell were considered, the latter corresponding to 1ML. Now we also study the influence of higher coverages on OD frequencies and vibrational spectra. The spectra for coverages of $1/6$ (2 molecules per (2×2) supercell) and $1/3$ (4 molecules), as well as vibrational spectra for the O-II termination can be found in Appendix E. For the 1ML system, harmonic vibrational frequencies in comparison to experimental SFG data is shown here.

The 1ML system consists of a complex mixture of twelve adsorbed OD residues (on CUSb, inter-CUSa and inter-CUSb), as well as twelve surface OD groups on O- μ_2 but also the less favorable threefold coordinated O- μ_3 (see Figure 3.6(b)). Due to the quite different species, the system possesses many peaks in the OD region, see Figure 3.13(b)-(c). Hydrogen bonding and interaction between groups shift many of the peaks, compared to the singly adsorbed species. Below 900 cm^{-1} , delocalized OD and lattice vibrations can be found (panel (a)). In the region between 872 and 1117 cm^{-1} (shown in Figure 3.13(b)), there are bending-like vibrations mostly of O- $\mu_2\text{D}$ groups. From ≈ 2000 to 2740 cm^{-1} , various OD stretch vibrations occur. These are split into three distinct regions: From $\approx 2000\text{-}2220 \text{ cm}^{-1}$ in plane vibrations of strongly hydrogen-bonded species can be found. From $2400\text{-}2450 \text{ cm}^{-1}$ in plane vibrations of non hydrogen-bonded species occur and above 2550 cm^{-1} out of plane OD stretching bonds appear. Also for this system an experimental SFG spectrum was obtained (only for the lattice

3.4 Interpretation of Vibrational Spectra

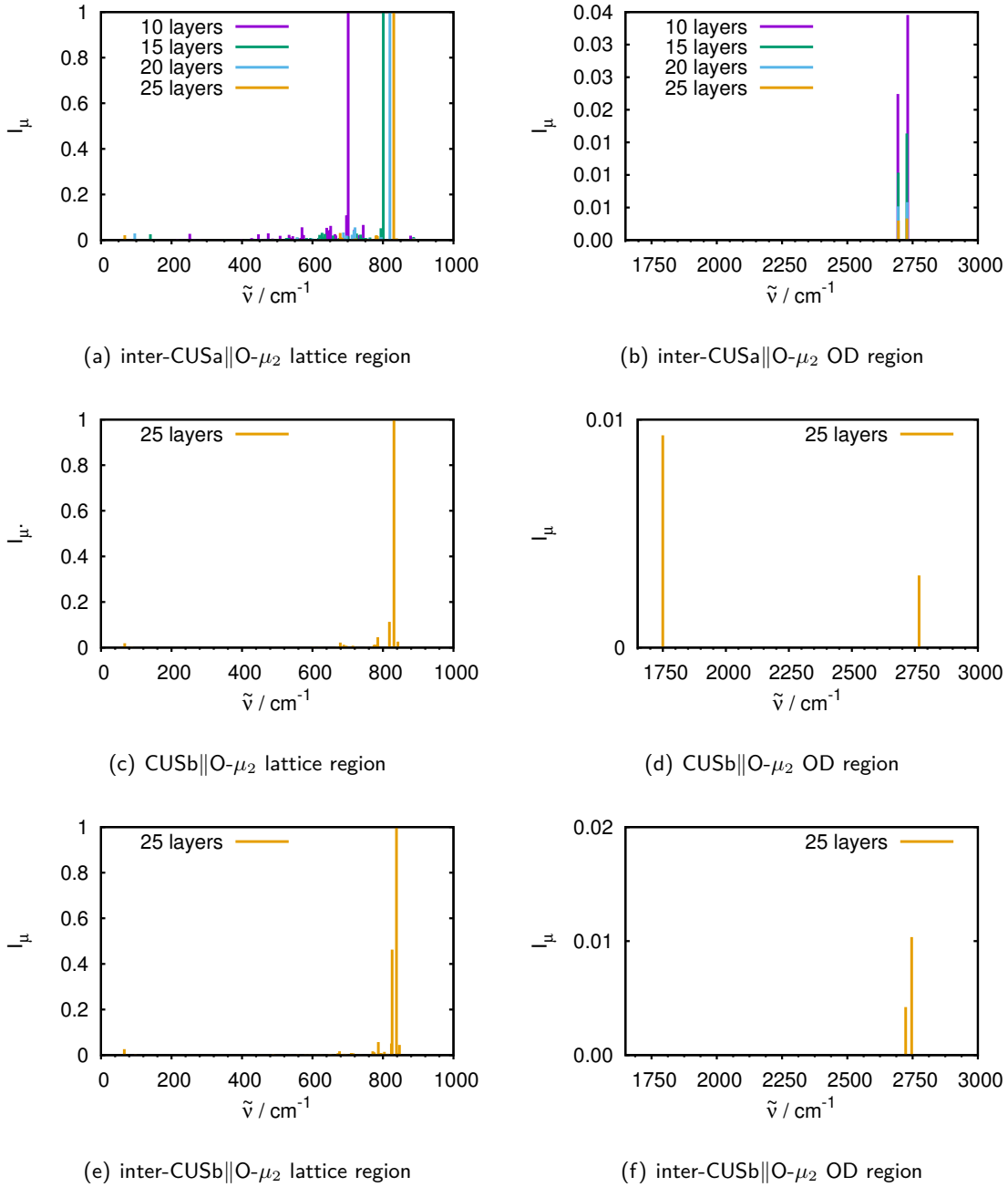


Figure 3.12: Comparison of inter-CUSa||O- μ_2 , CUSb||O- μ_2 and inter-CUSb||O- μ_2 frequencies and intensities for the 25 layer slab, obtained by normal mode analyses with intensities from the dipole model. For inter-CUSa||O- μ_2 also spectra for slab sizes from 10 to 25 are shown for comparison. All peaks were normalized to the most intense peak.

3 Water on $\alpha\text{-Al}_2\text{O}_3(11\bar{2}0)$

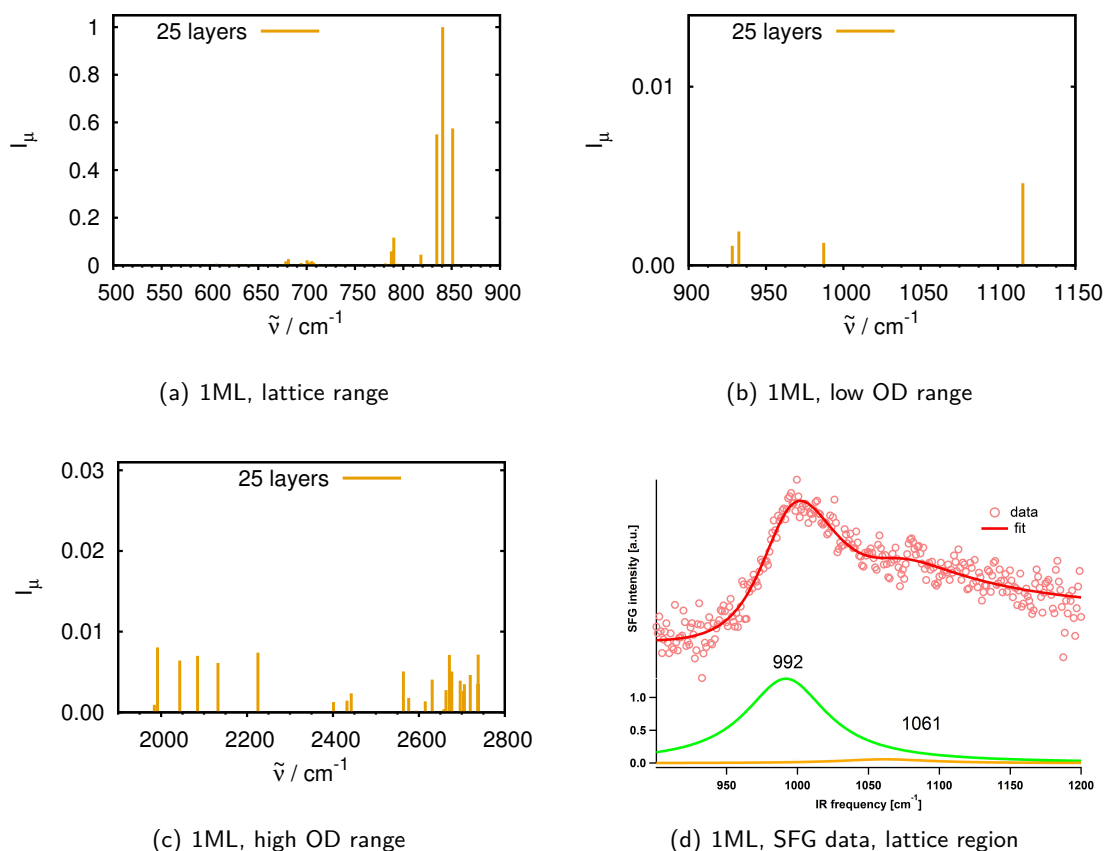


Figure 3.13: Comparison of stick spectra in the dipole model of the fully D_2O covered surface (1ML, twelve molecules). Shown is the spectrum for the 25 layer slab for (a) the lattice region, (b) the low energy OD range with bending-like vibrations and (c) the high energy OD range. The omitted regions do not contain peaks. The spectrum is normalized to one concerning the most intense peak. (c) Data of experimental SFG spectroscopy by the group of K. Campen (FHI) for the lattice region of the $(11\bar{2}0)$ surface with 1ML water coverage including fit (colored lines) as in Figure 3.11.

region, see Figure 3.13(d)). In the lattice region two peaks are found, one at 992 and the other at 1061 cm^{-1} giving a difference of $\Delta\tilde{\nu} = 69\text{ cm}^{-1}$. The calculation with 25 layers gives the corresponding peaks at 790 and 851 cm^{-1} with a $\Delta\tilde{\nu} = 61\text{ cm}^{-1}$. The wavenumbers are redshifted by circa 200 cm^{-1} compared to experiment but it is expected that low energy modes are in worse agreement than OD stretch modes. However, the agreement in relative numbers is good.

3.4.2 Harmonic Vibrational Spectra from Born Effective Charges

As a second method to obtain vibrational intensities, Born effective charges were evaluated, again with frequencies obtained within the harmonic approximation on the PBE+D2/PW level. Spectra were calculated for the three most stable adsorbed, dissociated species inter-CUSa||O- μ_2 , CUSb||O- μ_2 and inter-CUSb||O- μ_2 of α -Al₂O₃(11 $\bar{2}$ 0) with one D₂O per (2 × 2) cell, using the 10 layer slab model. For getting the spectrum an angle of the IR beam of 45° was assumed. This choice of this angle weights the elements (x , y and z) of the Born effective charge matrix in Equation (1.60) that are in the sum of the intensity, see Section 1.7. Since both the dipole model intensities and the BEC calculations are based on normal modes, the frequencies are equal and only the intensities can differ.

In Figure 3.14 a comparison of NMA spectra with BEC and dipole model intensities is given.

For inter-CUSa||O- μ_2 , the intensities in the OD range are nearly the same, although the peaks with the higher intensity changed (Figure 3.14(b)). In the lattice region the agreement is not good at all, see Figure 3.14(a). For the OD region of CUSb||O- μ_2 , the agreement is worse between BEC and the dipole model intensities, BEC predicts the H-bonded peak at 1711 cm⁻¹ to be the most intense whereas in the dipole model the most intense peak is in the lattice region, *cf.* Figures 3.14(c) and (d). Concerning the inter-CUSb||O- μ_2 , the OD region shows good agreement between BEC and dipole model (Figure 3.14(f)). Also the most intense peak is from the same vibration. Again in the lattice region, the difference is larger, see Figure 3.14(e).

In Table 3.13, a comparison between dipole and BEC intensities of the OD stretch vibrations can be found. The results are in reasonable agreement for inter-CUSa||O- μ_2 and inter-CUSb||O-

Table 3.13: Comparison of the intensities for the 10 layer system of D₂O/Al₂O₃(11 $\bar{2}$ 0) obtained from the dipole model and from the Born effective charges based approach. They were normalized to the most intense peak within the full frequency range, to make a reasonable comparison.

	vibration	$\tilde{\nu}$ [cm ⁻¹]	Intensity	
			dipole model	BEC
inter-CUSa O- μ_2	OD _{ads}	2731	0.034	0.023
	OD _{surf}	2694	0.022	0.029
CUSb O- μ_2	OD _{ads}	2785	0.262	0.038
	OD _{surf}	1711	0.155	1.000
inter-CUSb O- μ_2	OD _{ads}	2692	0.007	0.013
	OD _{surf}	2689	0.060	0.072

μ_2 , but deviate largely for the hydrogen-bonded CUSb||O- μ_2 system. The overall agreement of the inter-CUSa||O- μ_2 spectra is very good. Only the most intense peak in the lattice region

3 Water on $\alpha\text{-Al}_2\text{O}_3(11\bar{2}0)$

diverges by 27 cm^{-1} . For the other two species the agreement is mediocre, especially in the

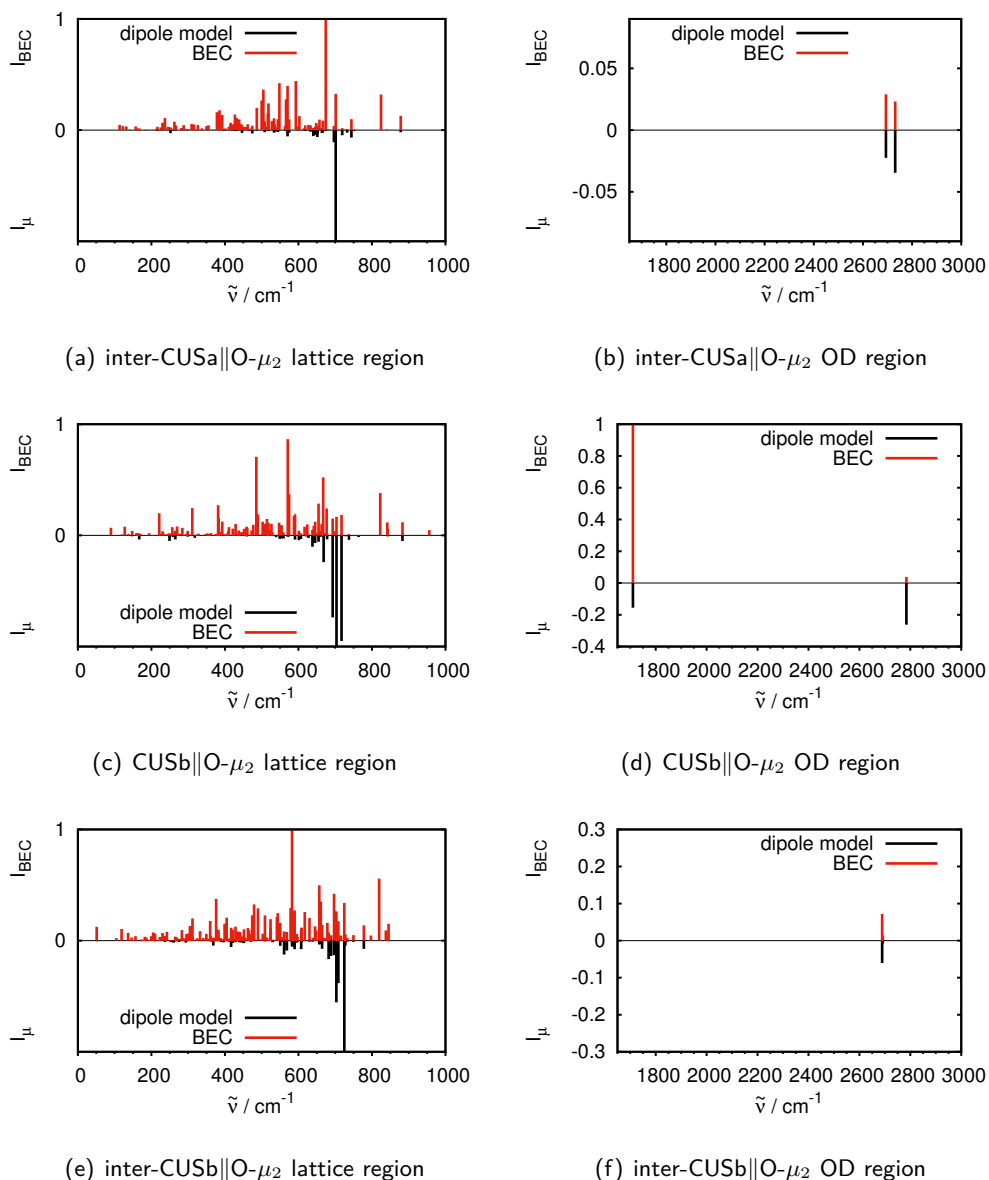


Figure 3.14: Comparison of intensities for the three most stable adsorbed species for intensities from dipole model (black) and from Born effective charges (red). Negative and positive values have no physical meaning and have been chosen to enable better comparison between both intensity models. All spectra were obtained for the 10 layer system and the highest peaks normalized to one. The lattice region is shown from 0 to 1000 cm^{-1} and the OD region from 1650 to 3000 cm^{-1} .

lattice region, where the most intense BEC peak is more in the blue region compared to the peak

from dipole corrected intensities. It is about 30 cm^{-1} for the most intense peak in the lattice region of $\text{CUSb}\|\text{O}-\mu_2$ and around 40 cm^{-1} for the corresponding peaks in $\text{inter-CUSb}\|\text{O}-\mu_2$.

3.4.3 Vibrational Analysis Based on Vibrational Density of States Curves

To go beyond the harmonic approximation, we use vibrational density of state curves obtained from AIMD simulations (Section 1.7). The velocity-velocity autocorrelation function is evaluated from AIMD calculations and Fourier transformed to get information from the time to the frequency domain. This is a radically different ansatz to calculating a spectrum, which gives besides frequencies also intensities and broadened signals. The intensities cannot be directly related to IR or SFG intensities as outlined earlier, however, they are often similar to them [60]. The widths of VDOS curves arise from atomic motion at finite temperature. Respective AIMD trajectories were calculated at 300 K for the clean surface (30 layers), and the three most stable adsorbed structures ($\text{inter-CUSa}\|\text{O}-\mu_2$, $\text{CUSb}\|\text{O}-\mu_2$ and $\text{inter-CUSb}\|\text{O}-\mu_2$, 10 layer model in each case), starting from the minimum structures. For the clean surface the propagation time was 5 ps (with a time step of 1 fs) with the first three ps being equilibration time and the last 2 ps being used for evaluating the spectrum. Similar, for the systems with adsorbed water, around 3.7 ps were simulated (time step of 0.2 fs) and the last 2 ps were used for obtaining the VDOS. Also in all cases a Hann window function was applied [113] to gain better smoothness, but which does not affect the peak positions. The presented spectra are merely preliminary results, since the propagation duration is substantially too short and only one trajectory per system was simulated due to computational costs, so that one cannot rule out the possibility that the system is not converged properly. Usually, for a converged study, for several trajectories and a preequilibration phase of several ps is assumed and afterwards the production run is up to 100 ps or even more, but these results still give a good first glimpse to what the spectrum could look like.

For the clean surface, as for the normal mode results, all peaks are below 900 cm^{-1} , see Figure 3.15 (red line). The most prominent peak in the power spectrum can be observed at significantly lower energy than for any normal mode based result. Also more peaks are present in the whole range from 0 to around 900 cm^{-1} . Compared to the stick spectrum from NMA with intensities from the dipole model also shown in Figure 3.15 (black line), there is no good agreement.

For the water adsorbed surface systems, results are shown in Figure 3.16. The system $\text{inter-CUSa}\|\text{O}-\mu_2$ was propagated for 3.68 ps. The respective spectrum is shown in Figure 3.16(a)

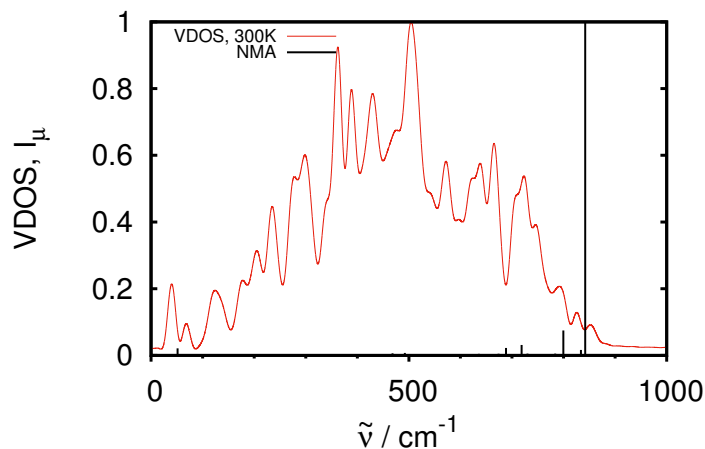


Figure 3.15: VDOS curve of the clean surface of the 30 layer slab, calculated from velocity-velocity autocorrelation function for the last 2 ps of a canonical (NVT) AIMD trajectory at 300 K (in total 5000 steps, 5 ps). In addition to the VDOS, the stick spectrum with intensities from the dipole model based on normal modes for the 30 layer slab is shown in black. Both spectra are normalized to the highest peak.

and shows two prominent peaks in the OD region at 2691 and 2726 cm^{-1} . These two fit very well to the peaks in the normal mode calculations at 2694 and 2731 cm^{-1} . In the lattice region, as it could be observed for the clean surface as well, the eminent peaks of the VDOS spectrum are at lower wavenumbers and there is no strong agreement.

The spectrum of the CUSb||O- μ_2 system can be seen in Figure 3.16(b). It was propagated for 3.67 ps. The OD range shows one clear peak at around 2757 cm^{-1} , which likely corresponds to the non-hydrogen-bonded peak at 2785 cm^{-1} in the normal modes. In contrast to that, the hydrogen-bonded peak which can be found in the normal modes calculation at 1711 cm^{-1} is given in the power spectrum as a multitude of small peaks smeared in the region between 1300 and 2100 cm^{-1} , indicating delocalization between the O_{ads} and O_{surf}. In the lattice region the prominent peaks are distributed wider and also the most prominent peak of the lattice region is at a higher energy than the normal modes suggest. It is unclear whether this description or the normal modes results are closer to the experiment, or if the difference is an artifact which could be overcome by more complete statistics.

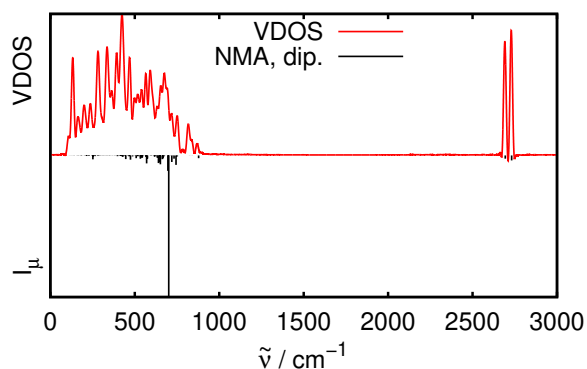
For the inter-CUSb||O- μ_2 species with a trajectory duration of about 3.68 ps, the OD region is in very good agreement with the normal mode results (see Figure 3.16(c)). Compared to the normal modes, where we observe two peaks, there is one broad peak around 2694 cm^{-1} covering both peaks from the normal modes (2689 and 2692 cm^{-1}). It is possible that both groups

3.4 Interpretation of Vibrational Spectra

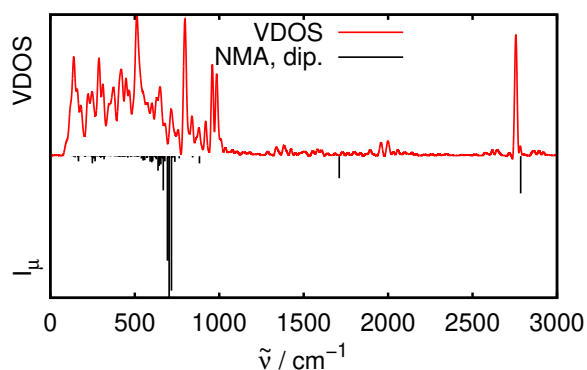
overlap and lead to the broad peak. Also in the lattice region there is good compliance, the most prominent peaks are only separated by 20 cm^{-1} which is the best result for the computed systems.

Although these results are only preliminary, the agreement with normal mode results is very good and gives hope for even more accurate results with longer propagation duration which have not been accomplished yet due to high computational costs.

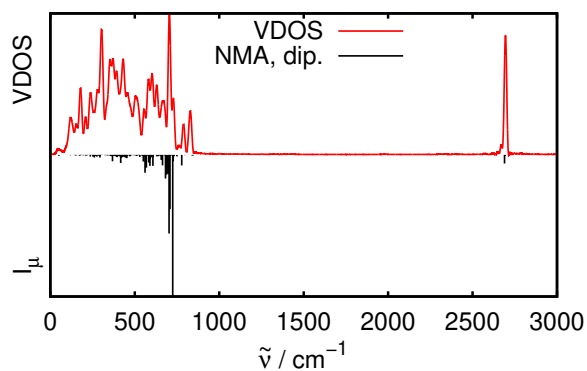
In contrast to normal mode analyses, the VDOS spectra contain anharmonicities, which red-shift the spectrum as expected. For the case of OD vibrations, the shift is up to approximately 10 cm^{-1} , whereas with the anharmonic corrections to normal modes (see Table 3.10) the peaks are shifted by $\approx 100 \text{ cm}^{-1}$. This can be explained when considering, that AIMD mostly probes the harmonic range close to the minimum on the potential energy surface, where the harmonic approximation is still valid.



(a) inter-CUSa||O- μ_2



(b) CUSb||O- μ_2



(c) inter-CUSb||O- μ_2

Figure 3.16: VDOS curves are shown in red, obtained from NVT AIMD trajectories at 300 K, obtained via velocity-velocity autocorrelation functions for the systems inter-CUSa||O- μ_2 (a), CUS||O- μ_2 (b) and inter-CUSb||O- μ_2 (c). Duration of the trajectories is 3.68 ps for inter-CUSa||O- μ_2 , 3.67 ps for CUSb||O- μ_2 and 3.68 ps for inter-CUSb||O- μ_2 , but for the spectra shown, only the last 2 ps were studied for the VDOS. In black the spectrum with intensities (I_μ) from the dipole model based on normal modes is shown below (10 layer slab). For each spectrum, the peaks were normalized to the highest peaks.

Summary

The (0001) surface of α -Al₂O₃ is the most stable surface cut under UHV conditions and was studied by many groups both theoretically and experimentally. Reaction barriers computed with GGA functionals are known to be underestimated. Based on an example reaction at the (0001) surface, this work seeks to improve this rate by applying a hybrid functional method and perturbation theory (LMP2) with an atomic orbital basis, rather than a plane wave basis. In addition to activation barriers, we calculate the stability and vibrational frequencies of water on the surface. Adsorption energies were compared to PW calculations and confirmed PBE+D2/PW stability results. Especially the vibrational frequencies with the B3LYP hybrid functional that have been calculated for the (0001) surface are in good agreement with experimental findings. Concerning the barriers and the reaction rate constant, the expectations are fully met. It could be shown that recalculation of the transition state leads to an increased barrier, and a decreased rate constant when hybrid functionals or LMP2 are applied.

Furthermore, the molecular beam scattering of water on (0001) surface was studied. In a previous work by Hass the dissociation was studied by AIMD of molecularly adsorbed water, referring to an equilibrium situation. The experimental method to obtaining this is pinhole dosing. In contrast to this earlier work, the dissociation process of heavy water that is brought onto the surface from a molecular beam source was modeled in this work by periodic *ab initio* molecular dynamics simulations. This experimental method results in a non-equilibrium situation. The calculations with different surface and beam models allow us to understand the results of the non-equilibrium situation better. In contrast to a more equilibrium situation with pinhole dosing, this gives an increase in the dissociation probability, which could be explained and also understood mechanistically by those calculations.

In this work good progress was made in understanding the (11 $\bar{2}$ 0) surface of α -Al₂O₃ in contact with water in the low-coverage regime. This surface cut is the third most stable one under UHV conditions and has not been studied to a great extent yet. After optimization of the clean, defect free surface, the stability of different adsorbed species could be classified. One

Summary

molecular minimum and several dissociated species could be detected. Starting from these, reaction rates for various surface reactions were evaluated. A dissociation reaction was shown to be very fast because the molecular minimum is relatively unstable, whereas diffusion reactions cover a wider range from fast to slow. In general, the $(11\bar{2}0)$ surface appears to be much more reactive against water than the (0001) surface. In addition to reactivity, harmonic vibrational frequencies were determined for comparison with the findings of the experimental “Interfacial Molecular Spectroscopy” group from Fritz-Haber institute in Berlin. Especially the vibrational frequencies of OD species could be assigned to vibrations from experimental SFG spectra with very good agreement. Also, lattice vibrations were studied in close collaboration with the experimental partners. They perform SFG spectra at very low frequencies to get deep into the lattice vibration region. Correspondingly, a bigger slab model with greater expansion perpendicular to the surface was applied, considering more layers in the bulk. Also with the lattice vibrations we could obtain reasonably good agreement in terms of energy differences between the peaks.

Acknowledgment

I want to thank my doctoral supervisor Prof. Dr. Saalfrank for giving me the scientific opportunity to research on surface systems and all the valuable discussions and advice. Also I am deeply grateful to my supervisor Dr. Jonas Wirth who gave me support during my time starting as a Bachelor's student, during my Master's thesis and also through the beginning of my PhD. Thanks to PD Dr. Tillmann Klamroth for discussions about programming and millions of theoretical questions that arose during the work, Dr. Radosław Włodarczyk for his endless knowledge with VASP and programming in general, Giacomo Melani (soon to be Dr.) for his advice and help, and also the discussions about our teaching duties in mathematics. Thanks to the whole workgroup for all the valuable discussions and the help. For the great atmosphere that was sometimes productive and sometimes also just relaxing and felt comforting, here especially Clemens Rietze, Robert Scholz, Dr. Jan Götze, Dr. Gereon Floss, Florian Bedurke and Steven Lindner contributed. Also I want to thank my second supervisor Prof. Dr. Beate Paulus for discussion and help beyond research topics. Great acknowledgment goes to my experimental cooperation partners from FHI, Yanhua Yue, Dr. Harald Kirsch and Dr. R. Kramer Campen for the great work and publications we did together. Thanks to Dr. Denis Usvyat for all his patience and knowledge and valuable discussions about CRYSTAL/CRYSCOR who often answered my questions from his phone during his vacations. I want to thank Dr. Jean Christophe Tremblay who brought me to theoretical chemistry by bringing my attention to this field of science. Christiane Wunderlich who was my school teacher in chemistry, without whom I would not have studied chemistry.

Appendix

A Special Basis Sets for AO Calculations with CRYSTAL

The customized basis sets 8 and 9 from Section 2.2, containing high angular momentum basis functions were not standard basis sets from the basis set library of CRYSTAL but constructed by Dr. Denis Usvyat, HU Berlin. For Al, s- and p-AOs from *Al_m-6-311G(d)_Heyd_2005* [96,97], d-AOs from *Al_s8511p511d11_Heifets_2013* [94] and f-AOs with a standard exponent of 0.6 were used. (The nomenclature is from the CRYSTAL basis set data base). For O, s-, p- and d-AOs from *O_8411(d11)_Heifets_2013* [94] plus f-AOs from cc-pVTZ were considered. For H s from *H_pob_TZVP* [95] plus p and d from cc-pVTZ (from [114] as implemented in CRYSTAL) were utilized.

In addition, for the dual basis (basis set 9) of O, further the d- and f- diffuse orbitals from aug-cc-pVTZ were added, for Al, also diffuse d- and f-AOs with exponents of 0.12 and 0.2 were added, respectively (as 1/4 and 1/3 of the exponents of the most diffuse d- and f-AOs in the non-dual basis).

The basis set is given in CRYSTAL format below. The first line contains the atomic number (13 for Al, 8 for O and 1 for H) and the number of shells. The following lines contain the specification for each shell. The leading 0 means that the basis is give explicitly, the second number gives the type of the shell (0 - s, 1 - sp, 2 - p, 3 - d, 4 - f). The third number gives the number of primitive Gaussian type orbitals (GTO) that were used to build this shell. The fourth number gives formally the number of electrons in this shell. The last number is a scaling factor that is used to scale the following exponents.

The following indented lines give the exponents and contraction coefficients.

For basis set 8, we have 39 AOs for Al, 30 for O and 14 AOs for H, which makes a total of 2016 basis functions for the (2×2) cell without water and 2074 basis functions for the cell with one water molecule For basis set 9, we have 51 AOs for Al, 42 AOs for O and 14 AOs for H, giving in total 2736 basis functions for the (2×2) cell without water and 2806 basis functions for the supercell with one adsorbed water. Similarly, we have for the other basis sets:

Appendix

Table A.1: Number of AOs for basis sets from Table 2.2. The basis sets are numbered corresponding to their size. Note, e.g. for bases 6 and 7, that a larger basis might have less AOs but have higher exponents for diffuse functions.

basis	Al	O	H
1	18	18	6
2	15	18	6
3	18	18	6
4	18	18	6
5	23	23	6
6	27	18	6
7	22	18	6
8	39	30	14
9	51	42	14

Basis set 8

Al atom: 13 15
 0 0 6 2. 1.
 54866.4890 0.839000000E-03
 8211.76650 0.652700000E-02
 1866.17610 0.336660000E-01
 531.129340 0.132902000
 175.117970 0.401266000
 64.0055000 0.531338000
 0 0 3 2. 1.
 64.0055000 0.202305000
 25.2925070 0.624790000
 10.5349100 0.227439000
 0 0 1 2. 1.
 3.20671100 1.00000000
 0 0 1 0. 1.
 1.15255500 1.00000000
 0 0 1 0. 1.
 0.70000000 1.00000000
 0 0 1 0. 1.
 0.35000000 1.00000000
 0 0 1 0. 1.

A Special Basis Sets for AO Calculations with CRYSTAL

```
0 0.176678000 1.00000000
0 2 4 6. 1.
  259.283620 0.944800000E-02
  61.0768700 0.709740000E-01
  19.3032370 0.295636000
0 7.01088200 0.728219000
0 2 2 1. 1.
  2.67386500 0.644467000
0 1.03659600 0.417413000
0 2 1 0. 1.
0 0.700000000 1.00000000
0 2 1 0. 1.
0 0.316819000 1.00000000
0 2 1 0. 1.
0 0.150 1.00000000
0 3 1 0. 1.
0 2.329027007 1.
0 3 1 0. 1.
0 0.480048498 1.
0 4 1 0. 1.
  0.6 1.
  O atom:
8 7
0 0 8 2.0 1.0
  26591.015149286 0.000338543
  4069.713048219 0.002548773
  943.177385588 0.012944513
  270.377217602 0.051837807
  88.721659363 0.164372032
  32.042734201 0.3855
  12.430169888 0.562307539
  4.976247393 0.350155411
0 1 4 6.0 1.0
  62.977656261 -0.006945266 0.006338931
  14.905934605 -0.076543237 0.043166905
  4.611711867 -0.132826481 0.157278934
0 1.603131709 0.379 0.347
0 1 1 0.0 1.0
0 0.568730447 1.0 1.0
0 1 1 0.0 1.0
0 0.184511607 1.0 1.0
0 3 1 0.0 1.0
0 1.387304921 1.0
0 3 1 0.0 1.0
0 0.450916551 1.0
0 4 1 0.0 1.0
  1.428 1.0
```

Appendix

H atom:

1 6
0 0 3 1.0 1.0
34.061341000 0.00602519780
5.1235746000 0.04502109400
1.1646626000 0.20189726000
0 0 1 0.0 1.0
0.4157455100 1.00000000000
0 0 1 0.0 1.0
0.1795111000 1.00000000000
0 2 1 0.0 1.0
1.4070000000 1.00000000000
0 2 1 0.0 1.0
0.3880000000 1.00000000000
0 3 1 0.0 1.0
1.0570000000 1.00000000000

Basis set 9

Al atom:

13 17
0 0 6 2. 1.
54866.4890 0.839000000E-03
8211.76650 0.652700000E-02
1866.17610 0.336660000E-01
531.129340 0.132902000
175.117970 0.401266000
64.0055000 0.531338000
0 0 3 2. 1.
64.0055000 0.202305000
25.2925070 0.624790000
10.5349100 0.227439000
0 0 1 2. 1.
3.20671100 1.00000000
0 0 1 0. 1.
1.15255500 1.00000000
0 0 1 0. 1.
0.70000000 1.00000000
0 0 1 0. 1.
0.35000000 1.00000000
0 0 1 0. 1.
0.176678000 1.00000000
0 2 4 6. 1.
259.283620 0.944800000E-02
61.0768700 0.709740000E-01
19.3032370 0.295636000

A Special Basis Sets for AO Calculations with CRYSTAL

```
0 2 2 1. 1. 7.01088200 0.728219000
    2.67386500 0.644467000
0 2 1 0. 1. 1.03659600 0.417413000
    0.700000000 1.000000000
0 2 1 0. 1. 0.316819000 1.000000000
0 3 1 0. 1. 0.150 1.000000000
0 3 1 0. 1. 2.329027007 1.
0 4 1 0. 1. 0.480048498 1.
0 3 1 0. 1. 0.6 1.
0 4 1 0. 1. 0.120000000 1.
    0.20 1.
    O atom:
8 9
0 0 8 2.0 1.0
    26591.015149286 0.000338543
    4069.713048219 0.002548773
    943.177385588 0.012944513
    270.377217602 0.051837807
    88.721659363 0.164372032
    32.042734201 0.3855
    12.430169888 0.562307539
0 1 4 6.0 1.0 4.976247393 0.350155411
    62.977656261 -0.006945266 0.006338931
    14.905934605 -0.076543237 0.043166905
    4.611711867 -0.132826481 0.157278934
0 1 1 0.0 1.0 1.603131709 0.379 0.347
0 1 1 0.0 1.0 0.568730447 1.0 1.0
0 3 1 0.0 1.0 0.184511607 1.0 1.0
0 3 1 0.0 1.0 1.387304921 1.0
0 4 1 0.0 1.0 0.450916551 1.0
0 3 1 0.0 1.0 1.428 1.0
```

Appendix

```
0.214 1.0
0 4 1 0.0 1.0
0.5 1.0
H atom:
1 6
0 0 3 1.0 1.0
34.061341000 0.00602519780
5.1235746000 0.04502109400
1.1646626000 0.20189726000
0 0 1 0.0 1.0
0.4157455100 1.00000000000
0 0 1 0.0 1.0
0.1795111000 1.00000000000
0 2 1 0.0 1.0
1.40700000000 1.00000000000
0 2 1 0.0 1.0
0.38800000000 1.00000000000
0 3 1 0.0 1.0
1.05700000000 1.00000000000
```

B Basis Set Superposition Error: Adsorption of H₂O at α -Al₂O₃(0001)

In contrast to plane wave calculations, for AO basis calculations a possible error source is the basis set superposition error (BSSE). As mentioned in Section 2.2.1, the BSSE for H₂O at α -Al₂O₃(0001) was calculated for basis set 4, and corresponding results can be found here.

The BSSE is due to overlapping basis functions from different atom centers, leading to an over-stabilization of the adsorbate system. To overcome this, one can apply counterpoise corrections (CP) [53]. For CP the parts of the system are treated individually and also with so-called ghost basis and ghost atoms. This requires a calculation for the water with a “ghost surface”, where the water molecule is treated as usual and the “surface” consists of atomic orbitals but with no charge, so that the electrons of water can occupy them. On the other hand, a similar calculation with the surface and a “ghost water molecule” (or OH and H residues, respectively) has to be computed. Since the structure of the dissociated species (especially the 1-4 dissociated water with a larger OH-H distance) is not necessarily stable without the surface or with a ghosted surface, it is unclear whether these calculations will converge.

In summary, to apply the CP, four calculations in addition to those needed for the determination of E_{ads} (without CP) are required:

- a) the water in the adsorbed geometry plus the surface made from ghost atoms
- b) the surface in the adsorbed geometry plus the ghost water molecule
- c) the water in the adsorbed geometry but without surface
- d) the surface in the adsorbed geometry but without the water.

Then the BSSE-corrected adsorption energy is calculated as:

$$E_{\text{ads}}^{\text{BSSE}} = E_{\text{water-surface}} - E_{\text{relaxed water molecule}} - E_{\text{relaxed surface}} - \Delta E_{\text{BSSE}}, \quad (\text{B.1})$$

with the BSSE given by:

$$\Delta E_{\text{BSSE}} = E(a) + E(b) - E(c) - E(d) . \quad (\text{B.2})$$

The adsorbate-surface interaction energy (stabilizing) is:

$$E_{\text{int}} = E_{\text{water-surface}} - E(a) - E(b) , \quad (\text{B.3})$$

and the relaxation energy (which is destabilizing) is:

$$E_{\text{relax}} = E(c) + E(d) - E_{\text{relaxed water molecule}} - E_{\text{relaxed surface}} . \quad (\text{B.4})$$

When one applies this to the adsorbed systems with basis set 4, the results shown in Table B.2 can be obtained.

Table B.2: Uncorrected adsorption energy, BSSE-corrected energy, BSSE, adsorbate-surface interaction energy and relaxation energy according to Equations (B.1)-(B.4) for the molecular adsorbed species (“mol”), obtained with PBE+D3 using AO basis set 4. Values are given in eV.

E_{ads}	-1.48
$E_{\text{ads}}^{\text{BSSE}}$	-1.34
ΔE_{BSSE}	-0.14
E_{int}	-1.58
E_{relax}	0.24

The missing entries for 1-2 and 1-4 diss in Table B.2 indicate, that the calculations for the 1-2 and 1-4 structure did not converge, because of missing stability in the ghosted calculations. The OH and H residues that are far apart in this case are not stabilized by the ghosted surface (*i.e.* without the real surface).

At least for molecular water one can evaluate the BSSE. For this basis set and geometry it is around 10% of the interaction energy, bringing the adsorption energy close to the PBE+D3/AO-8 value (see Table 2.3), for which a much smaller BSSE is expected.

From the results also follows that the relaxation energy is rather small, at least for the case of molecular adsorption.

C Reaction Probabilities for AIMD Molecular Beam Scattering Simulations of H₂O at α -Al₂O₃(0001)

In this section, the probabilities P for different findings of the AIMD molecular beam scattering simulations from Section 2.3 shall be given in detail. To this end the following abbreviations are used: P_{mol} = molecular adsorption, $P_{\text{diss}}(1-2)$ = 1-2 dissociation, $P_{\text{diss}}(1-4)$ = 1-4 dissociation, $P_{\text{diss}}(1-4')$ = 1-4' dissociation, P_{phys} = physisorption (of molecular D₂O), and P_{refl} = reflection. In case of two numbers in one cell, the first one refers to direct dissociation, and the second gives the probability for indirect dissociation, for example after initial molecular adsorption.

Due to the rounding procedure, the sum of the probabilities can be slightly different from 1. If no probabilities for an outcome are listed, the process did not occur. One has to have in mind that all results are obtained for only a limited number of trajectories whose number is given, respectively.

C.1 Microcanonical AIMD at a Clean Surface at $T = 0$

The probabilities for the microcanonical (NVE) results for a clean surface with a single, cold D₂O molecule and a $T = 0$ K surface for different initial kinetic energies E_{kin} from 0.5 to 0.9 eV are shown in Table C.3

Table C.3: Results for the NVE, $T = 0$ K trajectories of a single D₂O molecule approaching the clean surface. Averages are calculated over all 48 combinations of eight rotational orientations and six lateral impact points for each initial kinetic energy. The two numbers in the $P_{\text{diss}}(1-2)$ column refer to direct and indirect dissociation.

E_{kin} [eV]	P_{mol}	$P_{\text{diss}}(1-2)$	P_{refl}
0.5	0.56	0.17 + 0.08	0.19
0.6	0.58	0.17 + 0.06	0.19
0.7	0.58	0.17 + 0.06	0.19
0.8	0.54	0.15 + 0.12	0.19
0.9	0.50	0.19 + 0.04	0.27

C.2 Refined Surface Models: Effects of Precoverage

An improvement to the clean surface model is a precovered surface, with one D₂O per (2 × 2) supercell. This preadsorbed water was either adsorbed molecularly or dissociatively (1-2 or 1-4). To this prepared surface, a single D₂O molecule was brought with an initial kinetic energy of 0.7 eV with $T = 0$ K (NVE ensemble). The impact site was either in the same (1 × 1) subcell or in a neighboring subcell, see also Figure C.1. The probabilities in Table C.4 were obtained from 89 trajectories. More details can be found in the table caption and footnotes.

Table C.4: NVE reaction probabilities for D₂O approaching the precovered surface with an initial kinetic energy of 0.7 eV. The term “same CUS” refers to a D₂O hitting the (1 × 1) subcell where the water is preadsorbed and “neighbor CUS” refers to a situation, where the incoming molecule hits another subcell. Detail of the impact points can be found in Figure C.1. The preadsorbed water was considered to be either adsorbed molecularly (“preads. mol”), 1-2 dissociated (“preads. 1-2”) or 1-4 dissociated (“preads. 1-4”). If two entries are given, the first refers to the direct dissociation and the second to indirect dissociation.

	preads.	P_{mol}	$P_{\text{diss}}(1-2)$	$P_{\text{diss}}(1-4)$	P_{phys}	P_{refl}
same CUS	mol ¹	0.57	0.00+0.04	0.04+0.00	0.32	0.04
	1-2 ²	0.77	0.08+0.00	0.00	0.00	0.15
	1-4 ³	0.42	0.00	0.00	0.33	0.25
neighbor CUS	mol ⁴	0.36	0.18+0.05	0.23	0.18	0.00
	1-2 ⁵	0.57	0.29	0.00	0.00	0.14
	1-4 ⁶	0.71	0.14	0.00	0.00	0.14

¹ 28 trajectories, for [0.35,0.5], [0.5,0.35] and [0.35,0.45] all eight orientations and for the remaining three impact points only selected ones: [0.33,0.33]: [0,90,0] and [90,90,90]; [0.5,0.5]: [90,90,0] and [0.4,0.5]: [0,90,0].

² 13 trajectories, for [0.35,0.45] all eight orientations, [0.33,0.33]: [0,90,0] and [90,90,90]; [0.5,0.5]: [90,90,0]; [0.35,0.5]: [0,0,0]; [0.4,0.5]: [0,90,0].

³ 12 trajectories, for [0.35,0.45] all orientations were calculated, but [0,90,90] failed, for [0.33,0.33]: [0,90,0] and [90,90,90]; [0.5,0.5]: [90,90,0]; [0.35,0.5]: [0,0,0]; [0.4,0.5]: [0,90,0].

⁴ 22 trajectories, for [0.35,1.0] and [0.5,0.85] all orientations, [0.33,0.83]: [0,90,0] and [90,90,90]; [0.5,1.0]: [90,90,0]; [0.35,0.95]: [0,0,0] and [90,90,0]; [0.4,1.0]: [0,90,0].

⁵ seven trajectories, for [0.33,0.83]: [0,90,0] and [90,90,90]; [0.5,1.0]: [90,90,0]; [0.35,1.0]: [0,0,0]; [0.35,0.95]: [0,0,0] and [90,90,0]; [0.4,1.0]: [0,90,0].

⁶ seven trajectories, for [0.33,0.83]: [0,90,0] and [90,90,90]; [0.5,1.0]: [90,90,0]; [0.35,1.0]: [0,0,0]; [0.35,0.95]: [0,0,0] and [90,90,0]; [0.4,1.0]: [0,90,0].

In addition to the NVE trajectories at $T = 0$ K, analogous NVT calculations were employed for a thermalized and precovered surface. The surface including the preadsorbed species was equilibrated for 1 ps at $T = 300$ K starting from the minimum structure of the adsorbed species. To this surface, water with a kinetic energy of 0.7 eV was shot in 140 trajectories. Probabilities are given in Table C.5 and more details in the footnotes therein.

Table C.5: Probabilities for the NVT (canonical) case at 300 K. Three impact points were considered for the “same CUS”: [0.33,0.33], [0.35,0.45] and [0.5,0.35] and three for the “neighboring CUS”: [0.33,0.83], [0.35,0.95] and [0.5,0.85]. For clarification, these are shown in Figure C.1. If not mentioned otherwise, all eight rotational orientations were considered.

	preads.	P_{mol}	$P_{\text{diss}(1-2)}$	$P_{\text{diss}(1-4)}$	P_{phys}	P_{refl}
same CUS	mol	0.08+0.17	0.00+0.04	0.00	0.63	0.08
	1-2	0.00+0.83	0.00	0.00	0.13	0.04
	1-4 ¹	0.05+0.40	0.00+0.05	0.00	0.40	0.10
neighbor CUS	mol	0.63	0.17+0.17	0.04	0.00	0.00
	1-2	0.71	0.21	0.08	0.00	0.00
	1-4	0.92	0.08	0.00	0.00	0.00

¹ The trajectories for [0.33,0.33] with the orientations [0,0,0], [90,90,0] and [90,90,90] and for impact point [0.5,0.35] with the orientation [90,0,90] failed and were not analyzed.

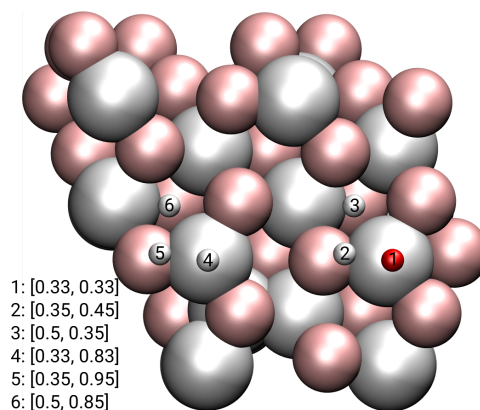


Figure C.1: Distinct lateral impact points for the trajectories from Table C.5 at the “same” (1, 2, 3) and the “neighboring” CUS (4, 5, 6). Position 1 is shown in red because there the preadsorbed OD fragment/water molecule is adsorbed.

C.3 Refined Beam Models: Clustering and Preexcitation

Apart from a refined surface model, the beam model was extended, too. This was performed by either clustering ((D₂O)₂, (D₂O)₄) or by exciting the water molecule vibrationally and/or rotationally.

One type of (D₂O)₂ cluster was tested (see Figure C.2). The structure is not the global minimum structure but a local minimum dimolecular water cluster. Even in the case of the (D₂O)₂ cluster, strong interaction between the molecules can be observed, although not as much as for the tetramer (see below). Also “only” molecular adsorption, 1-2 and 1-4 dissociation occur within the sampling. Interestingly, there is no case, where both molecules react in the

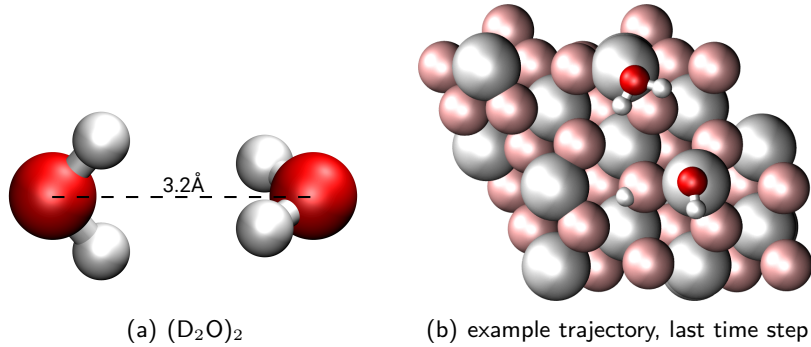


Figure C.2: (a) Structure of the optimized $(D_2O)_2$ cluster. (b) shows an example situation at the last step (after 1.2 ps) for 2 water molecules for the initial parameters $[a_0, b_0]=[0.35,0.45]$, $[\alpha, \beta, \gamma][90,0,90]$.

same way. For most dissociated trajectories there is only direct dissociation at the moment of the impact, with the only indirect one dissociating 0.3 ps later. Apart from that, no further dissociation and diffusion reactions were observed.

Table C.6: Reaction probabilities for microcanonical (NVE, $T = 0$) trajectories of the $(D_2O)_2$ cluster with a clean surface hitting with an initial kinetic energy $E_{kin} = 0.7$ eV.

P_{mol}	$P_{diss(1-2)}$	$P_{diss(1-4)}$	P_{refl}
0.40	0.15+0.05	0.05	0.35

In Table C.7, probabilities for a $(D_2O)_4$ cluster (see Figure 2.8(a)) are shown. This cluster was shot at the surface with an initial kinetic energy of 0.9 eV towards a cold ($T = 0$ K), clean surface in an NVE (microcanonical) MD ansatz. In total, ten trajectories for four different impact points and three different orientations were computed (for one impact point, only one orientation was considered).

Table C.7: Reaction probabilities for a $(D_2O)_4$ cluster approaching a clean surface with $E_{kin} = 0.9$ eV of microcanonical (NVE, $T = 0$) trajectories.

P_{mol}	$P_{diss(1-2)}$	$P_{diss(1-4)}$	$P_{diss(1-4')}$	P_{phys}	P_{refl}
0.25	0.05+0.10	0.03+0.18	0.00+0.05	0.18	0.18

In addition to considering a water cluster, microcanonical MD of a single D_2O molecule that was vibrationally and/or rotationally excited were performed. In addition to the linear momentum towards the surface, the molecule was excited vibrationally (symmetric, asymmetric stretch and bending) or rotationally (around the three axes) and four rotations coupled

with vibrational modes. This was evaluated in ten trajectories for only one set of parameters $([0.35,0.5],[0,0,0])$ for a kinetic energy of 0.7 eV. Probabilities are given in Table C.8

Table C.8: Reaction probabilities of an excited D_2O . Microcanonical (NVE, cold surface) trajectories of vibrationally and/or rotationally excited D_2O approaching a clean surface were simulated with $E_{kin} = 0.7$ eV. If two entries exist, the first refers to direct dissociation and the second to indirect dissociation.

P_{mol}	$P_{diss}(1-2)$	$P_{diss}(1-4)$	$P_{diss}(1-4')$	P_{phys}	P_{refl}
0.20	0.30+0.20	0.00	0.00+0.10	0.00	0.20

D Test of a Symmetric Slab: Normal Modes of H_2O at $\alpha-Al_2O_3(11\bar{2}0)$

To prove that for the $(11\bar{2}0)$ surface it is sufficient to calculate frequencies for the asymmetric slab (Section 3.4), we did test calculations with a slab containing an inversion center. A symmetric model of the surface with 15 layers was built. On both the top and the bottom, D_2O adsorbed dissociatively in the most stable species $inter-CUSa||O-\mu_2$. An optimized structure can be found in Figure D.3. In this model all atoms were allowed to relax. Henceforth, the

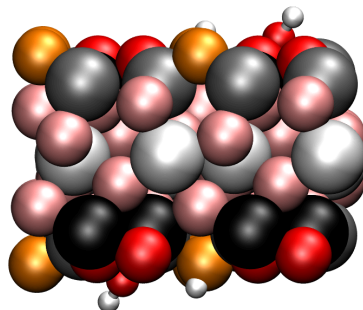


Figure D.3: Side view of the PBE+D2 optimized geometry of the 15 layer symmetric slab. Top view is very similar to Figure 3.4(b), and is not shown here. The adsorbed species is the most stable $inter-CUSa||O-\mu_2$. Color code as explained above.

normal mode analysis gives three imaginary frequencies (with very small energy, yet negative) that represent frustrated translation in a, b and c direction. The spectrum was calculated with normal modes and intensities from the dipole model and can be seen in Figure D.4. The high energy part (see Figure D.4(b)) shows that each of the two peaks comes as a doublet due to coupling of the four OD groups. These doublets lie at 2690 and 2725 cm^{-1} , which is only slightly lower than for the asymmetric model (only one adsorbate on the top) for all applied

E Harmonic Vibrational Spectra for Higher Coverages and the O-II Terminated α -Al₂O₃(11 $\bar{2}$ 0) Surface

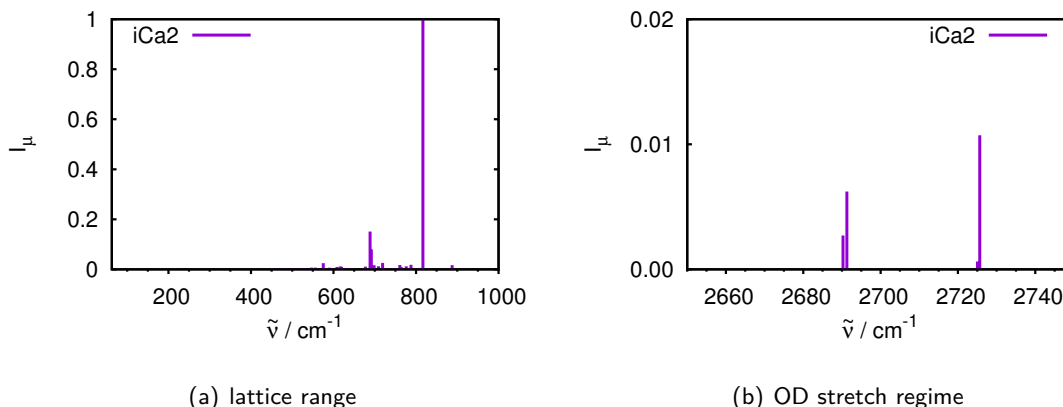


Figure D.4: Stick spectrum of the 15 layer symmetric adsorption model normalized to the most intense peak. (a) shows the lattice range of the spectrum with intensities from the dipole model and (b) gives a closer look at the OD range, featuring two doublets.

slab sizes. For example, for the 15 layer asymmetric system, the peaks come up at 2695 and 2728 cm^{-1} . In the lattice region, these shifts are somewhat larger, but nevertheless small. For example, the most intense peak is shifted from 801 to 816 (15 layer symmetric slab). It can be concluded that while the computational costs are increased, the symmetric system does not give substantially different vibrational frequencies.

E Harmonic Vibrational Spectra for Higher Coverages and the O-II Terminated α -Al₂O₃(11 $\bar{2}$ 0) Surface

In addition to low-coverage regime and the fully covered surface (1ML), spectra were calculated for coverages of 1/3 and 1/6 as well as for the O-II terminated surface, as mentioned in Section 3.4.1.3. First, the higher coverage systems with two water molecules (for the three structures considered see Figure 3.5) were examined. Those three are inter-CUSa||O- μ_2 +CUSb||O- μ_2 and inter-CUSa||O- μ_2 +inter-CUSa||O- μ_2 where both molecules are dissociated, and CUSb+CUSb||O- μ_2 , where one water is dissociated and the other is adsorbed molecularly. The total spectrum and the OD range of the 2D₂O systems in the dipole model are shown in Figure E.5, including a comparison between the systems with two D₂O molecules and the corresponding systems with only one adsorbate. If the water molecules interact strongly with each other, the OD peaks are shifted heavily. The system inter-CUSa||O- μ_2 +CUSb||O- μ_2 where both D₂O molecules are dissociatively adsorbed ((a) and (b) of Figure E.5) seems to

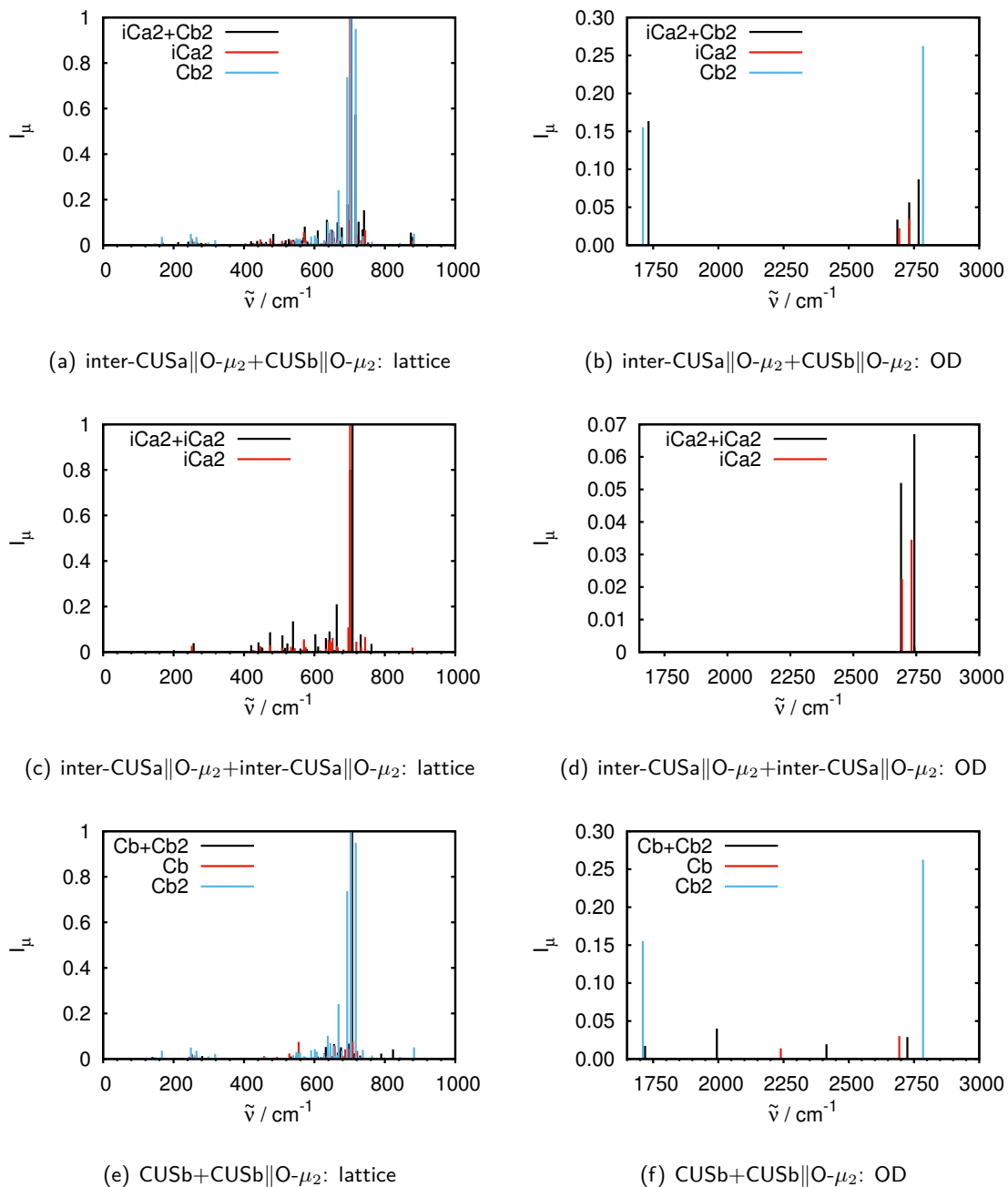


Figure E.5: Stick spectra from normal mode analyses and the dipole model, for two water molecules per (2×2) supercell (10 layer slab, black line) in comparison with the corresponding systems with one water molecule (red, blue). The left column shows the lattice range and the right column the OD range of the respective species. The abbreviations given are iCa2 for inter-CUSa||O- μ_2 , Cb2 for CUSb||O- μ_2 and iCb2 for inter-CUSb||O- μ_2 (see also Section 3.4.1.3).

be affected only weakly, inter-CUSa||O- μ_2 +inter-CUSa||O- μ_2 ((c) and (d)) is shifted slightly more. In this case, also both molecules are dissociated. However, the system CUSb+CUSb||O- μ_2 where one molecule is intact and the other one is dissociated ((e) and (f)) is shifted significantly, displaying a strong interaction between the molecularly adsorbed and the dissociated groups, stabilizing each other.

This is interesting since with respect to the adsorption energy the three systems behave differently, and if the adsorption energies are affected strongly, also the wavenumbers are shifted and vice versa. However, there should not be a correlation between the vibrational frequency and the adsorption energy. The inter-CUSa||O- μ_2 +inter-CUSa||O- μ_2 adsorption energy decreased its stability, whereas E_{ads} for the system inter-CUSa||O- μ_2 +CUSb||O- μ_2 did not change and for CUSb+CUSb||O- μ_2 E_{ads} even was more stabilized. With this in mind, it makes sense that those systems, in which the adsorption energy is slightly affected also shows hardly any difference to the single adsorption in the spectrum. On the other hand, the system where the molecular water is stabilized by its dissociated neighbor, the spectrum is shifted strongly. The inter-CUSa||O- μ_2 +inter-CUSa||O- μ_2 is more balanced, because the geometry does not change largely and only the adsorption energy is affected (in a destabilizing way).

Looking at the spectrum of the system with four adsorbed water molecules (1/3 coverage) we obtain Figure E.6 for vibrational spectra within the dipole model. All of these water molecules

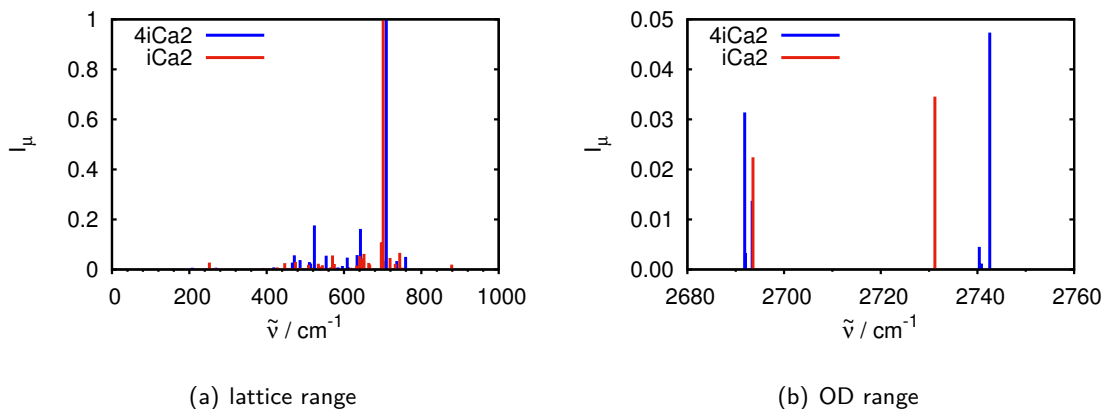


Figure E.6: Stick spectra from normal mode analyses and the dipole model for four water molecules per (2×2) supercell (10 layers) in blue, in comparison to a single water molecule dissociated to inter-CUSa||O- μ_2 (red). (a) shows the lattice range and (b) the OD range. The short notation stands for iCa2=inter-CUSa||O- μ_2 .

are adsorbed in inter-CUSa||O- μ_2 , see Figure 3.6(a) and E.6, which is the most stable and hence the most probable adsorbed species. As expected, we see the stretch vibrations of the adsorbed residue at higher wavenumbers. There are three modes for asymmetric (OD oscillators in con-

trary phases) and one for symmetric stretch vibrations (all OD oscillators in phase) around 2740 cm^{-1} . At lower wavenumbers (between 2691 and 2693 cm^{-1}), there are localized OD_{surf} vibrations (Figure E.6(b)). Below that there are delocalized combined vibrations of lattice and OD (panel (a)). In comparison to the singly adsorbed system (red line) there is an astonishing agreement, both in the OD range and the lattice region. When looking at the intensities in Figure E.6(b) one can see that the intensities of the singly adsorbed inter-CUSa||O- μ_2 are almost as high as for the system with four dissociatively adsorbed water molecules (and not approximately 1/4 of it). In contrast to that for the system with two inter-CUSa||O- μ_2 species the intensities of the respective mono adsorbed species is halved (see Figure E.5(d)). This is probably an artifact of the normalization to the highest peak in the lattice region.

Apart from the most stable surface termination (O-I), calculations of the second most stable surface termination (O-II), where the uppermost O layer is “missing”, were performed to account for the “unknown” sublattice visible in LEED spectra. Frequencies were analyzed for the clean surface and the fully covered system as shown in Figure 3.7, for both the 10 and 25 layer systems. In Figure E.7 the spectra from normal mode analysis within the dipole model

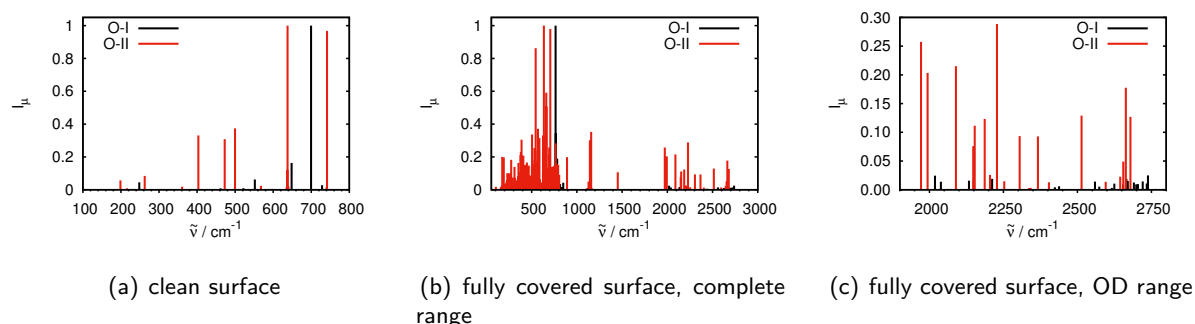
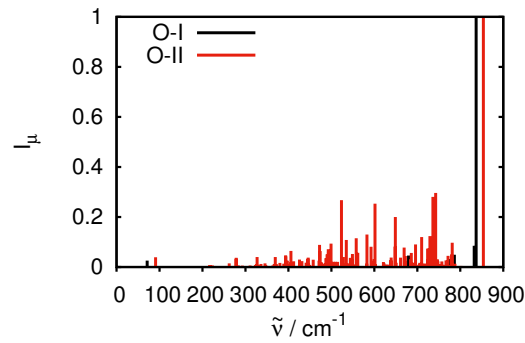


Figure E.7: Comparison of the 10 layer slab spectra calculated with normal mode analysis and intensities from the dipole corrections. The clean surface (a), O-I termination (most stable under the whole range of chemical potential) and O-II termination (see Kurita [21], also relatively stable over a wide range of chemical potential). The comparison of the fully covered O-I and O-II terminations is shown in (b) with a detailed view of the OD range in (c).

for the clean (a) and the fully covered surface termination O-II ((b), (c)) in comparison to the more stable O-I termination are given for the 10 layer slab. For the clean surfaces, the spectra of O-I and O-II deviate strongly: peaks are shifted by around 50 cm^{-1} and intensity distributions are different. The differences for the fully covered surfaces are more pronounced due to the different structures including especially more molecularly adsorbed water for the O-II termination (*cf.* Figure 3.7).

E Harmonic Vibrational Spectra for Higher Coverages and the O-II Terminated α -Al₂O₃(11 $\bar{2}$ 0) Surface

This comparison was also made for the clean surface with a larger slab (25 layers), see Figure E.8. The spectra are very similar and the most intense peak is only shifted by 20 cm⁻¹. After



(a) clean surface

Figure E.8: Comparing the O-I and O-II terminated clean surface of the 25 layer system shows that for both systems very similar results are obtained. The most intense peak is shifted by around 20 cm⁻¹.

normalization to the most intense peak, for the O-I termination the intensities of further peaks are weaker than for the O-II terminated surface for most vibrations. In the larger slab model there are many more bulk atoms than surface atoms which can contribute to vibrations. Due to this the differences between O-I and O-II termination get less significant for the larger system.

Appendix

Publications

- (1) Heiden, S.; Yue, Y.; Kirsch, H.; Wirth, J.; Saalfrank, P.; Campen, R. K.: »Water Dissociative Adsorption on α -Al₂O₃(11 $\bar{2}$ 0) Is Controlled by Surface Site Undercoordination, Density, and Topology«, *The Journal of Physical Chemistry C* **2018**, *122* (12), 6573-6584.
- (2) Heiden, S.; Wirth, J.; Campen, R. K.; Saalfrank, P.: »Water Molecular Beam Scattering at α -Al₂O₃(0001): An *Ab Initio* Molecular Dynamics Study«, *The Journal of Physical Chemistry C* **2018**, *122* (27), 15494-15504.

List of Abbreviations

AIMD	<i>ab initio</i> molecular dynamics
BEC	Born effective charges
BSSE	basis set superposition error
B3LYP	Becke 3 parameters Lee Yang Parr, hybrid functional
CP	counterpoise corrections
CUS	coordinatively unsaturated site
DFT	density functional theory
D2/D3	dispersion corrections (van der Waals interactions)
GGA	generalized gradient approximation
LDA	local density approximation
LEED	low energy electron diffraction
LMP2	local Møller Plesset perturbation theory of second order
MBS	molecular beam source
MD	molecular dynamics
ML	monolayer
MP2	Møller Plesset perturbation theory of second order
NEB	nudged elastic band
NEB-CI	nudged elastic band with climbing image
NMA	normal mode analysis
NVE	number of particles/volume/energy kept constant
NVT	number of particles/volume/temperature held constant
PAW	projector augmented wave
PBE	Perdew Burke Ernzerhof density functional
PES	potential energy surface
PW	plane waves
SFG	sum frequency generation
TDS	thermal desorption spectroscopy
TS(T)	transition state (theory)
VASP	Vienna ab-initio simulation package
VSF	vibrational sum frequency (=SFG)
WFT	wave function theory

References

- [1] Ago, H.; Nakamura, K.; Ikeda, K.; Uehara, N.; Ishigami, N.; Tsuji, M. Aligned Growth of Isolated Single-Walled Carbon Nanotubes Programmed by Atomic Arrangement of Substrate Surface, *Chem. Phys. Lett.* **2005**, *408*, 433–438.
- [2] Cargnello, M.; Delgado, J.; Hernández, J.; Bakhmutsky, K. .; Montini, T.; Gámez, J. C.; Gorte, R.; Fornasiero, P. Exceptional Activity for Methane Combustion over Modular Pd@CeO₂ Subunits on Functionalized Al₂O₃, *Science* **2012**, *337*, 713–717.
- [3] Knözinger, H.; Ratnasamy, P. Catalytic Aluminas: Surface Models and Characterization of Surface Sites, *Catal. Rev.* **1978**, *17*, 31–70.
- [4] Pearson, M. J. Alumina Catalysts in Low-Temperature Claus Process, *Product R&D* **1977**, *16*, 154–158.
- [5] Özbek, M. O.; van Santen, R. A. The Mechanism of Ethylene Epoxidation Catalysis, *Catal. Lett.* **2013**, *143*, 131–141.
- [6] Van Parijs, I. A.; Froment, G. F. Kinetics of Hydrodesulfurization on a Cobalt-Molybdenum/ γ -Alumina Catalyst. 1. Kinetics of the Hydrogenolysis of Thiophene, *Ind. Eng. Chem. Prod. Res. Dev.* **1986**, *25*, 431–436.
- [7] Breuer, H. *dtv-Atlas Chemie, Band 1, Allgemeine und anorganische Chemie*; dtv: München, 9 ed.; 2000.
- [8] Riedel, E.; Janiak, C. *Anorganische Chemie*; Walter de Gruyter: Berlin, 7 ed.; 2007.
- [9] Trail, D.; Watson, E. B.; Tailby, N. D. The Oxidation State of Hadean Magmas and Implications for Early Earth's Atmosphere, *Nature* **2011**, *480*, 79–82.
- [10] Frei, R.; Gaucher, C.; Poulton, S. W.; Canfield, D. E. Fluctuations in Precambrian Atmospheric Oxygenation Recorded by Chromium Isotopes, *Nature* **2009**, *461*, 250–253.
- [11] Buick, R. When did Oxygenic Photosynthesis Evolve?, *Philos. Trans. R. Soc. Lond. B: Biol. Sci.* **2008**, *363*, 2731–2743.
- [12] Olson, J. M. Photosynthesis in the Archean Era, *Photosynth. Res.* **2006**, *88*, 109–117.
- [13] Kirschvink, J. L.; Kopp, R. E. Palaeoproterozoic Ice Houses and the Evolution of Oxygen-mediating Enzymes: The Case for a Late Origin of Photosystem II, *Philos. Trans. R. Soc. Lond. B: Biol. Sci.* **2008**, *363*, 2755–2765.

- [14] Elam, J. W.; Nelson, C. E.; Cameron, M. A.; Tolbert, M. A.; George, S. M. Adsorption of H₂O on a Single-Crystal α -Al₂O₃(0001) Surface, *J. Phys. Chem. B* **1998**, *102*, 7008–7015.
- [15] Potter, A. E. J. Environmental Effects of the Space Shuttle, *Environ. Sci.* **1978**, *21*, 15–21.
- [16] Cofer, W. R.; Lala, G. G.; Wightman, J. P. Analysis of Mid-Tropospheric Space Shuttle Exhausted Aluminum Oxide Particles, *Atmos. Environ.* **1987**, *21*, 1187–1196.
- [17] Jones, A. E.; Bekki, S.; Pyle, J. A. On the Atmospheric Impact of Launching the Ariane 5 Rocket, *J. Geophys. Res.: Atm.* **1995**, *100*, 16651–16660.
- [18] Jackman, C. H.; Fleming, E. L.; Chandra, S.; Considine, D. B.; Rosenfield, J. E. Past, Present, and Future Modeled Ozone Trends with Comparisons to Observed Trends, *J. Geophys. Res.: Atm.* **1996**, *101*, 28,753–28,767.
- [19] Passerini, L. Solid Solutions, Isomorphism and Symmorphisms of the Oxide of Trivalent Metals: The Systems Al₂O₃-Cr₂O₃, Al₂O₃-Fe₂O₃, Cr₂O₃-Fe₂O₃, *Gazz. Chim. Ital.* **1930**, *60*, 544–548.
- [20] Wyckoff, R. W. G. *The Structure of Crystals*; American Chemical Society: 1931.
- [21] Kurita, T.; Uchida, K.; Oshiyama, A. Atomic and Electronic Structures of α -Al₂O₃ Surfaces, *Phys. Rev. B* **2010**, *82*, 1553191-1–14.
- [22] Kirsch, H.; Wirth, J.; Tong, Y.; Wolf, M.; Saalfrank, P.; Campen, R. K. Experimental Characterization of Unimolecular Water Dissociative Adsorption on α -Alumina, *J. Phys. Chem. C* **2014**, *118*, 13623–13630.
- [23] Jensen, F. *Introduction to Computational Chemistry*; Wiley: 2 ed.; 2007.
- [24] Groß, A. *Theoretical Surface Science: A Microscopic Perspective*; Springer: 2003.
- [25] Szabo, A.; Ostlund, N. S. *Modern Quantum Chemistry: Introduction to Advanced Electronic Structure Theory*; Dover Publications, Inc.: Mineola, First ed.; 1996.
- [26] Born, M.; Oppenheimer, R. Zur Quantentheorie der Molekeln, *Annalen der Physik* **1927**, *389*, 457–484.
- [27] Møller, C.; Plesset, M. S. Note on an Approximation Treatment for Many-Electron Systems, *Phys. Rev.* **1934**, *46*, 618–622.
- [28] Suhai, S.; Ladik, J. Perturbation Theoretical Calculation of the Correlation Energy in an Infinite Metallic Hydrogen Chain, *J. Phys. C: Solid State Phys.* **1984**, *15*, 4327–4337.
- [29] Hohenberg, P.; Kohn, W. Inhomogeneous Electron Gas, *Phys. Rev.* **1964**, *136*, B864–B871.
- [30] Kohn, W.; Sham, L. J. Self-Consistent Equations Including Exchange and Correlation Effects, *Phys. Rev.* **1965**, *140*, A1133–A1138.
- [31] Perdew, J. P.; Burke, K.; Ernzerhof, M. Generalized Gradient Approximation Made Simple, *Phys. Rev. Lett.* **1996**, *77*, 3865–3868.

- [32] Perdew, J. P.; Burke, K.; Ernzerhof, M. Erratum: Generalized Gradient Approximation Made Simple, *Phys. Rev. Lett.* **1997**, *78*, 1396.
- [33] Becke, A. D. A New Mixing of Hartree-Fock and Local Density-Functional Theories, *J. Chem. Phys.* **1993**, *98*, 1372–1377.
- [34] Stephens, P. J.; Devlin, F. J.; Chabalowski, C. F.; Frisch, M. J. *Ab Initio* Calculation of Vibrational Absorption and Circular Dichroism Spectra Using Density Functional Theory, *J. Phys. Chem.* **1994**, *98*, 11623–11627.
- [35] Krukau, A. V.; Vydrov, O. A.; Izmaylov, A. F.; Scuseria, G. E. Influence of the Exchange Screening Parameter on the Performance of Screened Hybrid Functionals, *J. Chem. Phys.* **2006**, *125*, 224106-1–5.
- [36] Becke, A. D. Density-Functional Thermochemistry. III. The Role of Exact Exchange, *J. Chem. Phys.* **1993**, *98*, 5648–5652.
- [37] Grimme, S. Semiempirical GGA-Type Density Functional Constructed with a Long-Range Dispersion Correction, *J. Comput. Chem.* **2006**, *27*, 1787–1799.
- [38] Kresse, G.; Hafner, J. *Ab Initio* Molecular Dynamics for Liquid Metals, *Phys. Rev. B: Condens. Matter Mater. Phys.* **1993**, *47*, 558–561.
- [39] Kresse, G.; Hafner, J. *Ab Initio* Molecular-Dynamics Simulation of the Liquid-Metal - Amorphous-Semiconductor Transition in Germanium, *Phys. Rev. B: Condens. Matter Mater. Phys.* **1994**, *49*, 14251–14269.
- [40] Kresse, G.; Furthmüller, J. Efficiency of *Ab Initio* Total Energy Calculations for Metals and Semiconductors using a Plane-Wave Basis Set, *Comput. Mat. Sci.* **1996**, *6*, 15–50.
- [41] Kresse, G.; Furthmüller, J. Efficient Iterative Schemes for *Ab Initio* Total-Energy Calculations using a Plane-Wave Basis Set, *Phys. Rev. B: Condens. Matter Mater. Phys.* **1996**, *54*, 11169–11186.
- [42] Kresse, G.; Joubert, D. From Ultrasoft Pseudopotentials to the Projector Augmented-Wave Method, *Phys. Rev. B: Condens. Matter Mater. Phys.* **1999**, *59*, 1758–1775.
- [43] Dovesi, R.; Orlando, R.; Erba, A.; Zicovich-Wilson, C. M.; Civalleri, B.; Casassa, S.; et. al., CRYSTAL14: A Program for the *Ab Initio* Investigation of Crystalline Solids, *Int. J. Quant. Chem.* **2014**, *114*, 1287–1317.
- [44] Bloch, F. Über die Quantenmechanik der Elektronen in Kristallgittern, *Z. Phys.* **1928**, *52*, 555-600.
- [45] Usvyat, D.; Maschio, L.; Schütz, M. Periodic Local MP2 Method Employing Orbital Specific Virtuals, *J. Chem. Phys.* **2015**, *143*, 102805-1–12.
- [46] Usvyat, D.; Maschio, L.; Schütz, M. Periodic Local Møller-Plesset Perturbation Theory of Second Order for Solids, *Handbook of Solid State Chemistry* **2017**, *5*, 59–86.

- [47] Maschio, L.; Usvyat, D.; Manby, F. R.; Casassa, S.; Pisani, C.; Schütz, M. Fast Local-MP2 Method With Density-Fitting For Crystals. I. Theory and Algorithms, *Phys. Rev. B* **2007**, *76*, 075101-1–9.
- [48] Pisani, C.; Schütz, M.; Casassa, S.; Usvyat, D.; Maschio, L.; Lorenz, M.; Erba, A. Cryscor: A Program for the Post-Hartree-Fock Treatment of Periodic Systems, *Phys. Chem. Chem. Phys.* **2012**, *14*, 7615–7628.
- [49] Usvyat, D.; Maschio, L.; Pisani, C.; Schütz, M. Second Order Local Møller Plesset Perturbation Theory for Periodic Systems: the CRYSCOR Code, *Z. Phys. Chem.* **2010**, *224*, 441–454.
- [50] Tosoni, S.; Tuma, C.; Sauer, J.; Civalleri, B.; Ugliengo, P. A Comparison between Plane Wave and Gaussian-Type Orbital Basis Sets for Hydrogen Bonded Systems: Formic Acid as a Test Case, *J. Chem. Phys.* **2007**, *127*, 154102-1–11.
- [51] Blöchl, P. E. Projector Augmented-Wave Method, *Phys. Rev. B* **1994**, *50*, 17953–17979.
- [52] Kresse, G.; Joubert, D. From Ultrasoft Pseudopotentials to the Projector Augmented-Wave Method, *Phys. Rev. B: Condens. Matter Mater. Phys.* **1999**, *59*, 1758–1775.
- [53] Boys, S. F.; Bernardi, F. Calculation of Small Molecular Interactions by Differences of Separate Total Energies - Some Procedures with Reduced Errors, *Mol. Phys.* **1970**, *19*, 553–566.
- [54] Marx, D.; Hutter, J. *Ab Initio Molecular Dynamics: Basic Theory and Advanced Methods*; Cambridge University Press: 2012.
- [55] Marx, D.; Parinello, M. *Ab Initio Path Integral Molecular Dynamics: Basic Ideas*, *J. Chem. Phys.* **1996**, *104*, 4077–4082.
- [56] Verlet, L. Computer "Experiments" on Classical Fluids. I. Thermodynamical Properties of Lennard-Jones Molecules, *Phys. Rev.* **1967**, *159*, 98–103.
- [57] Nosé, S. A Unified Formulation of the Constant Temperature Molecular Dynamics Methods, *J. Chem. Phys.* **1984**, 511–519.
- [58] Nosé, S. A Molecular Dynamics Method for Simulations in the Canonical Ensemble, *Mol. Phys.* **1984**, 255–268.
- [59] Hoover, W. G. Canonical Dynamics: Equilibrium Phase-Space Distributions, *Phys. Rev. A: At., Mol., Opt. Phys.* **1985**, 1695–1697.
- [60] Melani, G.; Nagata, Y.; Wirth, J.; Saalfrank, P. Vibrational Spectroscopy of Hydroxylated α -Al₂O₃(0001) Surfaces with and without Water: An *Ab Initio* Molecular Dynamics Study, *J. Chem. Phys.* **2018**, *149*, 014707-1–10.
- [61] Karhánek, D.; Bučko, T.; Hafner, J. A Density-Functional Study of the Adsorption of Methane-Thiol on the (111) Surfaces of the Ni-Group Metals: II. Vibrational Spectroscopy, *J. Phys.: Condens. Matter* **2010**, *22*, 265006-1–9.

- [62] Yang, B.; Kaden, W. E.; Yu, X.; Boscoboinik, J. A.; Martynova, Y.; Lichtenstein, L.; Heyde, M.; Sterrer, M.; Włodarczyk, R.; Sierka, M.; Sauer, J.; Shaikhutdinov, S.; Freund, H.-J. Thin Silica Films on Ru(0001): Monolayer, Bilayer and Three-Dimensional Networks of [SiO₄] Tetrahedra, *Phys. Chem. Chem. Phys.* **2012**, *14*, 11344–11351.
- [63] Baroni, S.; Giannozzi, P.; Testa, A. Green's-Function Approach to Linear Response in Solids, *Phys. Rev. Lett.* **1987**, *58*, 1861–1864.
- [64] Giannozzi, P.; Gironcoli, S.; Pavone, P.; Baroni, S. *Ab Initio* Calculation of Phonon Dispersion in Semiconductors, *Phys. Rev. B* **1991**, *43*, 7231–7242.
- [65] Born, M.; Huang, K. *Dynamical Theory of Crystal Lattices*; Oxford University Press: 1954.
- [66] Brüesch, P. *Phonons: Theory and Experiments II*; Springer: 1986.
- [67] Baroni, S.; de Gironcoli, S.; Corso, A. D.; Giannozzi, P. Phonons and Related Crystal Properties from Density-Functional Perturbation Theory, *Rev. Mod. Phys.* **2001**, *75*, 515–562.
- [68] Grillo, F.; Garrido Torres, J. A.; Treanor, M.-J.; Larrea, C. R.; Götze, J. P.; Lacovig, P.; Fruchtl, H. A.; Schaub, R.; Richardson, N. V. Two-Dimensional Self-Assembly of Benzotriazole on an Inert Substrate, *Nanoscale* **2016**, *8*, 9167–9177.
- [69] Thomas, M.; Brehm, M.; Fligg, R.; Vöhringer, P.; Kirchner, B. Computing Vibrational Spectra from *Ab Initio* Molecular Dynamics, *Phys. Chem. Chem. Phys.* **2013**, *15*, 6608–6622.
- [70] Horníček, J.; Kaprálová, P.; Bouř, P. Simulations of Vibrational Spectra from Classical Trajectories: Calibrations with *Ab Initio* Force Fields, *J. Chem. Phys.* **2007**, *127*, 084502-1–9.
- [71] Hudecová, J.; Hopmann, K.; Bouř, P. Correction of Vibrational Broadening in Molecular Dynamics Clusters with the Normal Mode Optimization Method, *J. Phys. Chem. B* **2012**, *116*, 336–342.
- [72] Eyring, H. The Activated Complex in Chemical Reactions, *J. Chem. Phys.* **1935**, 107–115.
- [73] Eyring, H.; Polanyi, M. On Simple Gas Reactions, *Z. Phys. Chem.* **1931/2013**, *227*, 1221–1245.
- [74] Henkelman, G.; Jónsson, H. Improved Tangent Estimate in the Nudged Elastic Band Method for Finding Minimum Energy Paths and Saddle Points, *J. Chem. Phys.* **2000**, *113*, 9978–9985.
- [75] Henkelman, G.; Uberuaga, B. P.; Jónsson, H. A Climbing Image Nudged Elastic Band Method for Finding Saddle Points and Minimum Energy Paths, *J. Chem. Phys.* **2000**, *113*, 9901–9904.
- [76] Wirth, J.; Saalfrank, P. The Chemistry of Water on α -Alumina: Kinetics and Nuclear Quantum Effects from First Principles, *J. Phys. Chem. C* **2012**, *116*, 26829–26840.
- [77] Tong, Y.; Wirth, J.; Kirsch, H.; Wolf, M.; Saalfrank, P.; Campen, R. K. Optically Probing Al-O and O-H Vibrations to Characterize Water Adsorption and Surface Reconstruction on α -Alumina: An Experimental and Theoretical Study, *J. Chem. Phys.* **2015**, *142*, 054704-1–12.

- [78] Wirth, J.; Kirsch, H.; Wlosczyk, S.; Tong, Y.; Saalfrank, P.; Campen, R. K. Characterization of Water Dissociation on α -Al₂O₃(1 $\bar{1}$ 02): Theory and Experiment, *Phys. Chem. Chem. Phys.* **2016**, *18*, 14822–14832.
- [79] Hass, K. C.; Schneider, W. F.; Curioni, A.; Andreoni, W. The Chemistry of Water on Alumina Surfaces: Reaction Dynamics from First Principles, *Science* **1998**, *282*, 265–268.
- [80] Hass, K. C.; Schneider, W. F.; Curioni, A.; Andreoni, W. First-Principles Molecular Dynamics Simulations of H₂O on α -Al₂O₃(0001), *J. Phys. Chem. B* **2000**, *104*, 5527–5540.
- [81] Brown, G. E.; Henrich, V. E.; Casey, W. H.; Clark, D. L.; Eggleston, C.; Felmy, A.; Goodman, D. W.; Grätzel, M.; Maciel, G.; McCarthy, M. I.; Nealon, K. H.; Sverjensky, D. A.; Toney, M. F.; Zachara, J. M. Metal Oxide Surfaces and Their Interactions with Aqueous Solutions and Microbial Organisms, *Chem. Rev.* **1999**, *99*, 77–174.
- [82] Kelber, J. A. Alumina Surfaces and Interfaces under Non-Ultrahigh Vacuum Conditions, *Surf. Sci. Rep.* **2007**, *62*, 271–303.
- [83] Tsyganenko, A. A.; Mardilovich, P. P. Structure of Alumina Surfaces, *J. Chem. Soc., Faraday Trans.* **1996**, *92*, 4843–4852.
- [84] Chang, C. C. Silicon-on-Sapphire Epitaxy by Vacuum Sublimation: LEED-Auger Studies and Electronic Properties of the Films, *J. Vac. Sci. Technol.* **1971**, *8*, 500–511.
- [85] Lee, W. E.; Lagerlof, K. P. D. Structural and Electron Diffraction Data for Sapphire (α -Al₂O₃), *J. Electron Microsc. Tech.* **1985**, *2*, 247–258.
- [86] Nelson, C. E.; Elam, J. W.; Cameron, M. A.; Tolbert, M. A.; Georges, S. M. Desorption of H₂O from a Hydroxylated Single-Crystal α -Al₂O₃(0001) Surface, *Surf. Sci.* **1998**, *416*, 341–353.
- [87] Ranea, V. A.; Carmichael, I.; Schneider, W. F. DFT Investigation of Intermediate Steps in the Hydrolysis of α -Al₂O₃(0001), *J. Phys. Chem. C* **2009**, *113*, 2149–2158.
- [88] Thissen, P.; Grundmeier, G.; Wippermann, S.; Schmidt, W. G. Water Adsorption on the α -Al₂O₃(0001) Surface, *Phys. Rev. B* **2009**, *80*, 245403-1–6.
- [89] Shapovalov, V.; Truong, T. N. *Ab Initio* Study of Water Adsorption on α -Al₂O₃(0001) Crystal Surface, *J. Phys. Chem. B* **2000**, *104*, 9859–9863.
- [90] Wittbrodt, J. M.; Hase, W. L.; Schlegel, H. B. *Ab Initio* Study of the Interaction of Water with Cluster Models of the Aluminum Terminated (0001) α -Aluminum Oxide Surface, *J. Phys. Chem. B* **1998**, *102*, 6539–6548.
- [91] Wang, B.; Hou, H.; Luo, Y.; Li, Y.; Zhao, Y.; Li, X. Density Functional/All-Electron Basis Set Slab Model Calculations of the Adsorption/Dissociation Mechanisms of Water on α -Al₂O₃(0001) Surface, *J. Phys. Chem. C* **2011**, *115*, 13399–13411.
- [92] Heiden, S.; Wirth, J.; Campen, R. K.; Saalfrank, P. Water Molecular Beam Scattering at α -Al₂O₃(0001): An *Ab Initio* Molecular Dynamics Study, *J. Phys. Chem. C* **2018**, *122*, 15494–15504.

- [93] Wirth, J. *Chemische Reaktionen in Substrat-Adsorbat-Systemen: Eine kinetische Perspektive*, Thesis, Universität Potsdam, 2014.
- [94] Heifets, E.; Kotomin, E. A.; Bagaturyants, A. A.; Maier, J. *Ab Initio* Study of BiFeO₃: Thermodynamic Stability Conditions, *J. Phys. Chem. Lett.* **2015**, *6*, 2847–2851.
- [95] Peintinger, M. F.; Oliveira, D. V.; Bredow, T. Consistent Gaussian Basis Sets of Triple-Zeta Valence with Polarization Quality for Solid-State Calculations, *J. Comput. Chem.* **2012**, *34*, 451–459.
- [96] Heyd, J.; Peralta, J. E.; Scuseria, G. E.; Martin, R. L. Energy Band Gaps and Lattice Parameters Evaluated with the Heyd-Scuseria-Ernzerhof Screened Hybrid Functional, *J. Chem. Phys.* **2005**, *123*, 174101-1–8.
- [97] Pernot, P.; Civalleri, B.; Presti, D.; Savin, A. Prediction Uncertainty of Density Functional Approximations for Properties of Crystals with Cubic Symmetry, *J. Phys. Chem. A* **2015**, *119*, 5288–5304.
- [98] Catti, M.; Valerio, G.; Dovesi, R.; Causà, M. Quantum-Mechanical Calculation of the Solid-State Equilibrium MgO+ α -Al₂O₃ \rightleftharpoons MgAl₂O₄ (Spinel) versus Pressure, *Phys. Rev. B* **1994**, *49*, 14179–14187.
- [99] Montanari, B.; Civalleri, B.; Zicovich-Wilson, C. M.; Dovesi, R. Influence of the Exchange-Correlation Functional in All-Electron Calculations of the Vibrational Frequencies of Corundum (α -Al₂O₃), *Int. J. Quantum Chem.* **2006**, *106*, 1703–1714.
- [100] Demichelis, R.; Noel, Y.; Civalleri, B.; Roetti, C.; Ferrero, M.; Dovesi, R. The Vibrational Spectrum of α -AlOOH Diaspore: An *Ab Initio* Study with the CRYSTAL Code, *J. Phys. Chem. B* **2007**, *111*, 9337–9346.
- [101] Kesharwani, M. K.; Brauer, B.; Martin, J. M. L. Frequency and Zero-Point Vibrational Energy Scale Factors for Double-Hybrid Density Functionals (and Other Selected Methods): Can Anharmonic Force Fields Be Avoided?, *J. Phys. Chem. A* **2015**, *119*, 1701–1714.
- [102] Simons, J.; Nichols, J. Strategies for Walking on Potential Energy Surfaces Using Local Quadratic Approximations, *Int. J. Quantum Chem. Symp.* **1990**, *24*, 263.
- [103] Zicovich-Wilson, C. M.; San-Román, M. L.; Ramírez-Solís, A. Mechanism of F⁻ Elimination from Zeolitic D4R Units: A Periodic B3LYP Study on the Octadecasil Zeolite, *J. Phys. Chem. C* **2010**, *114*, 2989–2995.
- [104] Heiden, S.; Yue, Y.; Kirsch, H.; Wirth, J.; Saalfrank, P.; Campen, R. K. Water Dissociative Adsorption on α -Al₂O₃(11 $\bar{2}$ 0) Is Controlled by Surface Site Undercoordination, Density, and Topology, *J. Phys. Chem. C* **2018**, *122*, 6573–6584.
- [105] Wales, D. J.; Walsh, T. R. Theoretical Study of the Water Tetramer, *J. Chem. Phys.* **1997**, *106*, 7193–7207.

- [106] Catalano, J. G. Relaxations and Interfacial Water Ordering at the Corundum (110) Surface, *J. Phys. Chem. C* **2010**, *114*, 6624–6630.
- [107] Becker, T.; Birkner, A.; Witte, G.; Wöll, C. Microstructure of the α -Al₂O₃(11 $\bar{2}$ 0) Surface, *Phys. Rev. B* **2002**, *65*, 115401-1–8.
- [108] Marmier, A.; Parker, S. C. *Ab Initio* Morphology and Surface Thermodynamics of α -Al₂O₃, *Phys. Rev. B* **2004**, *69*, 115409-1–9.
- [109] Sung, J.; Shen, Y. R.; Waychunas, G. A. The Interfacial Structure of Water/Protonated α -Al₂O₃(11 $\bar{2}$ 0) as a Function of pH, *J. Phys.: Condens. Matter* **2012**, *24*, 124101-1–9.
- [110] Monkhorst, H. J.; Pack, J. D. Special Points for Brillouin-Zone Integrations, *Phys. Rev. B* **1976**, *13*, 5177–5192.
- [111] Stair, P. C. The Concept of Lewis Acids and Bases Applied to Surfaces, *J. Am. Chem. Soc.* **1982**, *104*, 4044–4052.
- [112] Zhao, Y.; González-García, N.; Truhlar, D. G. Benchmark Database of Barrier Heights for Heavy Atom Transfer, Nucleophilic Substitution, Association, and Unimolecular Reactions and its Use to Test Theoretical Methods, *J. Phys. Chem. A* **2005**, *109*, 2012–2018.
- [113] Ohto, T.; Hasegawa, T.; Bonn, M.; Nagata, Y. Toward *Ab Initio* Molecular Dynamics Modeling for Sum-Frequency Generation Spectra; An Efficient Algorithm Based on Surface-Specific Velocity-Velocity Correlation Function, *J. Chem. Phys.* **2015**, *143*, 124702-1–10.
- [114] Dunning Jr., T. H. Gaussian Basis Sets for Use in Correlated Molecular Calculations. I. The Atoms Boron through Neon and Hydrogen, *J. Chem. Phys.* **1989**, *90*, 1007–1023.

Erklärung

Hiermit versichere ich, dass die vorliegende Arbeit an keiner anderen Hochschule eingereicht sowie selbständig und ausschließlich mit den angegebenen Quellen angefertigt worden ist.

Potsdam, Dezember 2018